

MECHANICAL CHARACTERIZATION OF 3D PRINTED CORE AND SANDWICH COMPOSITE

Thesis

Submitted in partial fulfillment of the requirements for the degree of

DOCTOR OF PHILOSOPHY

by

BHARATH H S



DEPARTMENT OF MECHANICAL ENGINEERING
NATIONAL INSTITUTE OF TECHNOLOGY KARNATAKA,
SURATHKAL, MANGALORE – 575025

AUGUST, 2021

DECLARATION

I hereby *declare* that the Research Thesis entitled “**MECHANICAL CHARACTERIZATION OF 3D PRINTED CORE AND SANDWICH COMPOSITE**” which is being submitted to the **National Institute of Technology Karnataka, Surathkal** in partial fulfillment of the requirements for the award of the Degree of **Doctor of Philosophy** in **Department of Mechanical Engineering** is a *bonafide report of the research work carried out by me*. The material contained in this Research Thesis has not been submitted to any University or Institution for the award of any degree.

Register Number : **197002ME004**

Name of the Research Scholar : **BHARATH H S**

Signature of the Research Scholar : Bharath

Department of Mechanical Engineering

Place : **NITK, Surathkal**

Date : **August 17, 2021**

C E R T I F I C A T E

This is to *certify* that the Research Thesis entitled “**MECHANICAL CHARACTERIZATION OF 3D PRINTED CORE AND SANDWICH COMPOSITE**” submitted by **Mr. BHARATH H S** (Register Number: **197002ME004**) as the record of the research work carried out by him, is *accepted as the Research Thesis submission* in partial fulfillment of the requirements for the award of degree of **Doctor of Philosophy**.

Research Guide



Dr. Mrityunjay Doddamani

Assistant Professor

Department of Mechanical Engineering



Chairman – DRPC

Date: **August 17, 2021**

ACKNOWLEDGEMENT

I would like to extend my sincere gratitude to Dr. Mrityunjay Doddamani, Assistant Professor, Mechanical Engineering Department for the invaluable constructive guidance and encouragement extended throughout my study. I would like to thank Research Progress Assessment Committee members, Prof. G. C. Mohan Kumar and Dr. Raviraj H. M. for their valuable inputs.

I would like to thank Prof. S. M. Kulkarni, Head of Mechanical Engineering Department and all the faculty members at Mechanical Engineering Department for their support throughout this research work.

Constant encouragement of family members, my parents Dakshayani C B (mother), H S Siddappa (father), Veeregowda B N (father in law), Geetha G M (mother in law) to pursue higher studies has made it possible for me to reach at this stage. I wish to thank all my family members for love, help and encouragement provided. I thank my wife, Triveni B V and my son Master Nibhish H B for being with me in this research journey.

I express my sincere thanks to my lab mates Mr. Praveen, Mr. Sailesh R, Mr. B Dilip and Advanced Manufacturing Lab research team for their help and kind cooperation extended throughout this research work. Special note of thanks to all my friends and well wishers for their constant help, encouragement and understanding.

ABSTRACT

Fused filament fabrication (FFF) is one of the most widely used additive manufacturing (AM) techniques to fabricate lightweight complex functional parts with zero tooling cost, lower energy, and reduced material consumption. Three-dimensional (3D) printed lightweight hollow particle-filled syntactic foam core, and sandwich composites are developed using the FFF process in the present work. Hollow glass micro balloons (GMBs) are used as filler particles, and high-density polyethylene (HDPE) is used as matrix material. Hollow GMBs have blended with HDPE matrix by 20, 40, and 60 volume % to form GMB/HDPE blends. These blends are extruded using a single screw extruder to develop lightweight feedstock filaments to be used as input in a 3D printer to print syntactic foam core and sandwich composites. The suitable extruder parameters are chosen to ensure a homogeneous mixture of constituent materials and develop syntactic foam filaments with minimum or no GMB particle breakage.

Before printing of syntactic foam core and sandwich structures, the melt flow index (MFI), differential scanning calorimetry (DSC), coefficient of thermal expansion (CTE) and rheological properties of GMB/HDPE blends are studied to optimize the 3DP parameters. An increase in GMB content reduces MFI owing to the filler resistance to HDPE flow. MFI decreased by 23.29, 54.79, and 72.97%, increasing GMB by 20, 40, and 60 vol. %, respectively. A decrease in crystallinity (56.68%) for foam filaments is observed with increasing GMB % compared to HDPE. Compared to filaments, the corresponding prints have higher crystallinity and are anticipated to provide higher dimensional stability and reduce warpage-related issues. CTE values qualitatively exhibit warpage and dimensional stability information of 3D printed HDPE and foam samples. The addition of GMB in the HDPE matrix lowers CTE values. At higher printing temperatures, dimensional stability can be achieved by adding GMB into HDPE. This indicates that the warpage can be avoided to a greater extent in printed components with dimensional stability and lower residual thermal stresses. An increase in filler infusion increases the melt viscosity of the polymer and is observed in the entire frequency sweep during the rheological study of GMB/HDPE

blends. At a higher frequency, HDPE shows a shear-thinning region. Similar behavior is observed in foams with a marginal increase in complex viscosity. With the increase in filler content and frequency, both storage and loss modulus are increased. All these properties act as a guideline for selecting appropriate process parameters for the printing of quality components.

The performance and behavior of extruded foam filaments are influenced by the interaction of the filler–matrix, filler %, and matrix porosity. For filaments to be used in a 3D printer, adequate spooling stiffness and strength are needed. Hence, tests to find the density and morphology of the extruded filament and tensile properties are performed before printing to check the quality, stiffness, and strength necessary for filament feasibility to be used in a commercially available printer. HDPE filament's experimental and theoretical densities are very close, indicating lower void formations because of its hydrophobic nature. An increase in GMB content increases void content in filaments (0.84 - 7.70%) and prints (2.42 - 9.73%). Higher void content in print, as compared to filaments, indicate that matrix porosity is transferred from the filament to prints. Such porosity in prints amid 100% infill is because of air gaps between the raster (residual micro-porosity). These porosities form three-phase (HDPE, GMB, and raster gap) syntactic foams enhancing the damping capabilities. Tensile testing of extruded filaments is carried out to know its feasibility in a 3D printer. Stiffer intact GMB particles increase filament modulus by 8 - 47% in H20, H40, and H60, respectively, compared to neat HDPE. H20 exhibits more than 40% strain with the highest ultimate tensile strength (UTS) of 12.63 MPa among foams. In comparison, H60 exhibits the highest modulus because of a higher number of intact GMB particles. Strength decreases with increasing filler content as with increasing GMB content, HDPE volume decreases, lowering the ductile phase substantially. Pilot investigations are carried out to propose the suitable printing parameters for printing core (H20-H60) and sandwiches (SH20-SH60) by exploiting Nozzle - 1 and Nozzle - 2 available on the commercial FFF-based printers. GMBs presence in the HDPE matrix reduces the co-efficient of thermal expansion leading to lower warpage and samples with dimensionally closer tolerance. Several initial trials in the pilot

investigations did not yield high-quality prints. The reasons for such observations and the possible solutions are discussed that result in sound quality core and sandwiches. Tensile testing of 3D printed samples exhibits similar behavior as that of respective filaments. Among foams, H60 displays the highest modulus and is 48.02% higher than the HDPE print. H20 shows up to 30.48% strain. In HDPE, a long necking region is observed due to raster fibrillation leading to the broom-like fibrous ends. A typical brittle fracture is observed in H40 and H60. 3D printed HDPE and foams modulus is better than respective filaments. The flexural testing of HDPE and syntactic foam core and sandwich composites are carried out in a three-point bending configuration. Foams displayed brittle fracture as compared to neat HDPE, which did not fail until 10% strain. GMB inclusion induces brittleness in the compliant HDPE matrix. An intact GMB particle increases the flexural modulus with higher filler loadings. The H60 modulus is 1.37 times higher than HDPE, while strength is observed to be decreased. Lower strength values are due to the poor interface bonding between constituent elements and raster gaps. Similar behavior is observed in flexural testing of syntactic foam-cored sandwich samples. SH20 did not fail until 10% strain and registered the highest strength as compared to other sandwiches. SH40 and SH60 showed a brittle fracture. SH60 showed the highest modulus compared to other sandwich compositions. The flexural strength of syntactic foam cored sandwich samples are higher than their respective cores. The mechanics of composite beam theory is used for theoretical calculations of critical load. The deviation between the experimental and theoretical loads is noted to be in very good agreement, up to half of the maximum load. The failure mode of sandwich structures is analysed, and it is observed that SH40 and SH60 showed indentation failure. None of the samples failed in shear. All the samples except SH20 fractured in an approximately straight line just below the loading point.

Compressive responses of 3D printed core and sandwich samples are investigated at a constant crosshead displacement rate of 0.5 mm/min. The data is analysed using in-house developed MATLAB code to estimate yield strength and modulus for all the samples. HDPE exhibits a higher modulus and is 1.06 times higher than H60. The modulus of foam samples increases with GMB content. H60 displayed the highest

modulus among foams due to the presence of intact GMBs at higher filler loading. HDPE displayed 1.23 times higher yield strength compared to H60 samples. The Yield strength of syntactic foams decreases with an increase in filler loading because of poor interface bonding between constituent elements and residual micro-porosities. Similar behavior is observed in sandwich samples as well. Among sandwiches, SH20 has higher yield strength, and SH60 has the highest modulus.

The buckling and vibration response of 3D printed foams subjected to axial compression is investigated. The buckling load is estimated using Modified Budiansky Criteria (MBC) and Double Tangent Method (DTM) through the load-deflection plots. The first three natural frequencies and their mode shapes are computed as a function of axial compressive load. It is noted that the natural frequency reduces with an increase in axial compressive load. It is also observed that with an increase in GMB %, the natural frequencies and critical buckling load increase. Analytical solutions obtained from the Euler-Bernoulli-beam theory are compared with experimental results. Similar behavior is observed for sandwich samples that displayed global buckling mode during the buckling test, wherein the maximum deflection is reported at the mid-section with no signs of skin wrinkling, delamination, and skin micro buckling. The load-deflection data and frequency obtained experimentally are compared with numerical predictions deduced using finite element analysis (FEA), which is noted to match well. The comparative analysis of 3D printed samples is carried out with samples developed using other thermoplastic manufacturing routes through property maps for specified test conditions. The current work successfully demonstrated the development of lightweight feedstock filament intending to widen available material choices for commercially available 3D printers.

Keywords: *Syntactic foam filament; 3D printing; FFF; High density polyethylene; glass micro balloons; Crystallinity; CTE; Mechanical properties.*

CONTENTS

Declaration	
Certificate	
Acknowledgement	
Abstract	
CONTENTS.....	i
LIST OF TABLES	viii
ABBREVIATIONS	x
NOMENCLATURE	xi
1 INTRODUCTION	1
1.1 Composite Materials	1
1.2 Syntactic Foams	3
1.2.1 Filler/Reinforcement	5
1.2.2 Matrix.....	7
1.3 Sandwich composites.....	8
1.4 Processing of Syntactic foams	11
1.4.1 Compression Molding.....	13
1.4.2 Injection Molding.....	13
1.4.3 Additive Manufacturing (AM).....	15
1.5 Review of Literature	20
1.6 Motivation of work	43
1.7 Objectives and scope of the work	43
1.8 Thesis Outline	45
2 MATERIALS AND METHODS.....	46
2.1 Constituent Materials	46
2.1.1 Glass microballoons.....	46
2.1.2 Matrix.....	47
2.2 Blend preparation.....	47
2.3 Melt Flow Index (MFI).....	49
2.4 Rheological study of GMB/HDPE blends	50
2.5 Filament development and 3D Printing	50
2.6 Differential scanning calorimetry (DSC).....	54

2.7	Coefficient of thermal expansion (CTE).....	55
2.8	Density	55
2.9	Tensile response.....	56
2.10	Flexural behavior of 3D printed core and sandwich.....	56
2.11	Compression response of 3D printed core and sandwich	57
2.12	Buckling and free vibration investigation.....	57
2.12.1	Buckling of 3D printed core	57
2.12.2	Free vibration of 3D printed core.....	59
2.12.3	Bradella-Genna model for estimating young's modulus	59
2.12.4	Theoretical formulation	60
2.12.5	Vibration correlation technique (VCT).....	63
2.12.6	Buckling of 3D printed foam cored sandwich	63
2.12.7	Numerical analysis.....	65
2.13	Microstructural characterization	66
3	MATERIAL CHARACTERIZATION AND PROCESSING ASPECTS	68
3.1	Blend characterization	68
3.1.1	MFI of HDPE and GMB/HDPE blends.....	68
3.1.2	Rheology of HDPE and GMB/HDPE blends	68
	<i>Frequency sweep</i>	68
	<i>Temperature sweep</i>	69
3.2	Filament development.....	71
3.3	3D printing of syntactic foam core and sandwich	74
3.4	DSC investigations of filament and 3D prints	81
3.5	CTE of prints.....	82
4	TENSILE BEHAVIOR.....	84
4.1	Tensile behaviour of HDPE and foam filament.....	84
4.2	Tensile behaviour of 3D prints	86
4.3	Property map.....	88
	Conclusions.....	90
5	FLEXURAL RESPONSE.....	92
5.1	Flexural behavior of 3D printed core.....	92
5.1.1	Property map.....	95
5.2	Flexural behavior of 3D printed sandwich.....	97

5.2.1	Comparison of core and sandwich flexural properties	101
5.2.2	Theoretical prediction of sandwich properties.....	101
5.2.3	Failure mode of 3D printed sandwich.....	105
	Conclusions.....	107
6	COMPRESSIVE BEHAVIOR	109
6.1	Compressive behavior of 3D printed core	109
6.2	Compressive behavior of 3D printed sandwich.....	113
	Conclusions.....	117
7	BUCKLING AND FREE VIBRATION RESPONSE	118
7.1	Buckling and free vibration of foam core under axial compression.....	118
7.1.1	Buckling investigation	118
7.1.2	Natural frequency of prints	121
7.1.3	Critical buckling load estimation using VCT	123
7.1.4	Property map.....	124
7.2	Buckling and free vibration of printed sandwiches under axial compression	126
7.2.1	Buckling behavior.....	127
7.2.2	Free vibration response.....	130
7.2.3	Comparative analysis	132
	Conclusions.....	135
8	3D PRINTED INDUSTRIAL COMPONENTS	137
	SUMMARY AND CONCLUSIVE REMARKS	140
	SCOPE OF FUTURE WORK	144
	REFERENCES	145
	LIST OF PUBLICATIONS	171
	BIO-DATA	172

LIST OF FIGURES

Figure 1.1 Composites based on filler types.....	2
Figure 1.2 Different structures of SFs.....	4
Figure 1.3 Micrograph of as received GMB particles.	6
Figure 1.4 Polymer consumption in India (Shekhar 2012).....	8
Figure 1.5 The structure of a sandwich composite.	9
Figure 1.6 Representation of reinforced syntactic foam fabrication method.....	12
Figure 1.7 Constituents of PMCs and manufacturing options (Reinhart 1998).	12
Figure 1.8 Work flow of AM/3DP.....	16
Figure 1.9 Schematic of FFF process.	18
Figure 2.1 As received (a) GMB in powder form and (b) HDPE granules used in the present work.	47
Figure 2.2 (a) Brabender (b) blending mechanism and (c) GMB/HDPE blend from brabender.	48
Figure 2.3 Flow chart of the present study.	49
Figure 2.4 Melt flow indexer (Dynisco LMI5000).....	50
Figure 2.5 (a) Schematic representation of the industrial scale single screw extruder and (b) experimental setup.	52
Figure 2.6 (a) Schematic representation of FFF printer and (b) FFF printer utilized in the present work.....	53
Figure 2.7 Schematic of the experimental setup utilized for mechanical buckling and vibration under a compressive load.	58
Figure 2.8 Representative load-deflection plots for estimating P_{cr} using (a) DTM and (b) MBC for representative H20 print.	58
Figure 2.9 Schematic diagram of specimen used in free vibration test.	59
Figure 2.10 Schematic representation of the (a) experimental setup and (b) sample configuration.....	65
Figure 2.11 (a) Numerical analysis steps and (b) FEA Model of the Sandwich composite. ..	66
Figure 3.1 (a) Complex viscosity (b) storage modulus and (c) loss modulus as a function of frequency for HDPE and their blends.....	69

Figure 3.2 (a) Storage modulus (b) loss modulus and (c) $\tan \delta$ as a function of temperature for HDPE and their blends.....	70
Figure 3.3 Representative extruded H60 feedstock filament.....	72
Figure 3.4 Extruded filament micrograph of (a) cross-sectional view for representative H20. H60 at (b) lower and (c) higher magnifications.....	73
Figure 3.5 Challenges in 3D printing of HDPE (Table 3.2) (a) Improper layer deposition (b) Interlayer defects (c) excessive diffusion (d) maximum warpage and (e) defect free print. ..	75
Figure 3.6 Micrograph of printed (a) H in thickness direction and (b) freeze fractured across the thickness.....	76
Figure 3.7 Prints with different (a) N1 and (b) N2 temperatures.....	78
Figure 3.8 Prints with (a) different combination of bed and chamber temperatures and (b) different printing speeds.	78
Figure 3.9 Micrograph of printed (a) H60 and (b) associated raster gaps (residual micro-porosity) in H60.....	79
Figure 3.10 As printed freeze fractured micrograph of sandwich (a) across the thickness and (b) along the thickness.	80
Figure 3.11 DSC for crystallization peaks: Cooling cycle in (a) filaments and (c) prints. Melting peaks from heating cycle (2 nd) in (b) filaments and (d) prints.	82
Figure 4.1 Representative filament stress-strain plot of (a) H and (b) H20 - H60. Micrographs of (c) H20 and (d) H60 filament post tensile tests.....	85
Figure 4.2 Fractographic analysis of representative 3D printed (a) H (Patil et al. 2019) and (b) H60 post tensile test.	87
Figure 4.3 Tensile (a) modulus and (b) strength of HDPE composite (Jayavardhan and Doddamani 2018, Jayavardhan et al. 2017, Kumar et al. 2016).....	89
Figure 5.1 (a) Representative H60 mounting in flexure mode (b) yielding (c) and crack initiation.....	93
Figure 5.2 Representative (a) stress-strain plots for prints (b) flexural modulus (c) flexural strength as function of GMB % and (d) H60 micrograph showing raster gaps.....	93
Figure 5.3 Micrographs of post flexure tested (a) H20 (b) H40 and (c) H60 printed cores. ..	94
Figure 5.4 Flexural (a) modulus and (b) strength of HDPE composite (Jayavardhan and Doddamani 2018, Jayavardhan et al. 2017, Kumar et al. 2016).....	96

Figure 5.5 Freeze fractured micrographs of (a) SH20 (b) SH40 and (c) SH60 at skin-core interface.....	98
Figure 5.6 Flexural test of representative SH20 (a) yielding and (b) maximum mid-point deflection.....	99
Figure 5.7 (a) Stress - strain plots (b) Modulus and (c) strength as function of GMB content in printed sandwiches.....	100
Figure 5.8 SEM of post flexure tested representative (a) SH20 and (b) SH60.....	100
Figure 5.9 Flexural (a) strength and (b) modulus comparison for printed Core and Sandwich.	101
Figure 5.10 (a) Print dimensions and flexural test configuration (b) Schematic representation of sandwich with the terminologies.	102
Figure 5.11 Sandwich experimental and theoretical comparison of (a) flexural modulus (b) critical load and (d) force–deflection plots. Note: T denotes “theoretical”.	105
Figure 5.12 Schematic representation of (a) core indentation and (b) failure modes observed in 3D printed SF core sandwiches (c) face wrinkling in SH20 and (d) indentation failure (SH40 and SH60).....	107
Figure 6.1 (a) Experimental setup (b) compressive stress-strain plots for HDPE (c) foam (d) H20 - before and after compression (e) compressive modulus and (f) yield strength as function of GMB Vol. %.	111
Figure 6.2 Micrographs of compressive tested H20 (a-b) H40 (c-d) and H60 (e-f).....	112
Figure 6.3 (a) Experimental setup (b) sandwich compressive stress-strain plots for 3D printed sandwich (c) SH60 before and after compression (d) compression modulus and (e) yield strength as function of GMB Vol. %.	114
Figure 6.4 Compression property comparison of 3D printed core and sandwich.	115
Figure 6.5 Compressive tested SH20 (a-b) SH40 (c-d) and SH60 (e-f).	116
Figure 7.1 Micrographs of 3D printed freeze fractured (a) H (b) H20 (c) H40 and (d) H60.	118
Figure 7.2 (a) 3D printed representative foam sample being tested and (b) plots showing buckling behavior of prints.	120
Figure 7.3 FRF of H60 at no load condition.	121

Figure 7.4 Natural frequency vs. compressive load for representative (a) H (b) H20 (c) H40 and (d) H60.	122
Figure 7.5 (a) Critical Buckling load for H – H60 using VCT and (b) comparison of critical buckling load through VCT, DTM and MBC.....	124
Figure 7.6 Buckling load as a function of density (Rajesh and Pitchaimani 2017, Waddar et al. 2018, Waddar et al. 2018).....	125
Figure 7.7 Concurrently 3D printed representative SH60.	126
Figure 7.8 Micrographs of (a) SH20 core and (b) concurrently 3D printed SH60 across the thickness.....	127
Figure 7.9 Load-deflection behavior of (a) printed HDPE and sandwich (b) comparative analysis of representative H20 and SH20 and (c) buckled representative SH60.....	129
Figure 7.10 FRF curve of representative SH20 under axial compression.	131
Figure 7.11 Axial compressive influence on the natural frequencies of (a) 1 st (b) 2 nd and (c) 3 rd modes.....	132
Figure 7.12 Experimental and ANSYS comparative plots for (a) SH20 (b) SH40 and (c) SH60.	134
Figure 7.13 First Buckling mode shape of representative SH20.	134
Figure 8.1 Representative components printed using H60 1. Hard disk fan cover 2. Hard disk cooling fan 3. External device connector - top case 4. External device connector - colling fan unit 5. External device connector - lower case 6. Power pac - lower case 7. Power pac - top case and 8. Thrust propeller.	138

LIST OF TABLES

Table 1.1 AM process categories (ASTM F2792-10).	17
Table 1.2 Thermoplastics for FFF.	21
Table 2.1 Properties of iM30K hollow glass microballoons*.	46
Table 2.2 Characteristics of HDPE grade HD50MA180*.....	47
Table 2.3 Single screw extruder specifications.....	52
Table 2.4 Specifications of FFF based 3D printer.	54
Table 3.1 Physical Properties of Filament (F) and Prints (Pnt).....	72
Table 3.2 Remarks on different 3D printing parameters.	74
Table 3.3 Experimental test observations during 3DP of SF cored sandwiches.	77
Table 3.4 Suitable printing parameters used to print core and sandwich.	79
Table 3.5 Thermal behaviour of H - H60.	81
Table 3.6 CTE of printed samples.	83
Table 4.1 Tensile properties of filament and 3D prints.	86
Table 4.2 Weight saving quantification parameters of H - H60.	88
Table 5.1 Flexural Response of H - H60 Prints.....	94
Table 5.2 Physical properties of the printed sandwiches.....	97
Table 5.3 Flexural response of sandwich prints.....	99
Table 5.4 Experimental and theoretical critical load estimations.	104
Table 6.1 Compressive properties of 3D printed H - H60.....	111
Table 6.2 Specific compressive properties of 3D printed H - H60.....	111
Table 6.3 Compressive properties of 3D printed sandwiches.....	114
Table 6.4 Specific properties of 3D printed sandwich samples.....	114
Table 7.1 Experimental and theoretical critical buckling load for 3D prints.....	119
Table 7.2 Modulus comparison between the frequency data and Bardella-Genna model for 3D prints.....	120
Table 7.3 P_{cr} of printed sandwiches.....	129
Table 7.4 P_{cr} estimations through DTM and MBC methods.	130
Table 7.5 Natural frequency estimations through experimental route of all the prints.	131
Table 7.6 Young's moduli predictions through Bardella-Genna model.....	133
Table 7.7 P_{cr} using experimental and numerical approaches.....	134

Table 7.8 Comparison of natural frequencies at no load condition.	135
Table 8.1 Details of 3D printed components.	139

ABBREVIATIONS

ASTM	: American Society for Testing and Materials
AM	: Additive Manufacturing
CTE	: Coefficient of Thermal Expansion
CM	: Compression Molding
DAQ	: Data Acquisition System
DSC	: Differential Scanning Calorimetry
DTM	: Double Tangent Method
FFF	: Fused Filament Fabrication
FFT	: Fast Fourier Transform
FDM	: Fused Deposition Modeling
GMB	: Glass Microballoon
HDPE	: High Density Polyethylene
MBC	: Modified Budiansky Criteria
MFI	: Melt Flow Index
PMC	: Polymer Matrix Composite
QCM	: Quartz Crystal Microbalance
SEM	: Scanning Electron Microscope
SF	: Syntactic Foam
UTS	: Ultimate Tensile Strength
VCT	: Vibration Correlation Technique
3DP	: 3 Dimensional Printing

NOMENCLATURE

ω_j	Angular natural frequency	rad/s
K_{bulk}	Bulk modulus	MPa
T_{Melt}	Crystallization temperature	°C
η'	Complex viscosity	Pa.s
P_{cr}	Critical buckling load	N
β_j	Constant parameter	-----
α	Constant parameter	-----
A	Cross-sectional area	m ²
E_c	Core Modulus	MPa
A_s	Cross-sectional area of skin	mm ²
A_c	Cross-sectional area of core	mm ²
ρ	Density	kg/m ³
ρ_c	Density of the composite	kg/m ³
ρ_f	Density of the filler	kg/m ³
ρ_m	Density of the matrix	kg/m ³
α_{Cryst}	Degree of crystallinity	%
$Tan \delta$	Damping factor	-----
δ	Deflection	mm
d	Distance between centers of skin	mm
Y	Distance between base to centroid axis	mm
Y_s	Distance between the neutral axis of the sandwich to centroid axis of skin	mm
Y_c	Distance between the neutral axis of the sandwich to centroid axis of core	mm
ρ_{exp}	Experimental density	kg/m ³
I_{eq}	Equivalent moment of inertia	mm ⁴
E_{fM}	Flexural modulus	MPa
σ_{fS}	Flexural strength	MPa

ΔH_m	Heat of fusion	J g^{-1}
ΔH_m^*	Heat of fusion per gram for 100% crystalline HDPE	J g^{-1}
P	Load	N
G''	Loss modulus	Pa
T_{Cryst}	Melting peak temperature	$^{\circ}\text{C}$
$Y(x)$	Modal displacement	m
I	Moment of inertia	m^4
M	Moment of resistance	N-mm
I_c	Moment of inertia of core	mm^4
I_s	Moment of inertia of skin	mm^4
Y_{max}	Maximum distance of skin from neutral axis	mm
f	Natural frequency	Hz
ϑ	Poisson's ratio	-----
ϑ_m	Poisson's ratio of matrix	-----
ϑ_f	Poisson's ratio of filler	-----
η	Radius ratio	-----
V	Relative axial force	N
Ω	Relative natural frequency	Hz
$(AG)_{eq}$	Shear rigidity	MPa
E_s	Skin Modulus	MPa
G'	Storage modulus	Pa
G	Shear modulus	MPa
m	Slope	-----
t	Thickness of Skin	mm
c	Thickness of Core	mm
I_t	Total moment of inertia	mm^4
ρ_{th}	Theoretical density	kg/m^3
y	Transverse displacement	m
h	Total thickness of the sample	mm

L	Unclamped specimen length	mm
σ_{fmax}	Ultimate Stress	MPa
Φ_V	Void content	%
V_m	Volume fraction of matrix	%
V_f	Volume fraction of filler	%
b	Width of the sample	mm
W_{GMB}	Weight fraction of GMB	%
E	Young's modulus	MPa

1 INTRODUCTION

1.1 Composite Materials

Increasing performance demands for modern technology applications make it necessary to look for new materials. Achieving significantly higher and specific quality standards using single materials are challenging. Thereby, materials are developed by combining two or more conventional materials to achieve a unique combination of properties known as composite materials. According to the ASM Handbook (ASTM D3878-18), composite materials are the macroscopic mixture of two or more different materials with a visible interface between them. These materials improve the overall efficiency of the structure by reducing the weight of the components. Because of their superior properties, such as higher specific modulus, higher strength, and structural designability, composite materials have a wide range of applications in challenging areas such as space vehicles, wind power generators, and rail transit (Zhu et al. 2011). Composites have notable applications in airplanes; for example, in Boeing 787, nearly 50% of the entire aircraft account for composite materials. Further, the latest version of Airbus, A350, has a 53% share of composite materials (Tang et al. 2018). Composite properties can be tailored to meet specific design requirements, directional and structural properties. Nowadays, many researchers are developing hybrid composites by changing the orientation of fibers, volume fraction, etc., to achieve enhanced properties (Gangil et al. 2019, Hemath et al. 2020, Laishram et al. , Sachinkumar et al. 2020).

The composite material is defined by its matrix and reinforcements materials (Chawla 2001). Matrix is a continuous phase, while the reinforcement is either a continuous or a discontinuous phase. The third phase of the composite is the interface between matrix and reinforcement. Composites are classified as Polymer matrix composites (PMC), Ceramic matrix composites (CMC), and Metal matrix composites (MMC) based on matrix material. The growing demand for lightweight materials (Matli et al. 2020) in all fields results in the rapid development of PMCs in recent years. Because of their desirable combination of mechanical properties, PMCs are becoming a promising material for various structural and automotive applications (Benchechou et al. 1998). PMCs are extensively used in aerospace, electronics engineering, and day-to-day consumer industries due to their lower density, good

thermal/electrical characteristics, better chemical inertness and easier manufacturing routes. Figure 1.1 represents the classification of composites based on the nature of reinforcements (Agarwal and Broutman 1980).

Thermoset and thermoplastic polymers are the two types of widely used polymers. Since the chains are rigidly linked with tight covalent bonds, thermosetting polymers are insoluble and infusible after cure. Commonly found thermoplastic in everyday life are phenolic, melamine, vinyl esters, vulcanized rubber, epoxy resin, and silicones. The bonds in thermoplastics are fragile and of the Van-der-Waal type, making them form high temperatures and pressure. Some common examples of thermoplastics are polyvinyl chloride, polybenzimidazole, polyethylene, acrylic, polypropylene, Teflon, and nylon. PMCs consist of a thermoplastic or thermosetting resin reinforced by fillers like fibers, particles, etc. PMCs have excellent specific properties due to the lower density of the constituents. Compared to metals and ceramics, polymers have low strength and stiffness. Nonetheless, their properties can be enhanced by reinforcing fillers. In addition, PMCs' processing does not require high pressure and temperature and can be easily molded to a variety of shapes and sizes. PMCs have less issue with reinforcement deterioration during manufacturing than composites with other matrices. Furthermore, the equipment needed for PMCs has fewer complexities.

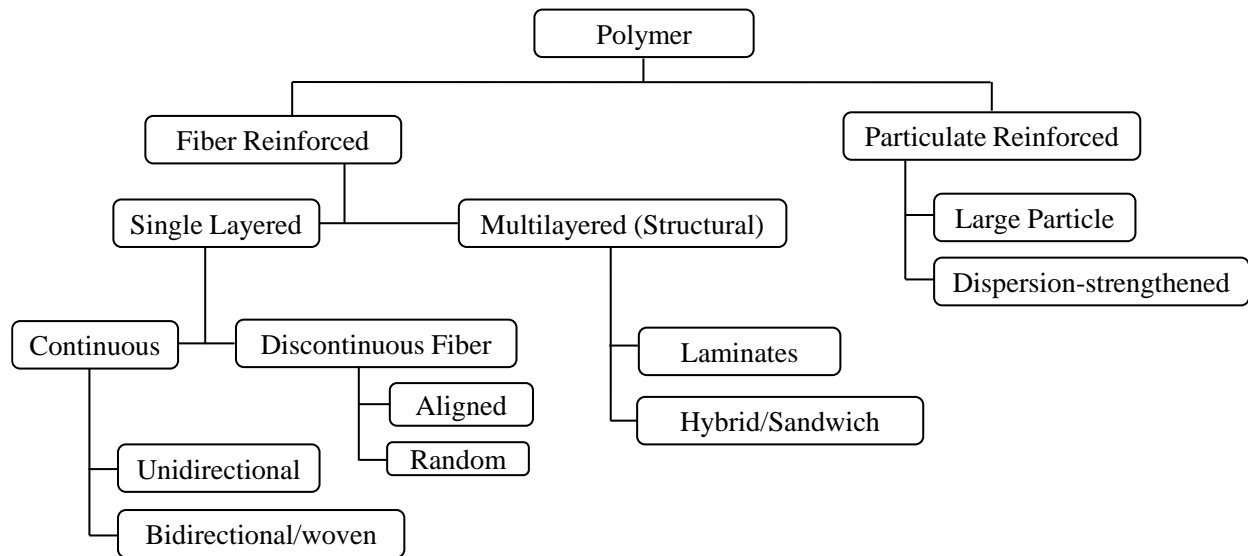


Figure 1.1 Composites based on filler types.

Composites, especially with the focus on lightweight materials, syntactic foam (SF) composites are undoubtedly superior to other conventional composites for weight savings without compromising structural performance. Due to their high specific strength, low moisture absorption, bending stiffness, and excellent damping properties, SFs are treated as a special class of structural composite and have become very common in recent years. The low density of SF enables them to be ideal materials for space, marine, sports, and aeronautical applications (Gupta and Woldesenbet 2004). SFs are lightweight porous composites that are developed as buoyancy support materials for deep-sea applications (Malloy et al. 1990) in addition to their usage in aircraft, spacecraft, and ship structures (Bardella and Genna 2001). SFs can also be used in the thermal insulation of pipelines in the oil and gas industry due to their higher porosity fractions. SFs are also used in electronic packaging, composite tooling, and thermoforming plug assists due to their lower coefficient of thermal expansion and dimensional stability at higher temperatures. The possibility of tailoring the mechanical and thermal properties of SFs by proper selection of material combinations, hollow particle volume fraction, and hollow particle wall thickness has helped in rapidly growing these applications. One of the most significant advantages of syntactic foams over traditional particulate and fibrous composites is their ability to design and fabricate according to the application's physical and mechanical property requirements (Gupta et al. 2005).

1.2 Syntactic Foams

Syntactic foams are particulate composites developed in the 1960s and are used in marine structures due to their naturally buoyant behavior and low moisture absorption. These foams are multi-functional due to their wide range of mechanical properties, and hence they are used as core material in the sandwich composite for lightweight applications (Breunig et al. 2020). Syntactic foams are realized by mixing hollow filler particles (micro balloons/microspheres/cenospheres) in the matrix material. A variety of thermoplastic and thermosetting polymers are being used as the matrix resin, depending on the operating conditions (Doddamani and Kulkarni 2011). Similarly, microballoons made of silicone, ceramic, or metal may also be selected depending on availability (Gupta et al. 2013). These foams have low thermal conductivity and high specific strength (Gupta et al. 2005). The buoyancy offered by SFs with higher compression strengths and modulus are crucial for

weight sensitive structural applications (Kulkarni et al. 2021). One of the important advantages of these foams is their ability to produce composites with the required properties for a specific application.

The structure of SF has two phases, namely matrix resin, and microballoons. There are two types of foams, namely, open-cell and closed cell. Open-cell foams are cellular material and always find limitations because of low compressive modulus and strength (Gupta et al. 2004). To overcome these issues, closed-cell foams known as syntactic foams are developed (Puterman et al. 1980). Nevertheless, during the production of SFs, some air is inevitably trapped in the structure and is present as open-cell structured porosity. This entrapped air is referred to as voids, making these foams three-phase structures (matrix, microballoons, and voids). Similarly, SFs, when reinforced with fibers, results in a multi-phase structure. Figure 1.2 presents SFs structure.

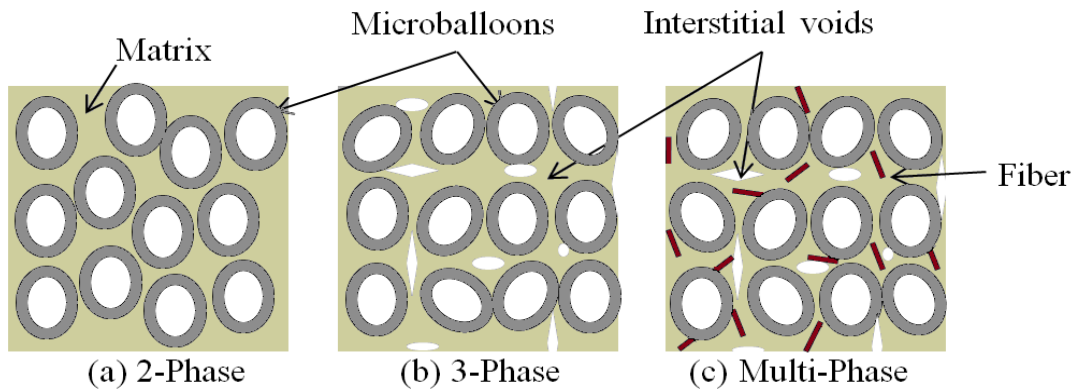


Figure 1.2 Different structures of SFs.

Closed-cell foams or syntactic foams provide greater versatility in designing structural applications. Hence, by changing the volume % of these hollow fillers in the matrix, tailor-made properties can be achieved for many different applications (Gupta and Ricci 2006, Jayavardhan and Doddamani 2018). Achieving these properties depends on the particle survival in these lightweight foams and processing methods used for synthesizing them (Jayavardhan et al. 2017, Kumar et al. 2016). Hence it is worth characterizing these materials for mechanical behavior synthesized through advanced manufacturing methods like 3D Printing.

1.2.1 Filler/Reinforcement

The property requirements and envisaged applications govern filler selection. Inorganic and organic solid fillers have been used extensively in thermoplastic industries (Chen et al. 2006, Gwon et al. 2012, Liu et al. 2008, Liu et al. 2009). Reinforcing filler particles in the matrix has several benefits, including a reduction in resin costs and flexibility in tailoring properties (Annigeri and Veeresh Kumar 2018, Ou et al. 2014). Mechanical, surface, electrical, and magnetic properties can be altered using fillers (Jayavardhan and Doddamani 2018, Jayavardhan et al. 2017). Many reinforcements in polymers can be added including ceramics, mineral particles, metal, polymer, and various industrial wastes (Shaikh and Channiwala 2006). The most commonly used fillers are Al_2O_3 (Singh et al. 2016), glass (Spoerk et al. 2018), iron particles (Masood and Song 2004), carbon, and glass fibers (Brenken et al. 2018). The filler choice is primarily governed by the target composite properties. The shape of the filler particles has a significant impact on the composite's properties. Spherical, blocks, cubical, flaky, and fibrous particles are some of the most common shapes of filler particles. Spherical particulate fillers are more popular than the other types due to the regularity of shape, high crush strength, low surface area to volume ratio, better rheology, closely controlled particle size, and control of surface properties (Ferrigno 1978).

In recent years, the use of hollow particles like glass microballoons (GMBs) and fly ash cenospheres has increased significantly in the development of low density and high damage-tolerant composites (Ashrith et al. 2019, Doddamani 2019, 2020, Shahapurkar et al. 2019). The reinforcing matrix with hollow fillers reduces the matrix volume %, leading to lightweight composite structures known as SFs. They have better mechanical properties and can produce complex functional parts that can replace high-cost resin, thereby lowering carbon footprints (Gupta et al. 2001, Satapathy et al. 2011). Naturally, available fly ash cenospheres have numerous surface defects (Garcia et al. 2018) compared to engineered glass microballoons. Hence, GMBs is the most commonly utilized filler. Introducing these hollow GMB particulate fillers in a matrix can significantly reduce weight and can be effectively exploited for weight-sensitive structures.

GMBs are a free-flowing powder that evolved from the production of solid glass beads in the year 1960. GMBs are developed commercially in several ways. GMBs are less expensive than polymeric ones due to developing process technology and raw material supply in many countries (Shutov 1986). GMBs are produced in a vertical tube furnace which is heated using gas that contains a mixture of propane-butane. At the bottom of the tube, a powder containing glass and a porofore is sprayed. Porofore is a chemical blowing agent that produces gas at the glass melting point and inflates partially fused monolithic particles. The microspheres are then brought to the top of the tube by the hot gas, where they are cooled and washed with water to eliminate defective microspheres. Then they are treated with acid to enhance their chemical resistance and increase their softening temperature (Shutov 1986). Sodium silicate microballoons are developed by combining sodium silicate with ammonium pentaborate subsequently spray-dried to form hollow microballoons (Lee 1992). The micrograph of as-received glass micro balloons is shown in Figure 1.3.

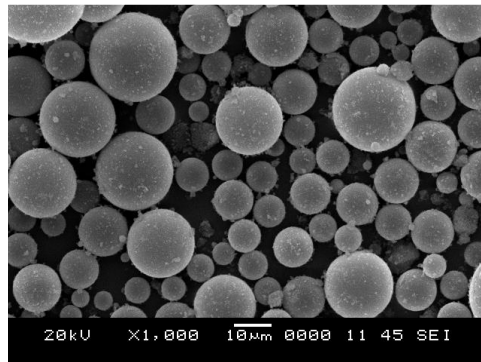


Figure 1.3 Micrograph of as received GMB particles.

GMBs come in various grades based on their physical properties like crushing strength, wall thickness, and density. The strength, density, chemical stability, water resistance, and alkalinity of hollow GMBs are the primary criteria for selecting them for a specific application. Weight (density) and strength are essential material properties and are crucial for aeronautical, naval, and automotive components. In manufacturing low-cost, lightweight thermoplastics without compromising the material's mechanical properties, GMBs are candidate fillers exhibiting promising behavior (Jayavardhan et al. 2017). Developing newer and useful systems using glass microballoons with near isotropy will be challenging and exciting.

1.2.2 Matrix

Polymers are materials formed out of long chains of repeated molecules. The repeating structural units are known as monomers held together by covalent bonds, and the process is known as polymerization. Polymers have desirable properties such as ductility, formability, and corrosion resistance (Srinivasan and Ramakrishnan 1983). The properties of the polymers depend on the type of molecules and bonding. Thermoplastic polymers (rubber, polyester, etc.) can be remolded without compromising their characteristics through continuous cooling and heating (Arzamasov B 1989). Whereas thermosetting polymers (epoxies, glass, etc.) are rough and durable, they remain rigid on heating unless they are turned to char (Arzamasov B 1989).

Commonly used thermoplastic polymers such as polymethylmethacrylate (Espalin et al. 2010), polylactide (Spoerk et al. 2017), acrylonitrile butadiene styrene (Dul et al. 2016), polycarbonate (Domingo-Espin et al. 2015), and polyetherimide (Arivazhagan et al. 2014). Thermoplastics are used in semi-structural and many engineering applications, as they are environmentally friendly and offer the flexibility of processing using various methods (Bharath Kumar et al. 2016). The word engineering plastics is emerged because of categorizing plastics that can effectively replace metals like aluminum in small devices and structures with low mechanical properties. Compared to traditional materials, engineering plastics are the primary source for creating composites with improved stiffness, strength-to-weight ratio, and chemical and atmospheric inertness (John and Nair 2014). Because of their intrinsic properties, polymer matrices are commonly used in composite materials. The cost of PMCs can be minimized by using low-cost fillers like hollow GMBs to reinforce the plastic. In India, the excessive use of plastic products in everyday life increased the demand for plastics. Polymers are used in almost every aspect of daily life like grocery bags, soda, and water bottles, cloth fabrics, tablets, computers, food containers, vehicle components, and toys. In 1997, India's estimated per capita plastic usage was 0.800 kg, one of Asia's lowest usages (Burgiel et al. 1994, Burgueno et al. 2004, Esha and Rajaram 1997, Scott 2000). In the year 2000 A.D., the estimated demand was 2.16 kg/capita (KSSPMA 1992). Since 1991, India has seen an increase in plastic usages because of economic liberalization. From 0.85 million tons in 1990-91 to 1.79 million tons in 1995-96, India's plastic usage has become

doubled. Commodity plastics demand is increasing at a rate of 15% per year. According to the All India Plastic Manufacturers Association, the total capacity to produce PVC, PS, PP, and PE is 1.39 million mega tones (MMT) in 1995, with demand increasing to 1.8-1.9 million mega tons in 1996-97. According to Plast India reports, this is distributed in three major sectors: infrastructure that includes 30 % of the total contributes to bridges, building, electricity, roads, and telecommunications; 25 % goes to packaging; and 24 % goes to water and agriculture (Nanavaty 1997). Figure 1.4 depicts India's polymer consumption in kilo tons (K_t). Polymers used in packaging account for about half of this consumption.

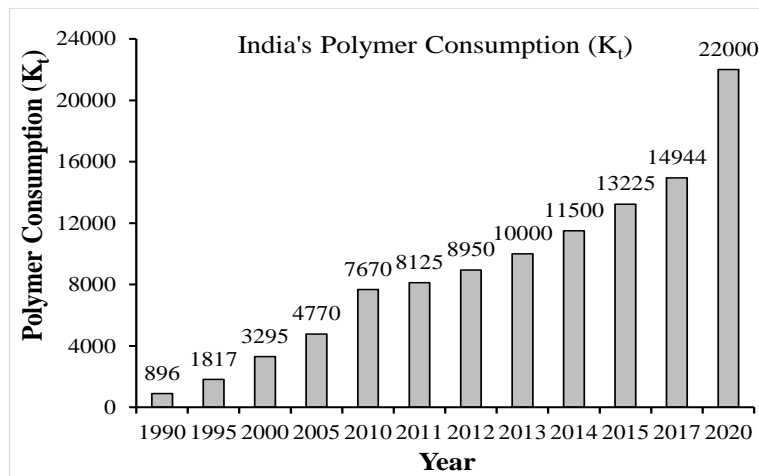


Figure 1.4 Polymer consumption in India (Shekhar 2012).

With the current growth rate in plastic consumption, thermoplastic syntactic foam composites with fillers such as hollow GMBs can prevent problems with plastic management and environmental issues. In addition, when a matrix is reinforced with fillers, the function of the interface between them, and associated compatibility problems must be addressed.

1.3 Sandwich composites

A sandwich structure comprises two thin, rigid facing sheets attached to either side of low-density core material or structure (Figure 1.5). With just a slight increase in weight, the separation of the facings by a lightweight core significantly increases the second moment of area of the material cross-section and thereby increases the bending stiffness. This is known as the “sandwich effect”. Sandwich materials can also provide many other advantages, such as functional integration, space savings, and modular construction, in addition to the

sandwich effect. Sandwich composite structures are widely explored in the marine, wind, civil, aerospace, and various other fields, due to the several significant advantages over traditional materials, like high specific strength, stiffness, high damping properties, excellent fatigue and corrosion resistance (Birman and Kardomateas 2018, Elamin et al. 2018, Mohamed et al. 2015, Thomsen 2009). Theories of sandwich-structured composites can be traced as early as 1849 CE (Noor et al. 1996). However, the ability of sandwich design is realized during World War II. Innovations in aerospace created a demand for lightweight structures with high strength that are highly resistant to damage. Composites with these properties are the first choice for many weight-sensitive applications.

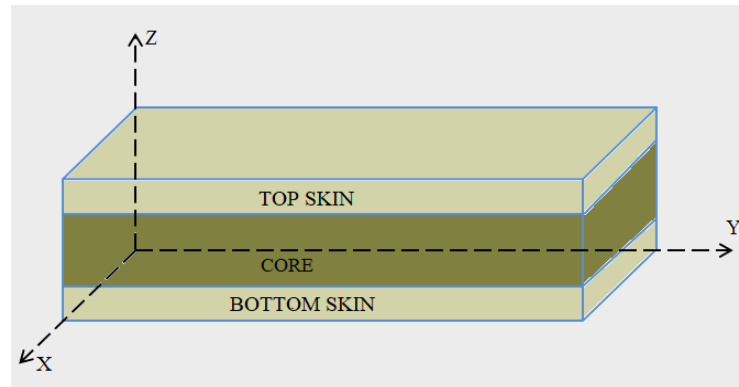


Figure 1.5 The structure of a sandwich composite.

Sandwich composites consist of a thick light-weight slab known as core to which two thin and stiff face sheets are attached, known as skin (Gupta et al. 2018, Gupta et al. 2018). The typical structure of sandwich composite is shown in Figure 1.5. The thickness of the core and skin depends on the required properties and specific applications. The selection of materials for sandwich composites depends on loading conditions, cost, quality, constituent materials availability, and functional requirements. Multilayered graphite and carbon epoxy facings are commonly used in aerospace structures, whereas glass epoxy or glass vinyl esters are being used in the frames of civil and marine systems (Birman and Kardomateas 2018). The design, thickness, and material of core and skin, orientation of material play an essential role in the load-bearing and damping properties of the sandwich structures (Yuan et al. 2012). The choice of appropriate matrix and filler materials, volume fractions of constituents make them achieve tailored properties. Many materials can be used as core based on application and

performance requirements (Vinson 1999). The commonly used core material can be low-density solid materials like open and closed cell foams structures, high-density material in cellular form like a honeycomb, high-density material in corrugated form like a truss, etc. The interface between the skin and core is affected by the core structure, which offers additional weightage for designing a sandwich structure according to requirements and operating conditions. The closed-cell foam core structure provides superior strength, higher moduli, lower moisture absorption, and resistance to flexure, impact, and blast in sandwich composites (Doddamani et al. 2011, Zhang et al. 2014, Zhang et al. 2016, Zhang et al. 2018). Tailor made properties can be achieved based on size, shape, and compositional elements of the pores.

Controlling the pore size and shape in foams is very critical in designing sandwich composites. The need for high strength and stiffness in sandwiches results in two distinct approaches (Yaseer Omar et al. 2015) of foams, sandwiching between stiffer face-sheets increasing flexural strength (Qin et al. 2014, Rajaneesh et al. 2014) and secondly, porosity integration using hollow particles resulting in effective reinforcing effect depending on their wall thickness and volume fraction. These foams filled with hollow particles are called SFs, as elaborately discussed earlier. These foams are multi-functional due to their wide range of mechanical properties, and hence they are used as core material in the sandwich composite for lightweight applications (Breunig et al. 2020, Waddar et al. 2018, Waddar et al. 2018, 2020, Waddar et al. 2019, Waddar et al. 2018). Nevertheless, the freedom of sandwich construction is not effectively studied (Doddamani and Kulkarni 2011). Still, only a few configurations, such as standard honeycomb (Petras 1999, Wang 2009, Yasui 2000), body-centered cubic lattice (Mines et al. 2013), pyramidal lattice (Wadley et al. 2003), square honeycomb (Park et al. 2012), tetrahedral lattice (Kooistra et al. 2008), diamond honeycomb (Wang and McDowell 2004), etc. are synthesized using conventional processing routes. Because of the production limitations, traditional production processes for sandwiches are limited for simple geometries (Dikshit et al. 2019). In handling extreme loads upon impact, intricate geometrical sandwich designs are essential. The multistage processing and associated tooling in conventional manufacturing pose challenges in realizing geometrically integrated complex-shaped sandwich composites. In addition, the traditional manufacturing

process involves adhesive bonding of the skin and core produced independently and requires a complex and expensive bonding process (Jakobsen et al. 2007, Karlsson and TomasÅström 1997, Ning et al. 2007). The bonding between skin and core plays a very vital role in load transfer. The differential stresses acting across the bonding interface, and the absence of parent material makes sandwiches weaker in the skin-core interface resulting in delamination/debonding and shear failure. Thereby, if sandwiches are realized as a concurrent structure, the inherent failure of sandwiches can be eliminated. This can be achieved effectively by selecting proper processing method like 3D printing to develop sandwich structure all at once (skin-core-skin).

1.4 Processing of Syntactic foams

All material system has its own set of physical, mechanical, and processing properties. To convert the material into its final shape, a suitable manufacturing process must be selected. The methods to fabricate parts made of composite materials changed from skilled labor operations to advanced microprocessor systems with automatically operated equipment in the twentieth century. Early researchers employed hand lay-up techniques or spray-up in open molds to create the final model by mixing raw materials and curing them at room temperature. PMCs benefits have driven these synthetic materials into nearly every other industry worldwide, from consumer goods to automotive and marine to primary structural components of aircraft and bridges. The rapid expansion of product applications necessitated developing materials technology, design methods, and manufacturing techniques (Arza 2012).

The manufacturing route must be carefully planned to reinforce hollow particles into the resin while fabricating SFs efficiently. By stabilizing gas bubbles in the polymer matrix, it is possible to prevent particle breakage and the inevitable outcome of higher matrix porosity. The manufacturing methods must be capable of wetting homogeneous reinforcement dispersion in the resin material, minimize clusters without influencing the reinforcement, and avoid the hollow particles breakage. Figure 1.6 (Gupta et al. 2013) depicts a typical fabrication process used for reinforced SFs.

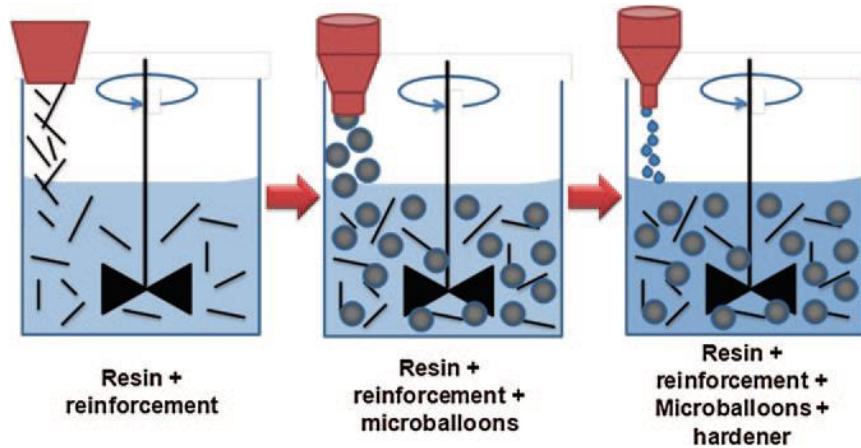


Figure 1.6 Representation of reinforced syntactic foam fabrication method.

A three-step mixing method is employed in this process. The reinforcement is blended into the pure resin in the first stage. Hollow particles are introduced after the reinforcement has been thoroughly mixed and stirred until a slurry of consistent viscosity has been achieved. The hardener or catalyst is applied to the resin in the final stage and stirred slowly. The mixture is poured into molds and cured according to the resin's requirements. Before the inclusion of hollow particles, the reinforcement is thoroughly mixed to reduce the risk of hollow particle breakage during processing. Open mold processes commonly used on the shop floor are hand layup, autoclave, and oven cured. Compression molding, injection molding, transfer molding, and thermo stamping are closed mold processes. The fabrication possibilities for thermoplastic and thermosets are presented in Figure 1.7.

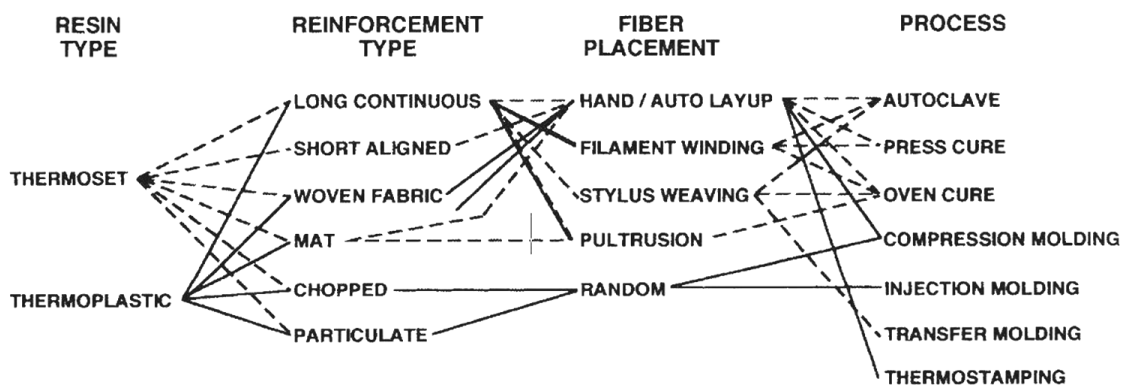


Figure 1.7 Constituents of PMCs and manufacturing options (Reinhart 1998).

Compression and injection molding are most commonly used to manufacture Particulate Reinforced Thermoplastics, as seen in Figure 1.7. Nonetheless, FFF/FDM-based additive manufacturing has taken a giant leap recently to process PMCs.

1.4.1 Compression Molding

Compression molding (CM) is the oldest and unique method used for molding plastic components into parts with near-net shape (Manas and Salil 2006). It is a closed mold technique and consists of two matched metal molds in which one is fixed, and other is moveable. A thermoplastic composite layup is introduced within the mold that is preheated to a specified temperature based on the type of constituent materials. Further, by using a hydraulic system, pressure is applied to the mold to form the required shape. The curing is done in the oven, where the pressure of the mold is maintained constant. A combination of heat and pressure in a compression molding process yield very low void formation and a good surface finish of the final product. CM is suitable for molding complex and high-strength fiber glass reinforcements. It is also feasible for advanced composite thermoplastics with unidirectional tapes, woven fabrics, a randomly oriented fiber sheet, or chopped strands. Compared to injection molding and stamping, compression molding is a more cost-effective option. The mold stays hot right through the compression molding process for thermosets. A fresh charge of molding powder should be added as soon as a molded component is expelled. Thermoplastics, on the other hand, must be cooled to harden, unlike thermosets. Compression-molded HDPE composites are investigated for impact and wear properties (Chand et al. 2010). Mechanical characteristics of compression molded multi-walled carbon nanotubes reinforced HDPE/cenosphere sheets processed at 15 MPa pressure and 160°C are studied (Divya et al. 2015). Deepthi and associates (Deepthi et al. 2014) also studied the mechanical characterization of HDPE reinforced with silicon nitride and nano clay. In terms of cycle time, part complexity, and yield volume, compression molding is less effective than the injection molding process.

1.4.2 Injection Molding

Injection molding is the most widely used manufacturing technique to produce plastic parts. It is also used to create a wide range of different sizes, designs, complexity, and application. An injection molding machine consists of a long screw placed inside a barrel, a hopper from which material in the form of pellets/granules are sent into the barrel, and the heater to melt the material inside the barrel. The material inside the barrel is melted and injected into the mold with the help of a rotating screw, where it cools and solidifies into the final

product. The material is fed into the split mold through a feeding system with sprue gates, and then the part is removed from the mold. Injection molding is one of the most commonly used thermoplastic manufacturing methods. Because of its fast production rate, low material cost, and variety of material choices, it is seen as an excellent alternative method for bulk production of polymer micro/nano engineered surfaces. As compared to compression molded counterparts, injection-molded products have good thermal, acoustic, and mechanical properties. Thermoplastic materials like Low and High-density polyethylene are widely used in the injection molding process (Alkan et al. 1995, Benchekchou et al. 1998). Injection molding facilitates the low-cost production of precision plastic parts in a variety of shapes and geometries. The use of these resins in the production of SFs can allow for weight savings in current applications and the development of new material systems (Bunn and Mottram 1993, Gupta et al. 2004). One of the benefits of using thermoplastic resins for producing SF components is the ability to use rapid production industrial techniques. On the other hand, current research hasn't employed such popular industrial production techniques to make these SFs. The cost of lightweight syntactic foam components can be reduced by using such rapid production techniques (Gupta et al. 2014). Physical and mechanical property study on cenosphere/HDPE based syntactic foams developed using injection molding is carried out by (Kumar et al. 2016). Although this method of using injection molding to produce fly as cenosphere/HDPE SFs is successfully explained, the weight reduction is not achieved, owing to its higher particle failures during processing. Fewer mechanical properties are affected due to higher particle failures inside the matrix resin. The available research on thermoplastic syntactic foams process materials at a laboratory level under controlled conditions typically yields high-quality SFs. On the other hand, material production at the industrial level cannot be able to provide the same quality foams. Though injection molding is a rapid processing method, it is very costly in tooling (molds). An alternative option for this is 3D printing, which provides greater flexibility in manufacturing complex shapes. In the recent past, the number of low-cost additive manufacturing machines available for home use has increased dramatically. This has drawn the focus and interest of the media to additive manufacturing machines. There have been numerous low-cost desktop printers realized recently, and the market sector has inspired a surge of innovation.

1.4.3 Additive Manufacturing (AM)

Advanced manufacturing is driven by rapid growth and developments in the manufacturing field for global competitiveness. Any country's economic growth depends on developing innovative materials and manufacturing technology to create next-generation goods. AM technology has advanced rapidly in recent years and gradually shifting the focus away from traditional application methods by gaining attention to promote competitiveness in the manufacturing sector compared to conventional processing technologies (Mohamed et al. 2015, Rezayat et al. 2015). AM results in a wider range of customization possibilities, increased productivity, flexibility, and cheaper production costs. AM also eliminates conventional part geometry constraints by rapidly manufacturing highly complex components using less material and resources. It eliminates the need for costly tooling and complex drawing, shortening the time from concept to commercialization, and strengthens the renewable energy economy by reducing energy intensity, creating a paradigm shift in the design-to-manufacture process. The traditional reductive techniques like milling or lathing remove material to make a part, whereas AM builds a part by sequentially adding more material. Rapid prototyping is possible in AM, and it can be used directly in manufacturing for small-scale production in some instances. It also enables low-volume output in a fast and cost-effective manner, as well as in adaptive improvements. This could be extremely useful for designers, as a real sense of a physical object can display features that are difficult to interpret from 3D models on a computer screen.

AM's applications are no longer restricted to rapid prototyping due to the brisk development of its methods. Rapid developments in additive manufacturing techniques have taken them from prototyping to the actual development of products in the aerospace, automotive, and medical industries (Vijayavenkataraman et al. 2017), which are now produced and deployed in operation using AM methods. Figure 1.8 shows the process chain of AM/3DP process (Chen et al. 2017). The process chain begins with transforming individual ideas/imagination into a solid CAD model using Computer-Aided Design, Computer Topographic (CT) scanning, or 3D laser scanning techniques, which is then optimized by software to a final shape and size. The CAD model is saved in Stereo lithography (STL)/Standard Tessellation Language format. The STL file is opened in slicing software, which serves as a link between

the 3D printer and the computer. It also permits the set of various process parameters for printing and helps to generate structure geometry and slice the CAD model into thin layers. The machine's operating system executes the G-code generated by the software that specifies the printing path of each layer. Once the printing process begins, the first layer is deposited on the bed/substrate, followed by the next layer deposited on the first layer according to the model definition. The process continues until the entire model is printed. Once the part is entirely printed, it is removed from the bed or substrate, and additional post-processing steps such as priming and painting are performed. Due to differences in method and materials used, various AM processes have different methods for removing the support structure from the actual component. Even though the details of individual AM processes differ significantly, all AM processes have one thing in common: all fabricated parts are created utilizing a quick, precise, fully mechanized and adaptable method directly from a 3D CAD model.

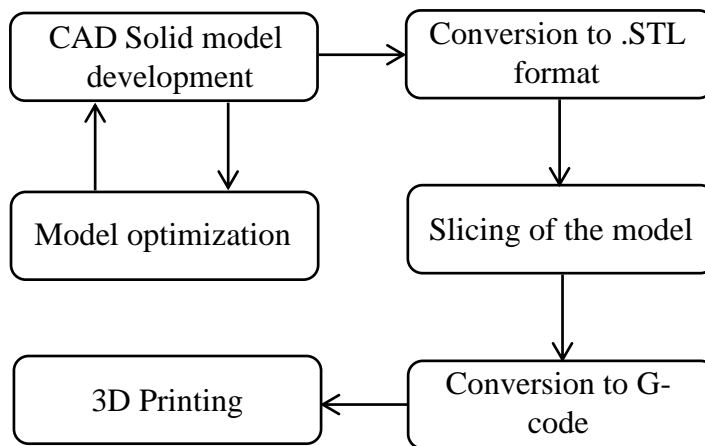


Figure 1.8 Work flow of AM/3DP.

Presently there are many AM systems available in the commercial space. As indicated in Table 1.1, the ASTM F42 council classifies AM processes into seven groups. Four of the seven AM classes are often employed in the processing of polymers, namely, Fused Deposition Modeling (FDM) or Fused Filament Fabrication (FFF), Stereolithography (SLA), Selective Laser Sintering (SLS), and Multi-jet/Polyjet modeling (MJM) (Kazmer 2017). These systems differ in terms of the amount of space needed, cost, layer heights, and materials used. The FFF method is an emerging AM technology in the advanced

manufacturing regime capable of manufacturing products without geometric constraints and offering many benefits such as lower cost, wide use of materials, low environmental damage, easy post-processing, etc. (Griffiths et al. 2016, Rinaldi et al. 2018, Wu et al. 2016). S. Scott Crump invented the FFF technology in the late 1980s, and Stratasys Inc., which he co-founded, commercialized it in 1990 (Perez 2013).

Table 1.1 AM process categories (ASTM F2792-10).

Process Type	Brief Description	Related Technology	Companies	Materials
Binder Jetting	Liquid bonding agent is selectively deposited to join powder material	Powder Bed and Inkjet Head (PBIH), Plaster Based 3D Printing	3D system (USA), ExOne (USA)	Polymer, Foundry sand, Metals
Direct Energy Deposition	Focused thermal energy to fuse material by melting as the material is being deposited	Laser Metal Deposition (LMD)	Optomec (USA), POM (USA)	Metals
Material Extrusion	Material is selectively dispensed through a nozzle or orifice	Fused Filament Fabrication (FFF)/ Fused Deposition Modeling (FDM)	Stratasys (Israel), Bits from bytes	Polymers
Material Jetting	Droplets of build material are selectively deposited	Multi-Jet Modeling (MJM)	Objet (Israel), 3D system (USA)	Polymer, Waxes
Powder Bed Fusion	Thermal energy selectively fuses regions of powder bed	Electron Beam Melting (EBM), Selective Laser Sintering (SLS), Selective Heat Sintering (SHS) and Direct Metal Laser Sintering (DMLS)	EOS (Germany), 3Dsystem (US), Arcam (Sweden)	Metals, Polymers
Sheet Lamination	Sheets of material are bonded to form an object	Laminated Object Manufacturing, Ultrasonic Consolidation (UC)	Fabrisonic (USA), Mcor (Ireland)	Paper, Metals
Vat Photo Polymerization	Liquid photopolymer in a vat is selectively cured by light-activated polymerization	Stereolithography (SLA), Digital Light Processing (DLP)	3D system (USA), Envisiontec (Germany)	Photopolymers

In the recent past, investigations are carried out on fused filament fabricated product characteristics to meet the given design requirements, such as build quality (Caminero et al. 2018, Gordeev et al. 2018, Narahara et al. 2016, Yuan and Bourell 2016), dimensional quality (Boschetto and Bottini 2016, Chen and Zhao 2016, Prüß and Vietor 2015), surface roughness (Boschetto et al. 2016, Durgun and Ertan 2014, Lalehpour and Barari 2018, Turner and Gold 2015), and mechanical properties (Es-Said et al. 2000, Hwang et al. 2015, Torres et al. 2015, Tsouknidas et al. 2016). FFF process (Figure 1.9) is the most common way to produce lower lead times using 3DP processes. Figure 1.9 shows a schematic representation of the FFF method.

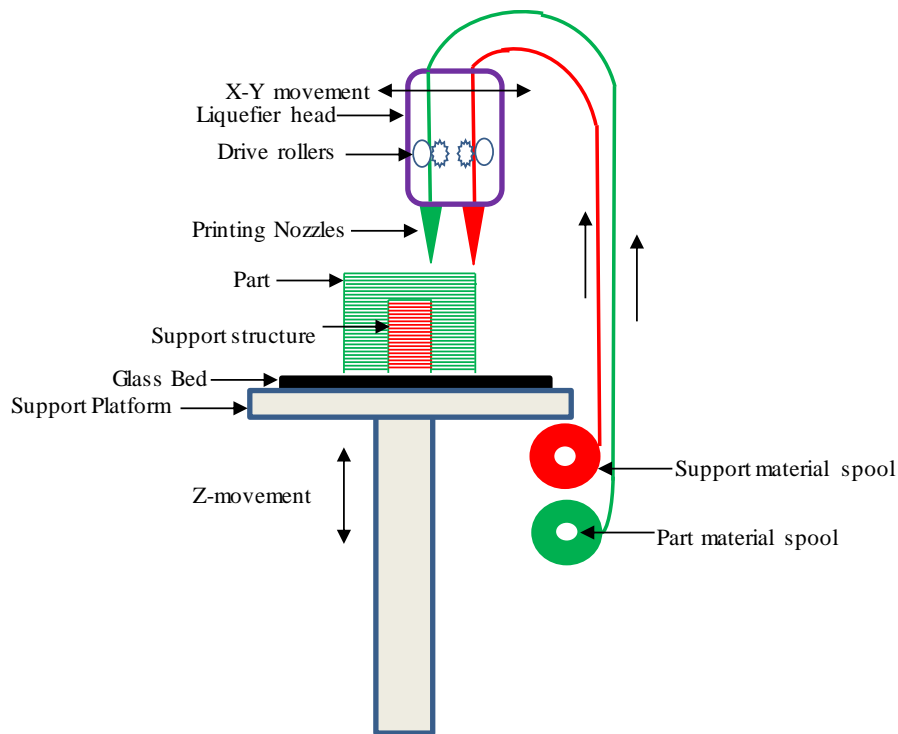


Figure 1.9 Schematic of FFF process.

In the present work, thermoplastic-based syntactic foam core and sandwich composite are 3D printed using FFF technology. The 3DP of composites based on polymer matrix offers higher specific stiffness in weight-sensitive components (Patil et al. 2019). FFF is a layer-by-layer material addition process to produce 3D objects by generating a desired printing path through digital slicing of computed designed virtual 3D objects (Turner and Gold 2015, Turner et al. 2014). Kisslicer, Simplify 3D, and Slice3r are examples of slicing software. Layer thickness, infill %, printing pattern, speed, support structure geometry, and component orientation are

all variables in the process can be defined using this software. The slicing software uses this data to produce G-code, which is then followed by the machine. An electromechanical feeding unit pulls the filament after being unwound from a spool. The heated nozzle would provide enough heat to melt the plastic material. The material in a semi-molten state is deposited on the bed in raster's/roads, and the whole part is printed layer by layer as time passes (Dakshinamurthy and Gupta 2018). In the FFF process, adhesion of the deposited polymer layers, solidification, and easy removal of prints, post-printing are important criteria for obtaining defect-free components. Printing multi-material systems at once, like in sandwiches (skin and core), is challenging because of differential volumetric shrinkage, adhesion, solidification, and crystallization at the skin-core interface. The FFF-based 3DP can be exploited to materialize sandwich manufacturing all at once. 3DP process can be utilized to print sandwiches wherein feedstock filaments of the skin and core can be fed independently one after the other through a 3D printer for layered deposition enabling good bonding between the skin and core.

Developing a lightweight filament with minimum to no particle breakage should significantly enhance specific properties in 3DP of the components for weight-sensitive applications such as in nose cones of remotely operated underwater vehicles or even printing the entire body in the tubular design form with all the internal structural details all at once. Automotive and aerospace components without any joints (integrated components), if realized through 3D printing, can add structural stability with enhanced performance. Adhesive joints are the weakest entities in the structure as pressurization/depressurization leads to foam fracture in a marine environment. 3DP of foams can eliminate adhesive bonding of multiple blocks, making them work well in deep-sea environments. To manufacture complex shapes and contours and eliminate the need for adhesive bonding, foam printing, and the associated development of specialized lightweight filaments is the need of the hour for marine, automotive, and aerospace components.

Due to various material and processing issues, most AM activities are based on polymers and metallic systems as input feed materials, and SF filaments are still in their infancy. There has been minimal research and development on 3D printing of GMB based SF core and sandwich

composites, and no data has been released on the properties of sandwich composites developed all at once (skin-core-skin). For AM of lightweight components utilizing the 3DP technique, novel material compositions with acceptable characteristics and processing parameters must be designed and optimized. This thesis addresses these issues and establishes the route for the use of AM technology to realize SF core and sandwich composites. The proposed methodology in the presented work can directly be implemented or used by the 3D printing industry to develop complex integrated parts without any joints or adhesive bonding. This work has been undertaken to identify the opportunities for decreasing the cost and increasing efficiency through large-scale AM systems. The work aimed to assist POLYMER INDUSTRIES where HDPE components are manufactured using injection molding machines requiring costly tooling. HDPE is reinforced with GMBs resulting in a cost-saving, relatively expensive matrix to develop SF filament to be utilized in the commercially available 3D printers.

The current work successfully demonstrated the development of lightweight feedstock filament intending to widen available material choices for commercially available 3D printers. The syntactic foam core and sandwiches are successfully 3D printed all at once (concurrently) without any defects. Filaments and 3D printed samples are tested for mechanical characterization to check their adaptability and feasibility for 3DP in weight-sensitive applications.

1.5 Review of Literature

Syntactic foams are lightweight composites and are used prominently in weight-saving applications. However, the extent to which these can be modified to achieve a desired mechanical performance is highly dependent on the resulting effective properties and, more significantly, the connection between these properties and their structure/microstructure. In the design and development of SF composites, investigating mechanical, thermal, and other related properties for a given microstructure and spatial distribution is essential. The table below presents, review dealing with the mechanical response of SFs and their associated processing routes.

Table 1.2 Thermoplastics for FFF.

Author	Process	Parameters	Materials Used	Property Studied	Remarks
(Nikzad et al. 2011)	FDM (3000)	Composition, Filler percentage	ABS (P400) - Iron Filler, ABS (P400) - Copper filler	Thermal conductivity, Heat capacity, DMA, Tensile	<ul style="list-style-type: none"> • The conductivity of a copper-ABS composite [30 vol. % Cu (45m)] is significantly increased. • ABS composites heat capacity is reduced when Fe is added. The conductivity of the Fe-ABS composite [30 vol. % Fe (45m)] increased dramatically. • A 3.5-4 GPa increase in storage modulus of composite [30 vol.% Cu (10 m)] is observed, which substantially reduced post further additions. • Storage modulus of composite [30 vol. % Fe (45m)] increased by 2.5-3 GPa, but values dropped dramatically post additions. • In ABS composite, storage modulus

					dropped significantly after 10 vol.% Cu (45m). As compared to neat ABS, the tensile strength of iron-ABS (10 vol.% Fe) composites dropped significantly.
(Singh et al. 2016)	FDM (uPrint SE)	MFI, Filler matrix proportion	Matrix: Nylon-6, Filler: Al ₂ O ₃	MFI, Wear	<ul style="list-style-type: none"> The composite's MFI decreased as the Al₂O₃ content increased. MFI has created an alternative filament based on standard filament with a suitable filler-matrix proportion (50:50 by wt. %). Wear resistance increased significantly as a result of the filler reinforcement.
(Singh et al. 2017)	Extrusion	Barrel and Die temperature, Screw speed, Wt. % of Fe.	HDPE, HDPE + Fe, LDPE, LDPE + Fe	Peak elongation, break strength, porosity	<ul style="list-style-type: none"> In the case of reinforced HDPE, peak elongation of 3.63 mm and break intensity of 15.02 N/mm² are observed. For 100 % HDPE, the porosity developed is the lowest.

(Dakshinamurthy and Gupta 2018)	FDM	Raster width, Raster angle, and Slice height	ABS	Viscoelastic property	<ul style="list-style-type: none"> • Slice height and raster distance both contributed 55 and 31 % to the viscoelastic properties of the FFF-RP components, respectively.
(Geng et al. 2019)	FDM	Printing speed and temperature	Polyether-ether-ketone (PEEK)	Extrusion and printing speed effect	<ul style="list-style-type: none"> • Higher melt pressure lowers surface defects • A fluctuating extrusion force is a major constraint on the extrusion process' stability.
(Lee and Huang 2013)	FDM	Print orientation	ABS, ABS +	Tensile	<ul style="list-style-type: none"> • Printed ABS's ultimate stress ranges from 50-80% of the ABS wire. The ABS plus printed sample's ultimate stress is 75-80% of the ABS + wire results. • The strain energy of ABS and ABS + printed samples ranges from 3.4 - 19.7% and 1.8 - 7.4% compared to neat ABS material respectively.
(Rayegani and Onwubolu)	FDM (Fortus)	Raster width angle, Part	ABS	Tensile properties	<ul style="list-style-type: none"> • Strength is affected by variations in component orientation and raster

2014)	400mc)	orientation and Air gap			angle. Tensile strength increases with a negative air gap and a smaller raster width.
(Tekinalp et al. 2014)	FDM	Method (CM, FDM), Carbon fiber wt. %	ABS, Carbon fiber (short fiber)	Tensile, Comparison with CM specimen	<ul style="list-style-type: none"> • As compared to neat ABS, the tensile strength and modulus of FDM composite are 115 % and 700 % higher, respectively. • In comparison to the CM sample, printed samples have a higher porosity. • The tensile modulus and strength of the FDM and CM samples are similar.
(Tuan Rahim et al. 2015)	3DP (Maker Bot Replicator 2X)	Material (neat, composite)	Fillers: Polyamide (PA1) + 5% hydroxyapatite (HA) + 15% ZrO ₂ , ABS with Cu and	Tensile, MFI, Thermal analysis	<ul style="list-style-type: none"> • PA12/ZrO₂/HA has a tensile strength of 22.78 MPa, which is lower than unfilled PA12 (26.54 MPa) and approximately equivalent to commercial PA and Taulman 618. (21.49 MPa). • With the addition of 15% ZrO₂ and

			Fe, pure polyamide 12, commercial polyamide, Taulman 618		<p>5% HA, the MFI of PA12 is reduced from 13.5 to 2.7 g/10 min.</p> <ul style="list-style-type: none"> The presence of filler raised the crystallisation temperature by ~ 4 °C and decreased the melting temperature by ~ 1 °C.
(Hwang et al. 2015)	FDM	Proportion of Cu and Fe particles, Temperature, Fill density	ABS with Cu and Fe particles	Tensile, Thermal conductivity	<ul style="list-style-type: none"> Tensile stress is reduced by adding Cu and Fe respectively from 45.7 - 26.5 and 45.7 - 36.2 MPa. The addition of 50 wt.% Cu particle to ABS reduced CTE by 29.50 % and increased conductivity from 0.646 to 0.912 W/Mk. The addition of metal powder to neat ABS reduced component distortion.
(Singh et al. 2016)	FDM	Particle size in equal proportion in weight (DPS, TPS, SPS)	Nylon 6 matrix of Al ₂ O ₃ and SiC-Al ₂ O ₃ particles	Tensile, MFI, Wear studies.	<ul style="list-style-type: none"> With increasing particle concentration, tensile and yield strength, percentage elongation and Young's modulus decrease.

					<ul style="list-style-type: none"> • MFI decreases as particle concentrations increase. As the particle concentrations increase, the wear rate decreases.
(Singh et al. 2016)	FDM	Temperature of the barrel, screw and take up speed	ABS-EG (Extrusion Grade)	Tensile	<ul style="list-style-type: none"> • Tensile strength is improved by increasing the barrel temperature and screw speed. • Strength and modulus are unaffected by take up speed. Young's modulus decreases as barrel temperature increases, As the screw speed increases up to 35 rpm, modulus is observed to increase. • One cartridge cost of 16.27 USD to fabricate, saves about 93 % of FDM filament.
(Faes et al. 2016)	FDM (Dimension SST 1200es)	Inter layer-cooling time, Build orientation	ABS –m30	Tensile strength	<ul style="list-style-type: none"> • As the interlayer cooling time is increased from 3.59 to 45.27 seconds, the upright sample strength drops from 20.5 to 13.3 MPa and

					<p>the elongation drops from 1.24 to 0.86 %.</p> <ul style="list-style-type: none"> • As the interlayer cooling time ranges from 54.92 to 282.71 s, the flat sample strength remains constant at 19 MPa. • As the interlayer cooling time is increased from 3.59 to 45.27 seconds, the flat sample elongation and modulus remain constant.
(Dul et al. 2016)	FFF (Sharebot NG, Italy)	Build orientation, Processing condition, Composition	ABS and Graphene nanoplatelets (xGnP)	Tensile, MFI, DMA, CTE	<ul style="list-style-type: none"> • Introducing 4 wt.% xGnP into ABS resulted in a 30 % increase in modulus over neat ABS for all manufacturing conditions (CM, 3DP, extrusion), as well as a reduction in stress and strain at break. • With the addition of xGnP, the MFI of neat ABS decreases. • The addition of 4 wt. % xGnP

					increased storage modulus and decreased CTE.
(Singh et al. 2016)	FDM (uPrint SE system)	Wt.% of Nylon-6 and Al ₂ O ₃ , Size of Al ₂ O ₃ , SPS, TPS and DPS	Filament of Al ₂ O ₃ reinforced with Nylon-6	Tensile properties	<ul style="list-style-type: none"> As the particle size varies in proportion from SPS (100 m) to TPS (100, 120, and 150 m), the % elongation decreases. DPS (100 and 120 m) have comparable maximum tensile strength, while TPS has the minimum value. DPS has the maximum Young's modulus and yield strength.
(Zou et al. 2016)	FDM (Dimension SST 1200es)	Build angle	ABS plus	Tensile	<ul style="list-style-type: none"> Using an isotropic model, the modulus, Poisson's ratio, and yielding stress are found to be 2400, 0.37, and 26.84 MPa, respectively. Poisson's ratio: 0.24 and 0.34, Young's modulus: 2432.29 MPa and 2367.10 MPa, and shear modulus 830.47 MPa are the results

					of transversely isotropic model in transvers and principal axis.
(Riddick et al. 2016)	FDM (Fortus 400 mc)	Build Direction, Orientation	ABS	Tensile	<ul style="list-style-type: none"> • Horizontal build direction: max. strength 32.60 MPa and modulus 2.69 GPa, raster angle 0°; min. strength 15.26 MPa, raster 90°) • Vertical build direction: max. strength 19.80 MPa, raster angle 45°; minimum strength 12.42 MPa, raster angle 90°, maximum modulus 2.7 GPa and 0° raster angle.
(Ferreira et al. 2017)	FDM	Printing orientation (0°, 90°, ±45°)	PLA/short carbon fiber	Tensile modulus, shear modulus, Poisson's ratio, and related strengths	<ul style="list-style-type: none"> • Tensile modulus of 2.2 and 1.25 times that of neat PLA at 0° and 90° orientations, respectively. At 45°, the shear modulus is 1.16 times that of neat PLA. • In both orientations ±45°, the Poisson coefficient is the same for neat PLA. The PLA and PLA/CF strengths are almost identical.

(Ning et al. 2017)	FDM	Nozzle temperature, Layer height, Raster angle and Infill speed	CFRP (ABS+ 5 wt. % Carbon fiber)	Tensile	<ul style="list-style-type: none"> • Tensile, yield strength and Young's modulus are higher at 0 and 90° than at ±45°. The highest average tensile properties are found in parts printed at a speed of 25 mm/s. • With a nozzle temperature inflection point of 220°C, the tensile properties increased and then decreased. • For a layer height of 0.15 mm, the tensile, yield strength and modulus are maximum. • For a layer height of at 0.25 mm, toughness and ductility reached their maximum mean values.
(Alaimo et al. 2017)	FDM (3NTR A4v3)	Filament cross-section, material (ABS and chemically additivated)	ABS	Tensile, Shear strength	<ul style="list-style-type: none"> • With filament cross-section (0° and 90°), there is an increase in elastic modulus. With increasing filament cross-section, tensile strength and ultimate strain increased at 90° and

		ABS)			<p>decreased at 0°.</p> <ul style="list-style-type: none"> • Shear modulus decreases as cross-section increases, while intensity increases at 90° and decreases at 0° as cross-section increases. • In comparison to neat ABS, ductile failure mode is observed in chemically additive ABS.
(Porter et al. 2017)	FFF	Infill angle, Number of outside perimeters, Sample thickness, Nozzle temperature	Polyvinylidene fluoride (PVDF)	Young's Modulus, Yield strength, β -phase	<ul style="list-style-type: none"> • 0° (484 MPa) and 90° (419 MPa) have the highest and lowest Young's modulus, respectively. While the infill pattern is parallel to the loading axis, yield strength is highest, and as the infill angle is decreased, yield strength decreases. • The Poisson's ratio is highest for 45° (0.361) and lowest for 0° degrees (0.243). • At high β-phase material the printed PVDF films display a small but

					<p>clear piezoelectric response when subjected to a post-printing corona poling procedure.</p> <ul style="list-style-type: none"> • Higher β-phase is characterized by high voltages, faster extrusion rates and lower extrusion temperatures.
(Yao et al. 2019)	FDM	Layer height (0.1,0.2 and 0.3 mm) and Printing angle (0,15,30,45,60,75 and 90°)	PLA	UTS	<ul style="list-style-type: none"> • The printing angle has a huge impact on UTS. Theoretical and experimental findings also showed that as layer height increases (0.1 - 0.3 mm). • The UTS of FDM 3D printed materials with different printing orientations can be predicted using two types of shear formulas obtained by theoretical models.
(Patil et al. 2019)	FDM	Orientation of infill ($\pm 45^\circ$)	HDPE and Cenospheres	Density, Rheology, Tensile and flexural	<ul style="list-style-type: none"> • Samples are printed with $\pm 45^\circ$ infill angle. Tensile and Flexural modulus increased with increase in the infill %.

				properties	<ul style="list-style-type: none"> • Tensile and flexural strength decreases with increase in the infill percentage.
(Domingo-Espin et al. 2015)	FDM (fortus 400mc)	Build orientation	Polycarbonate	Flexural, Tensile	<ul style="list-style-type: none"> • The highest (1.43) and lowest (1.33) flexural stiffness coefficients are found in the X and Y orientations, respectively. • Samples printed in the X (45.9 MPa) and Z (45.6 MPa) orientations had equal tensile strengths, while samples printed in the Z +45 (36.0 MPa) orientation had the lowest tensile strength. Samples printed in the Y (54.6 MPa) orientation had the highest tensile strength. • The highest and lowest Young's modulus is found in samples printed in the Y (2.41 GPa) and X (2.10 GPa) orientations, respectively.

(Weng et al. 2016)	FDM (creator, flash forge, china)	Organic Modified Montmorillonite (OMMT) wt. %	ABS and Organic Modified Montmorillonite (OMMT)	Flexural, Tensile, DMA, Thermal expansion	<ul style="list-style-type: none"> • The flexural strength of the material increased from 42.69 to 56.92 MPa (5 wt. % OMMT). • The addition of 5% OMMT to ABS samples increased the tensile modulus and strength of 3D printed (43%) and IM (28.96%, 68.42%) ABS samples, respectively. • The neat ABS storage modulus increased from 1.1 to 1.6 GPa (5 wt. % OMMT). Thermal stability increased and the thermal expansion coefficient decreased after the addition of OMMT.
(Abdullah et al. 2017)	FDM	Filler wt. %	Polyamide 12 (PA 12) and ceramic filler (30, 35 and 40 wt. %)	Flexural, Tensile and surface roughness	<ul style="list-style-type: none"> • In comparison to composites, PA 100 had the highest flexural modulus (1083.14 MPa). PA 12 (PA100) has higher tensile (33.98 MPa) and flexural (47.53 MPa) strength than composites (PA70F30,

					<p>PA65F35, PA60F40).</p> <ul style="list-style-type: none"> • PA 100 has a tensile modulus of 905.94 MPa, which is higher than PA70F30's (873.44 MPa), but lower than PA65F35's and PA60F40's. • The total surface roughness of the composites is 6 μm.
(Tian et al. 2017)	FDM	Material states (Pure, originally printed and Re-manufactured)	Poly lactide + Carbon Fibers	Flexural, Tensile, Charpy Impact	<ul style="list-style-type: none"> • Pure PLA sample flexural modulus and strength are 4.5 GPa and 100 MPa. CFRTPCs originally printed flexural modulus and strength are 14.5 GPa and 225 MPa, and re-manufactured flexural modulus and strength are 13.3 GPa and 263 MPa. • The pure PLA sample had a tensile modulus and strength of 4.2 GPa and 62 MPa, while the CFRTPCs are initially printed and re-manufactured had approximately equal strength (~256 MPa) and

					<p>modulus (~20.6 GPa).</p> <ul style="list-style-type: none"> • Pure PLA, CFRTPCs, and re-manufactured have impact strengths of 20, 34.5, and 38.7 kJ/m², respectively.
(Yao et al. 2017)	FDM	Fill density (%), Carbon fiber (no of filaments)	PLA + Polyacrylonitrile (PAN) based continuous carbon fiber	Three Point Bending and Tensile	<ul style="list-style-type: none"> • Fiber reinforcement increased flexural and tensile strength by 18.7 and 70%, respectively. • Weight saving of 26.01 % and 11.41 % of print time reduction.
(Li and Wang 2017)	FDM	Polymer reinforced with woven and unidirectional carbon fiber	Vero-White and acrylic-based photopolymer (core), unidirectional and woven carbon fibre (skin)	Flexural	<ul style="list-style-type: none"> • Flexural strength and stiffness are maximum for sandwich composites having truss core. • Re-entrant honeycomb core display simultaneous snap-through instability, which improves damping significantly.
(Nugroho et al. 2018)	FDM	layer thickness (0.1, 0.2, 0.3,	PLA	Flexural	<ul style="list-style-type: none"> • In the case of upright orientation, the results showed that increase in

		0.4, 0.5) mm			<p>the layer height, increases the flexural strengths.</p> <ul style="list-style-type: none"> • By retaining the bending load, the higher sheet's thickness continued to sustain greater pressure.
(Seyedkanani et al. 2020)	FDM	Beam thickness and length	Graded cellular beams	Flexural	<ul style="list-style-type: none"> • A substantial enhancement in bending stiffness is noted for a cellular beam graded across length, thickness, and in both directions, with values as high as 43, 155, and 182 %.
(Zeng et al. 2021)	FDM	Core wall and panel thickness, horizontal core wall length, single-layer corrugated core height, and corrugation angle	Trapezoidal corrugated sandwich structures made of continuous fiber-reinforced composite (CFRCTCSs)	Bending behavior and failure analysis	<ul style="list-style-type: none"> • The greater the number of layers, the higher the peak failure load of the CFRCTCS, lower specific flexural module and bending strength of the CFRCTCS. • As compared to the bending properties of many other existing structures, the 3D printed CFRCTCSs have the potential to

					provide new options for lightweight systems and multifunctional applications.
(Wang et al. 2016)	FDM	Heating time, Heating temperature, Microsphere percentage	Filament of poly wax mixed with hydrocarbon filled microspheres (Expancel 930DU120)	Compressive, Tensile	<ul style="list-style-type: none"> • 2 wt. % filled samples are heated at 140° C for 120 seconds. • Compressive and tensile strength increased by 52.2 % and 25.4 %, respectively, when compared to untreated samples.
(Byberg et al. 2018)	FDM	Build path (flat, edge and upright) and layer orientation (0°, 90°, 45°)	ULTEM 9085	Compression, Tensile and Flexural	<ul style="list-style-type: none"> • Maximum compressive stress is reported with a flat build direction and 90°-layer orientation. • Higher tensile stress was reported at edge build direction and 0°-layer orientation. • The combination of flat build direction and a 0° layer orientation yielded the highest flexural stress.

(Patil et al. 2019)	FDM	Quasi-static strain rates	Cenosphere/ HDPE syntactic foam	Compression	<ul style="list-style-type: none"> • Compression and specific modulus are found to increase with cenospheres vol. % and strain rate. • As the strain rate increases, the specific compressive strength increases, and it decreases as the cenospheres volume % increases. • The strain rate sensitivity of 3D printed syntactic foams is higher.
(Haldar et al. 2021)	3DP	Core designs - triangular and trapezoidal cores	Carbon fiber reinforced poly-lactic acid (CFRP)	Compression	<ul style="list-style-type: none"> • With increase in core thickness the compressive strength and energy-absorbing ability of the sandwich panels increase rapidly. • Mechanical properties are improved by increasing the contact area between the core and skins.
(Wang et al. 2018)	3DP	viscoelastic material filling	Sandwich panels of	Vibration damping and	<ul style="list-style-type: none"> • The VMF approach is efficient in lowering amplitude without

		(VMF)	hybrid composite Kagome truss with viscoelastic material filling	Eigen frequency	<p>substantially raising natural frequency, as per the findings of dynamic analysis.</p> <ul style="list-style-type: none"> • The acceleration amplitude of the VMF Kagome lattice plate at natural frequency is decreased by 18.19 dB when compared to a solid plate in a fixed modal test, and by 6.03 dB when compared to a regular Kagome lattice plate in a fixed modal test. • The VMF method can be used to create band-gaps. In both free and restricted modal study, the VMF method is observed to be capable of acquiring a band gap at a low frequency. • The reasons for the frequency band gap, as well as how designers can achieve the band gap at the optimal
--	--	-------	--	-----------------	--

					frequency by choosing the right viscoelastic material and lattice structure, are unclear.
(Amirpour et al. 2019)	3DP	Material stiffness ratios	Rigid plastic and rubber	A numerical and experimental analysis of 3D-printed polymeric functionally graded plates	<ul style="list-style-type: none"> • The variation between FE and experimental out of plane deflection for nonlinear FG plates is observed to be greater than for linear FG plates, which may be due to the high gradient distribution of the material additions. • The proposed 3D-digital image correlation method enables for transverse deformation of polymeric FG plates. • The FG plate's deflection contours are asymmetric, with the linear high stiffness ratio combination creating more significant variations. • The results of this study can be used to determine the best material

					selection for creating a polymeric FG plate with optimized stiffness and specified structural properties.
--	--	--	--	--	---

From Table 1.2, the majority of thermoplastic additive manufacturing efforts are based on printing only a few polymers/composites, limiting their applications in weight-sensitive structures and buoyancy modules. Prevailing literature indicates, hollow glass microballoons have not been well utilized in the production of thermoplastic-based syntactic foam core and sandwich composites using 3D printing. Interest in utilizing the benefits of the low-density syntactic foams and their sandwiches in a number of applications has necessitated characterization of these materials. As a result, the current research focuses on the manufacturing and characterization of lightweight GMB/HDPE syntactic foam filaments, as well as printing feasibility of SF core and concurrent printing of sandwich using commercially available 3D printers.

1.6 Motivation of work

Composite printing is an emerging technology to vastly improve the realization of seamlessly integrated components with a substantial reduction in production lead-time. Due to its flexibility in design, 3D printing draws the attention of researchers to explore new avenues for composite developments. Syntactic foams are one of those materials known to have lower density and higher damage-tolerant morphology. GMB based SFs are widely used in developing lightweight thermoplastic syntactic foams for weight-sensitive structures. Compared to fly ash cenospheres based closed cell foams, GMBs exhibit better mechanical properties due to the defect-free surface morphology and higher sphericity. Introducing hollow GMB particulate fillers in a matrix can significantly reduce weight and can be effectively exploited for weight-sensitive structures. The sandwich composites manufactured through the conventional approaches against 3D printed ones have the weakest point across the skin-core interface and limitations of fabricating geometrically complex designed cores. 3DP enabled complex and variable microarchitectures to manufacture lightweight sandwich structures (concurrent) with good interfacial bonding between skin and core. The present work focuses on developing lightweight GMB/HDPE syntactic foam filaments and concurrent 3DP of syntactic foam core and sandwich composite for mechanical characterization. The Motivation for pursuing this topic is summarized as below.

- Reduction in consumption of polymers
- Eco-friendly processing
- Durable, integrated components with complex geometries

The objectives of the work are outlined in the next section.

1.7 Objectives and scope of the work

The literature on the development of GMB/HDPE based syntactic foam filament, and 3DP of syntactic foam cored sandwich composites is scarce, as seen by the preceding literature review. As a result, the current study proposes the development and suitability of GMB/HDPE based syntactic foam feedstock filaments and its potential in 3D printing of concurrent sandwich composite.

The work undertaken aims to achieve the following objectives.

- Development of syntactic foam composite feedstock filament.
- Development of GMB/HDPE core and concurrent printing of sandwich composites through suitable printing parameters.
- Study the effect of GMB content on physical (Density and void content), flow, thermal, rheological properties (MFI, CTE, DSC), and mechanical properties of Core (Tensile, Three-point bending, Compression, Buckling and Vibration) and concurrently printed sandwich composite (Three-point bending, Compression and Buckling and Vibration).
- Development of representative industrial scale components to show the feasibility of 3D printing for GMB/HDPE based SFs.

The studies on thermoplastic SFs that are currently available process materials under controlled conditions at a laboratory scale, resulting in high-quality foams. Nonetheless, SFs have been manufactured by injection, and compression molding requires costly tooling. However, due to the challenges in developing high quality filaments without any particle breakage during blending and filament extrusion, studies on AM of SFs are not yet available. Rapid manufacturing with zero lead times is essential for meeting the ever-increasing demands for complex and long-lasting products. As a result, this work focuses on utilizing one such method known as 3D printing for realizing SFs and their sandwich composites.

The scope of this research includes preparation of blend by reinforcing hollow glass microballoons as fillers (20, 40, and 60 volume %) in HDPE matrix. Blends are characterized for MFI and rheological properties. Extrusion variables are chosen suitably to get the required feedstock filament diameter, which can then be loaded into a commercial 3D printer with ease. DSC, CTE, and tensile experiments are conducted to investigate filler-matrix behavior through mechanical and thermal tests. Finally, the potential of 3DP is demonstrated by printing SF industrial scale components.

1.8 Thesis Outline

The systematic study carried out for the above objectives is presented in the thesis. A brief skeletal structure of the thesis is,

Chapter 1. Provides an exhaustive literature survey on the FFF method followed by the objective and scope of the work.

Chapter 2. Deals with SF composites and associated processing and testing.

Chapter 3. Covers characterization methods and aspects of processing.

Chapter 4. Tensile behavior of filament and 3D prints is dealt with in this chapter.

Chapter 5. In this chapter, the flexural response of 3D printed core and concurrently printed sandwich composites are reported.

Chapter 6. Deals with compressive behavior of 3D printed core and concurrently printed sandwich composites.

Chapter 7. Buckling and free vibration of 3D printed core and concurrently printed sandwiches are dealt with in this chapter.

Chapter 8. This chapter demonstrates 3D printed industrial components.

Highlights of the significant conclusions drawn from the results are finally presented.

2 MATERIALS AND METHODS

2.1 Constituent Materials

In the present work, hollow glass microballoons (GMBs) are used as fillers, and high-density polyethylene (HDPE) is used as a matrix to prepare lightweight thermoplastic syntactic foam composites. Details about these constituents are dealt with in the sections to follow.

2.1.1 Glass microballoons

Hollow glass microballoons of grade iM30K are procured from 3M Corporation, Singapore. GMBs are used in as-received conditions (Figure 2.1a), without any surface treatment. Table 2.1 properties of GMBs in as-received condition.

Table 2.1 Properties of iM30K hollow glass microballoons*.

Particulars	Typical Value	Unit	Test Method
Shape	Hollow spheres with thin walls		
Composition	Soda-lime-borosilicate glass		
Appearance	Off-white, powdery		
True Density	0.60	(g/cc)	3M QCM 14.24.1
Isostatic Crush Strength	27,000	(psi)	3M QCM 14.1.8
Packing Factor (bulk density to true particle density)	63	%	-----
Oil Absorption	33.5	g oil/100 cc	ASTM D282 - 84
Softening Point	600	°C	-----
Flotation (density < 1.0 g/cc)	90	% (in volume)	3M QCM 37.2
Volatile Content (by weight)	Max. 0.5	%	3M QCM 1.5.7
Alkalinity	< 0.5	Milliequivalents/ gram	3M QCM
pH (5% loading in water)	9.5	-----	ASTM D3100 -1982
Diameter (average)	18	microns	3M QCM 193.0
Softening temperature	600	°C	-----
Thermal conductivity	0.05 - 0.20	Wm ⁻¹ K ⁻¹	@20°C
Dielectric constant	1.2 - 1.9	-----	@100 MHz
Minimum fractional survival	90	%	-----

*Supplier data

2.1.2 Matrix

HDPE of grade HD50MA180 supplied by Indian Oil Corporation Limited, Mumbai, India, is used as the matrix material. The resin is in granular form (~3 mm diameter). Table 2.2 presents the details about the matrix used. HDPE (Figure 2.1b) is also used in as-received condition.

Table 2.2 Characteristics of HDPE grade HD50MA180*.

Property	Test Method	Typical Value	Unit
Melt Flow Index (190 ⁰ C/2.16 kg)	ASTM D 1238	20.0	gm/10 min
Density @ 23 ⁰ C	ASTM D 1505	0.950	gm/cm ³
Tensile Strength at Yield	ASTM D 638	22	MPa
Elongation at Yield	ASTM D 638	12	%
Flexural Modulus	ASTM D 790	750	MPa
Hardness	ASTM D 2240	55	Shore D
Vicat Softening Point	ASTM D 1525	124	°C

* Supplier data



Figure 2.1 As received (a) GMB in powder form and (b) HDPE granules used in the present work.

2.2 Blend preparation

A Brabender of type 16CME SPL supplied from western company Keltron CMEI, Germany, is used to blend HDPE and GMB. Blending speed and temperature are set at 10 rpm and 160 °C (Jayavardhan and Doddamani 2018, Jayavardhan et al. 2017), respectively, based on the pilot experiments to avoid the GMB breakage. The GMB and HDPE are plasticized in a Brabender, as shown in Figure 2.2a. Mixing takes place in a confined chamber comprising of two screws, as seen in Figure 2.2b. Material is fed through a feeder, which melts in the heating zone and later is carried

forward to twin screws/lobes (Figure 2.2b). The blend of GMB/HDPE from Brabender in the form of pellets is depicted in Figure 2.2c. The blend compositions are represented as H20, H40, and H60, where H denotes the HDPE matrix and 20, 40, and 60 indicates volume % of GMB present in the HDPE matrix. The GMB volume % is chosen in the range of 20 - 60, as below 20%, no appreciable change in mechanical properties is seen. In comparison, above 60% volume fraction, much viscous blend formation is experienced with substantially higher particle breakage owing to particle-particle interactions (Jayavardhan et al. 2017). Figure 2.3 presents a flow chart of the envisaged work as part of this work.

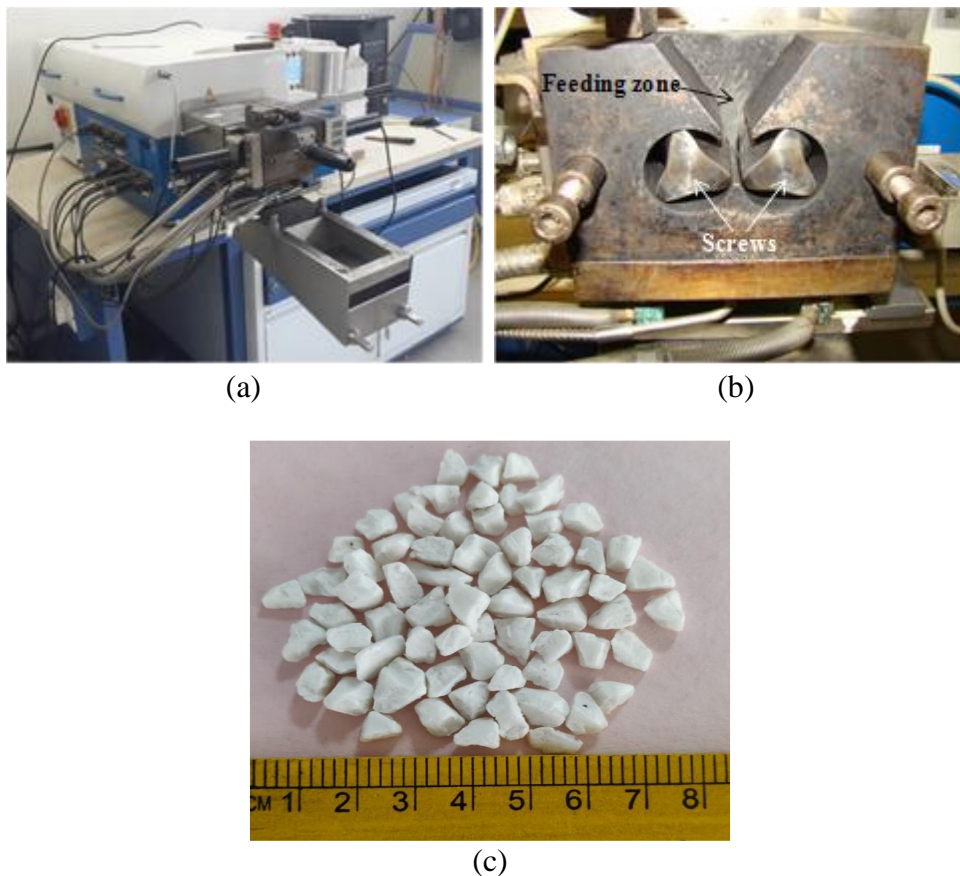


Figure 2.2 (a) Brabender (b) blending mechanism and (c) GMB/HDPE blend from brabender.

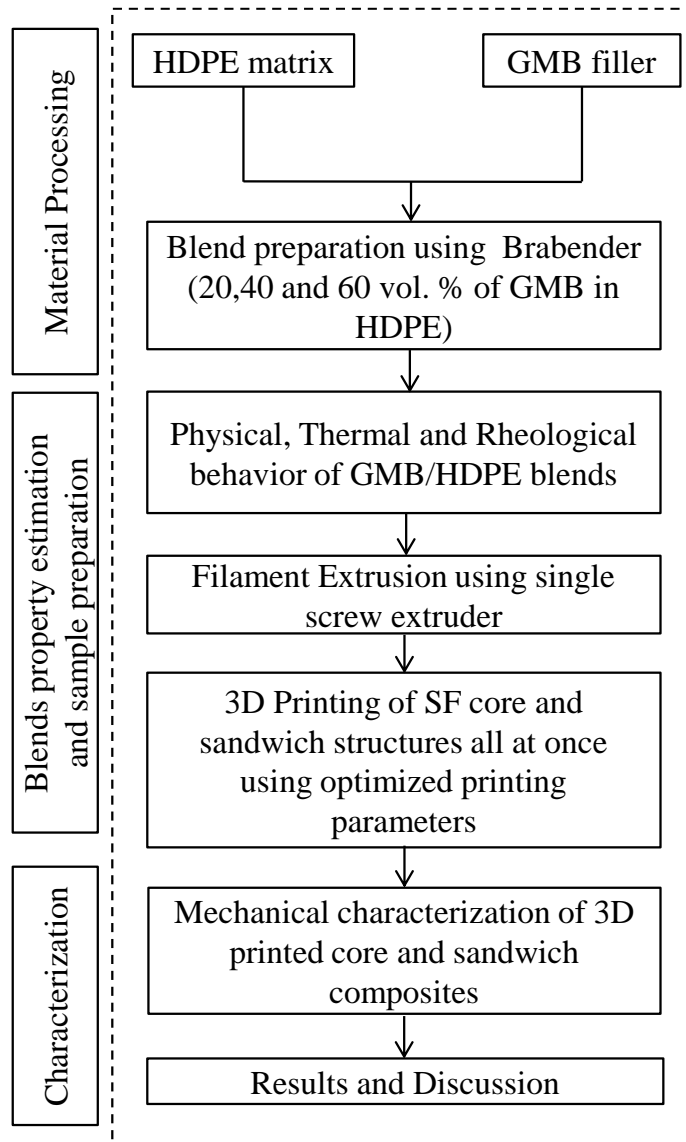


Figure 2.3 Flow chart of the present study.

2.3 Melt Flow Index (MFI)

MFI estimates material flowability. Melt flow rate refers to the rate at which thermoplastics are extruded through an orifice at a specified temperature and load. Dynisco LMI5000 MFI equipment (Figure 2.4) is used to measure MFI (ASTM D1238) of H - H60 pellets, which helps set an appropriate multiplier in 3D printing by isolating different temperature settings for different compositions.

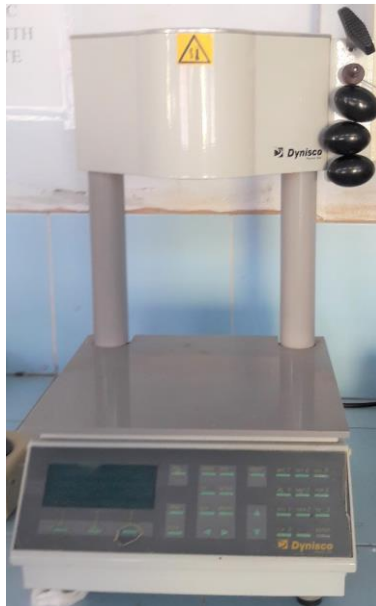


Figure 2.4 Melt flow indexer (Dynisco LMI5000).

2.4 Rheological study of GMB/HDPE blends

The study of rheological properties is essential to know the effect of the filler on manufacturing conditions. An Anton Paar rotational rheometer, MCR 502, is used to investigate the influence of fillers on the rheology of the developed blends. A 25 mm diameter and 1 mm thick specimens are used for frequency and temperature sweep. The frequency sweep is conducted at 0.1 - 10 Hz, 150 °C and 5% loading rate. The effect of frequency and GMB content on complex viscosity (η^*), storage (G'), and loss modulus (G'') is investigated. Similarly, in the temperature range of 130 - 150 °C, a temperature sweep is performed at 1 Hz. An average of five replicates is considered for all the experiments.

2.5 Filament development and 3D Printing

The most popular process for shaping polymer is extrusion. It is an uninterrupted process that employs a screw/barrel operation to drive polymer melt through a die to make products including films, pipes, plates, tubes, profiles etc. It can be used for compounding or palletizing polymerization. An extruder comprises an Archimedean screw that rotates inside a heated barrel, eventually melting polymeric granules or powder and delivering it to a die for shaping. The polymer is melted by a combination

of electrical heaters along the length of the barrel and frictional heat produced by the melt being sheared by the screw rotation. Solids conveying or feeding, melting or transition, and metering or pumping are the three-primary functional/geometrical zones of an extruder screw.

In order to develop a good quality GMB/HDPE syntactic foam filament, the issues related to particle breakage, formation of voids, and improper mixing must be carefully considered. For clarification, a schematic representation and a photograph of a single screw extruder that is used to develop HDPE and foam filament are presented in Figure 2.5a and Figure 2.5b, respectively. The single screw extruder's specifications are listed in Table 2.3 for reference.

For clarity, a schematic illustration and photograph of an industrial-scale FFF 3D printer depicted in Figure 2.6a and Figure 2.6b, respectively. The printer has dual brass nozzles and an overhead gantry with an extrusion/printing head that includes a melting unit and two nozzles, one for part material and the other for support material. The heating block above the nozzle provides the heat needed for filament melting. Appropriate built-in heating elements can maintain the temperature of the enclosed printing chamber. A fixed glass bed with embedded heating components is used in the chamber. The loading spools of part and support material are facilitated through a hanger arrangement. The machine control unit uses individual stepper motors to monitor the movement of the printing head in the X, Y, and Z directions. The technical characteristics of the 3D printer utilized in this study are listed in Table 2.4.

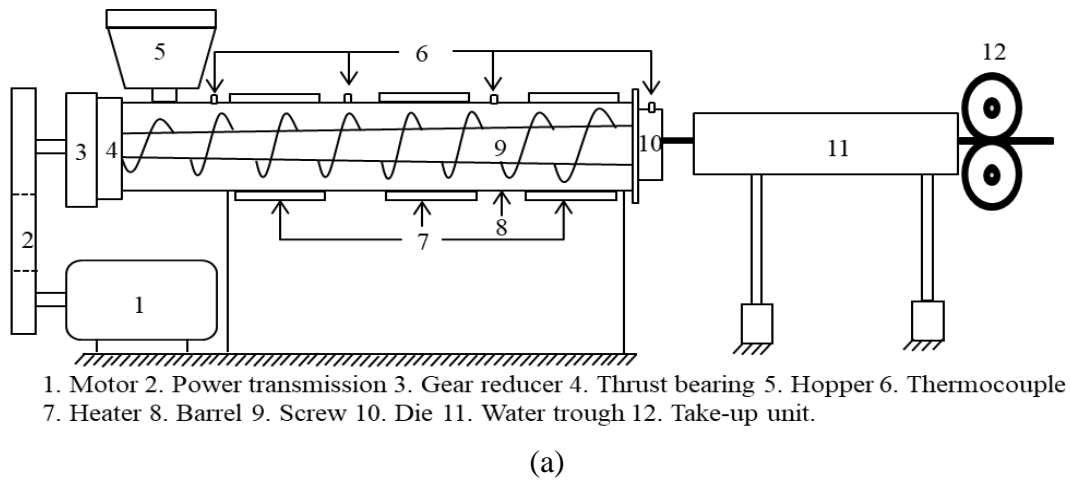


Figure 2.5 (a) Schematic representation of the industrial scale single screw extruder and (b) experimental setup.

Table 2.3 Single screw extruder specifications.

Specification	Details
Cooling	Water cooling
Die sizes	1.75, 2.5 and 3 mm.
Drive	3 HP ACVF Drive, Max. RPM 60.
Heaters	Ceramic in SS cover, 4 nos. with load up to 5 Kw.
Heating control panel	PID controllers with 5 zones, Accuracy $\pm 1^\circ\text{C}$, Max. Temp. 450°C .
Hopper	Min. 3 Kg, SS sheet with discharge chute.
Make and Model	Aasabi Machinery (P) Ltd. Dombivli, Mumbai, India. (25SS/MF/26, L/D ratio of 25:1)
Pelletizer	Helical type, minimum 4" dia. \times 4" L with 0.5HP ACVF drive.
Screw	High tensile nitride hardened alloy steel to sustainable up to 450°C , Dia. 25 mm with length 26D having uniform discharge.
Spooling arrangement	Take up rollers with 0.5 HP ACVF drive with height adjustments and castor wheels

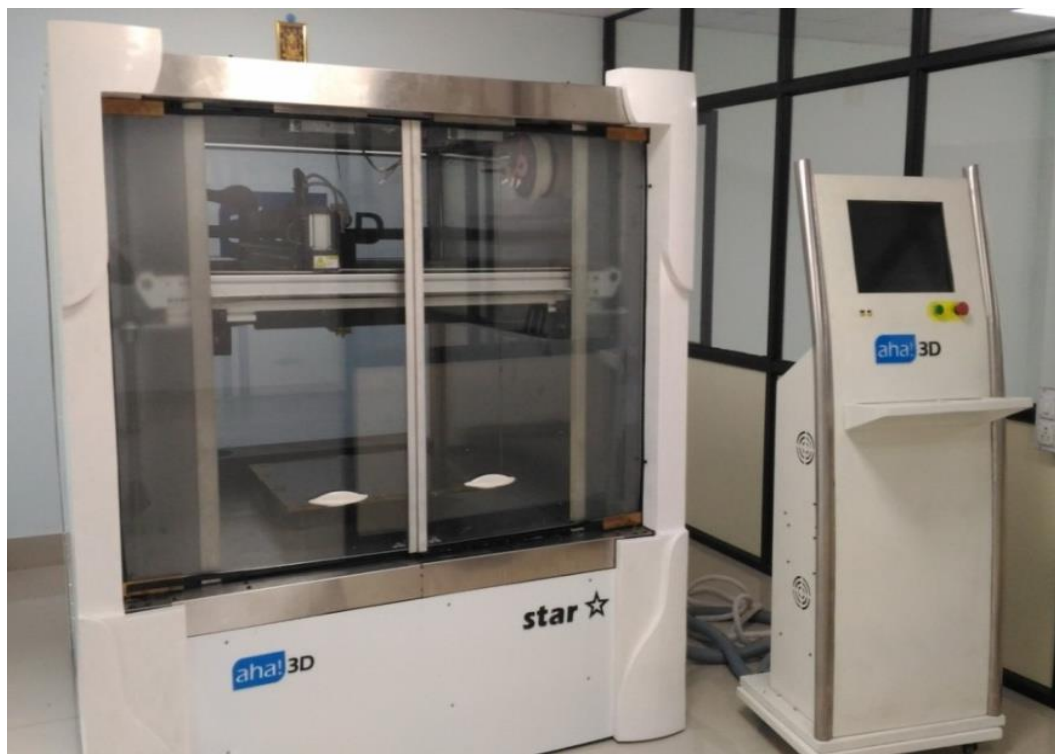
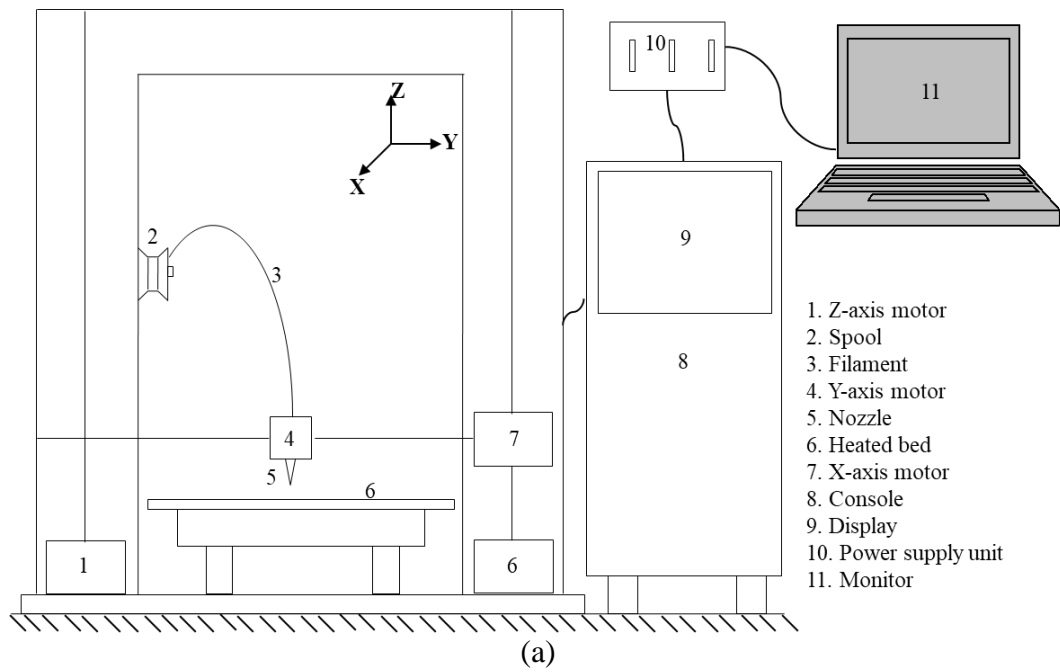


Figure 2.6 (a) Schematic representation of FFF printer and (b) FFF printer utilized in the present work.

Table 2.4 Specifications of FFF based 3D printer.

Specification	Details
Build chamber	Up to 100°C
Build platform	Up to 150°C
Build volume	500 × 500 × 500 mm ³
Data import format	STL, AMF, OBJ
Filament diameter	3 mm (Standard)
Layer height	100 to 500 microns
Make and model	Aha 3D Innovations Pvt. Ltd., Jaipur, Model: Star
Max. extrusion temp.	Basic tool head: 300 °C, Standard tool head: 500 °C
Number of extruders	2
Positional accuracy	50 micron (stepper), 20 microns (servo), 4 microns (dual servo)
Power requirement	220V AC, three phases
Printing materials	All engineering thermoplastic and Plastic Composites, ABS, HIPS, PC, Nylon, TPU, TPE, Carbon fiber composite, etc.
Rate of production	Basic tool head: up to 15 cm ³ /hr., Standard tool head: Up to 150 cm ³ /hr.
Screw	High tensile nitride hardened alloy steel to sustainable up to 450°C. Suitable compression ratio (at least Dia. 25 mm with length 26D) having a uniform discharge at metering zone.
Technology	Fused Filament Fabrication (FFF)
Tool head cooling	liquid cooled.
Workstation compatibility	Windows XP, Windows 7, Linux

2.6 Differential scanning calorimetry (DSC)

PerkinElmer DSC-6000, USA, is used to estimate the melting and crystallization behavior of filaments and prints of H - H60 compositions. The specimen weighing 10 mg is heated in a 30 μ L Al crucible for a 0 - 200 °C temperature range with isothermal curing at 200 °C for about 3 min. Later, samples are brought to zero degrees at a rate of 10°/min, eliminating thermal history because of earlier processing steps. Post cooling at 0 °C for 3 min, the samples are heated again from 0 to 200 °C. DSC plots display endothermic and exothermic peaks, representing melting enthalpy at cold crystallization. Crystallinity % (α_{Cryst}) is assessed as (Lee et al. 1995),

$$\alpha_{Cryst} = \frac{\Delta H_m}{\Delta H_m^*(1-W_{GMB})} \times 100 \quad (2.1)$$

where, ΔH_m = heat of fusion in J/g and ΔH_m^* = heat of fusion/gram of HDPE i.e., 293 J/g (Divya et al. 2013) and W_{GMB} = weight fraction of GMBs.

2.7 Coefficient of thermal expansion (CTE)

A dilatometer, CIPET, Chennai, is used to estimate CTE for prints (ASTM D696-13) having a dimension of $75 \times 12.7 \times 3$ mm. CTE values qualitatively exhibit warpage and correlates the effect of filler loading on dimensional stability and microstructural analyses (Fitzharris et al. 2018). CTE is performed in the temperature range of 20 - 90 °C. An average of five samples is reported for investigation.

2.8 Density

According to ASTM D792-13, experimental densities of the filaments and prints are calculated. Using the rule of mixture, the theoretical density is determined by,

$$\rho_c = \rho_f V_f + \rho_m V_m \quad (2.2)$$

where, ρ_c , V , f , and m are the density of composite, volume fraction, filler, and matrix, respectively. The theoretical density of sandwich composites is determined by,

$$\rho_{th} = V_s \rho_s + V_c \rho_c \quad (2.3)$$

where, s and c are skin and core of sandwich composite. Furthermore, the difference in theoretical (ρ^{th}) and experimental (ρ^{exp}) densities give % void content (Φ_V) and is given by (Gupta et al. 2004),

$$\Phi_V = \frac{\rho^{th} - \rho^{exp}}{\rho^{th}} \quad (2.4)$$

2.9 Tensile response

Filament and 3D printed samples are tensile tested using Zwick Roell Z020, USA, with a 20 kN load cell. The total length of the filament is 176 mm, with 76 mm as the distance between the grips. The test is carried out by maintaining a constant 5 mm/min loading rate. An extensometer (gauge length 50 mm) is used to measure the strain. The printed samples are tested according to ASTM D638-14, at similar crosshead displacement using a 25 mm extensometer gauge length. An initial load elongation of 0.1 MPa is recorded using an extensometer. The stress and strain are calculated using the load and displacement data obtained. For each configuration, the average modulus and strength values of five specimens are considered.

2.10 Flexural behavior of 3D printed core and sandwich

The flexural testing of the 3D printed core of sample dimension $127 \times 12.7 \times 3.2 \text{ mm}^3$ (ASTM D790-17) and sandwich of sample dimension $180 \times 18 \times 8 \text{ mm}^3$ (ASTM C393-16) is performed in a three-point bend configuration using a computer-controlled Zwick (Zwick Roell Z020, ZHU) machine having a load cell capacity of 20 kN. The strain rate of 0.01 S^{-1} and a preload of 0.1 MPa is considered. The loading rate of 1.37 mm/min for core and 3.41 mm/min for sandwich samples, with a span length to depth ratio of 16:1, is maintained. A minimum of five samples are tested, and the average values with standard deviations are reported. The test is terminated at a 10% strain in the case sample does not fail. Flexural modulus is computed using,

$$E_{fM} = \frac{L^3 m}{4bd^3} \quad (2.5)$$

where L is the support span (mm), b is the width of beam (mm), d is the thickness of beam (mm), and m is the slope of the tangent to the initial straight-line portion of the load-deflection curve. The flexural stress (σ_{fs}) is calculated by,

$$\sigma_{fs} = \frac{3PL}{2bd^2} \quad (2.6)$$

where, P is the load (N) at a given point on the load-deflection curve.

2.11 Compression response of 3D printed core and sandwich

The compression tests of 3D printed core and sandwich samples (ASTM C365M-16) are conducted using a Zwick (Zwick Roell Z020, ZHU) computer-controlled universal test system with a 20 kN load cell. The test is conducted at a constant crosshead displacement velocity of 0.5 mm/min. The criteria for the end of the test are set at 20 kN load. An in-house developed MATLAB code is used to analyze the data. The peak stress at the end of the elastic region determines the compressive strength. At least five samples of each volume fraction are examined to ensure accuracy.

2.12 Buckling and free vibration investigation

2.12.1 Buckling of 3D printed core

The buckling test of printed HDPE and syntactic foams under axial compressive loads having clamped-clamped condition is performed on an H75KS, Tinius Olsen universal testing machine (50 kN load cell) at 0.2 mm/min crosshead displacement. For the buckling test, samples of $210 \times 12.5 \times 4$ mm in length, width, and thickness respectively have been used (Waddar et al. 2018, Waddar et al. 2019), and an average of five tested samples is reported. The end shortening of 0.6 mm is considered to study the behavioral change in the post-buckling region based on the preliminary tests. Figure 2.7 presents a schematic of the experimental setup utilized for mechanical buckling and vibration under a compressive load.

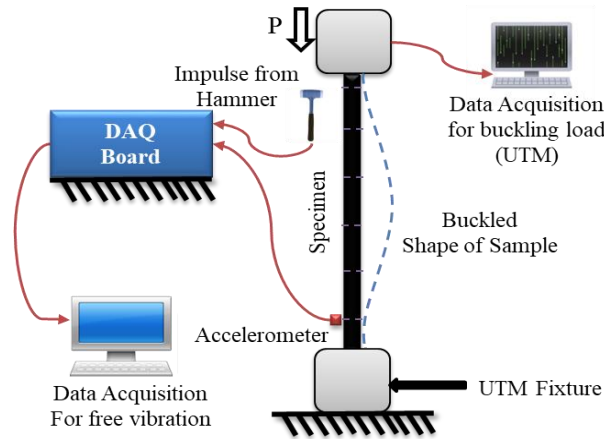


Figure 2.7 Schematic of the experimental setup utilized for mechanical buckling and vibration under a compressive load.

The DTM and MBC approaches are employed to estimate critical buckling loads enabling robust structural designs. The method to construct tangents for load-deflection curves obtained experimentally for DTM and MBC (Shariyat 2007, Tuttle et al. 1999) is illustrated in Figure 2.8 for a representative printed sample. Two tangents in the pre and post-buckling zones are drawn in the DTM method. The intersection of two tangents gives the critical load, as shown in Figure 2.8a. In the MBC method, the critical buckling load value corresponds to a point on the curve where the bisector drawn at the intersection point of both tangents meets, as seen from Figure 2.8b. Both DTM and MBC methods are reported for comparisons due to a lack of existing literature on buckling and vibration response of 3D printed HDPE and their syntactic foams.

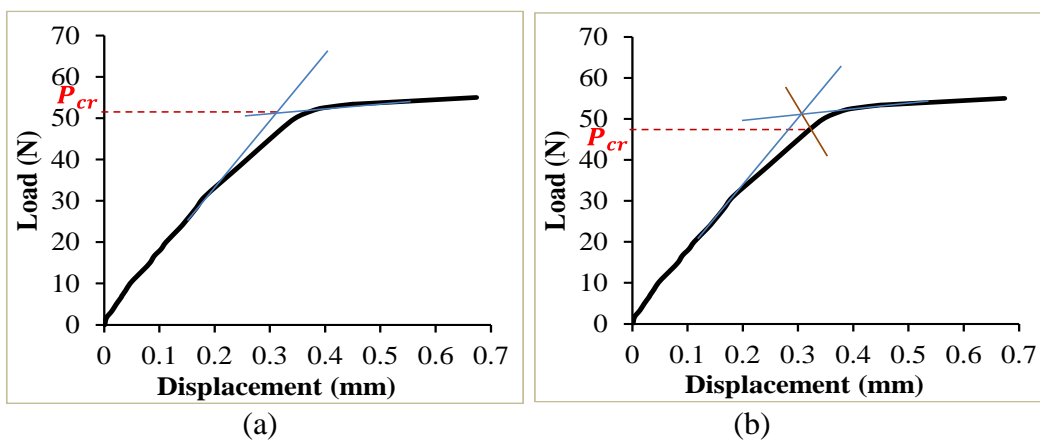


Figure 2.8 Representative load-deflection plots for estimating P_{cr} using (a) DTM and (b) MBC for representative H20 print.

2.12.2 Free vibration of 3D printed core

The first three natural frequencies of printed HDPE and their foam beams under axial compressive loads with clamped-clamped conditions are measured and monitored through experimental modal analysis (Figure 2.9). A uniaxial lightweight accelerometer (8778A500) with 10 mV/g sensitivity and ± 500 g operating range is used to record the vibration signals by exciting the samples using 9722A2000 Kitsler impulse hammer with a sensitivity 10 mV/N. Using the bee's wax, the accelerometer is mounted onto the specimen. DEWESoft software records response signals, and using a fast Fourier transform algorithm, it converts time-domain signals to a frequency domain to measure natural frequency and modes. The modal analysis through the experimental route is conducted with 20 N load increments until the sample deflection of 0.60 mm. The modal analysis is performed in situ by holding an ongoing compressive load for 2 minutes.

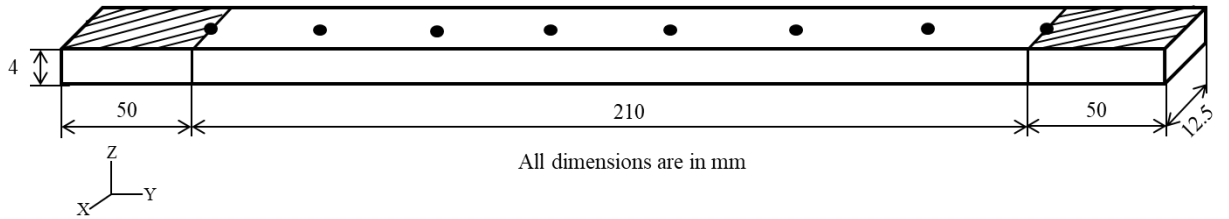


Figure 2.9 Schematic diagram of specimen used in free vibration test.

2.12.3 Bradella-Genna model for estimating young's modulus

The modulus of HDPE and foam samples are estimated using Bardella–Genna model (Bardella and Genna 2001), and results are compared with experimental values. This model uses a homogeneous method to predict the shear and bulk modulus and is determined by the following equations.

$$K_{bulk} = K_m \frac{\delta(1+\phi\gamma)+k(1+\phi\gamma)}{\delta(1-\phi)+k(\gamma+\phi)} \quad (2.7)$$

where,

$$\gamma = \frac{4G_m}{3K_m} \quad (2.8)$$

$$\delta = \frac{4G_f}{3K_m}(1 - \eta^3) \quad (2.9)$$

$$K = \frac{4G_f}{3K_f} + \eta^3 \quad (2.10)$$

The HDPE matrix's modulus and Poisson's ratio are taken as 810.25 MPa (Table 4.1) and 0.425 (Kumar et al. 2016), respectively. Similarly, the Poisson's ratio and modulus of GMB are taken as 0.21 and 60000 MPa (Tagliavia et al. 2010), respectively. The radius ratio of GMB particles is estimated using true particle and glass density of GMB (Shunmugasamy et al. 2014, Tagliavia et al. 2010) and is taken as 0.914. The shear modulus is obtained from the equation as mentioned in Ref. (Shariyat 2007). The foam modulus is estimated using Equation 2.11 (Thomson WT 2008).

$$E = \left(\frac{\omega_j}{\beta_j^2}\right)^2 \left(\frac{\rho^{exp} AL^4}{I}\right) \quad (2.11)$$

$$\text{where, } \omega_j = 2\pi f \quad (2.12)$$

The rule of mixtures is used to find the Poisson's ratio and density of the syntactic foams. β_j in Equation 2.11 is a constant corresponding to a particular mode, and for the first mode, it is taken as 4.73 under clamped-clamped boundary conditions (Thomson WT 2008). In this model, the voids present in the samples are assumed to be volume occupied by the matrix. The Young's modulus of foam is computed using Equation 2.13.

$$E = \frac{9KG}{3K+G} \quad (2.13)$$

2.12.4 Theoretical formulation

The shape of hollow GMB particles is spherical, and the dispersion of GMB in the HDPE matrix is observed to be uniform. Hence, the GMB/HDPE syntactic foam

composite can be modeled as isotropic material. Furthermore, it is expected that SF act as linearly elastic. The differential beam equation of the motion under axial compression, neglecting shear deformation and rotating effects of inertia, is given by (Bokaian 1988) as,

$$EI \left(\frac{\partial^4 y(x)}{\partial x^4} \right) + P \left(\frac{\partial^2 y(x)}{\partial x^2} \right) - \rho A \left(\frac{\partial^2 y}{\partial t^2} \right) = 0 \quad (2.14)$$

where, $y = y(x, t)$ and for normal mode of oscillation of the beam. Governing differential equation of motion of a beam subjected to axial compressive load derived based on the Euler-Bernoulli hypothesis is presented by Equation 2.14. In this equation, the first term represents the bending stiffness of the beam, the second term describes work done by the applied axial force, and the last term represents the inertia force of the beam.

$y(x, t) = Y(x) \cos \omega t$, then Equation 2.14 becomes,

$$EI \left(\frac{\partial^4 Y(x)}{\partial x^4} \right) + P \left(\frac{\partial^2 Y(x)}{\partial x^2} \right) - \rho A \omega^2 Y(x) = 0 \quad (2.15)$$

The solution for Equation 2.15 can be expressed by accounting dimensionless beam co-ordinate $\zeta = \frac{x}{l}$ ($0 \leq \zeta \leq L$).

$$Y(X) = Y(l\zeta) = D_1 \sinh M\zeta + D_2 \cosh M\zeta + D_3 \sin N\zeta + D_4 \cos N\zeta \quad (2.16)$$

where D_1, D_2, D_3 and D_4 are constant coefficients, M and N can be expressed as,

$$M = L \sqrt{\left\{ -\left(\frac{P}{2EI} \right) + \left[\left(\frac{P}{2EI} \right)^2 + \left(\frac{\rho A}{EI} \right) \omega^2 \right] \right\}} \quad (2.17)$$

$$N = L \sqrt{\left\{ \left(\frac{P}{2EI} \right) + \sqrt{\left[\left(\frac{P}{2EI} \right)^2 + \left(\frac{\rho A}{EI} \right) \omega^2 \right]} \right\}} \quad (2.18)$$

$$M = \sqrt{(-V + \sqrt{V^2 + \Omega^2})} \quad (2.19)$$

$$N = \sqrt{(V + \sqrt{V^2 + \Omega^2})} \quad (2.20)$$

where, $V = \frac{PL^2}{2EI}$; $\alpha = \sqrt{\frac{EI}{\rho A}}$ and $\Omega = \frac{\omega L^2}{\alpha}$

By differentiating Equation 2.16, we get,

$$\frac{dY}{dx} = MD_1 \cosh M\zeta + MD_2 \sinh M\zeta + ND_3 \cos N\zeta - ND_4 \sin N\zeta \quad (2.21)$$

$Y(x) = 0$, $\frac{dY(0)}{dx} = 0$, $Y(L) = 0$ and $\frac{dY(L)}{dx} = 0$ are the boundary conditions for the clamped-clamped scenario. The substitution of these boundary conditions in Equation 2.16 and Equation 2.21 leads to a non-trivial solution. By taking zero determinant of the coefficient for the non-trivial solution,

$$\begin{vmatrix} 0 & 1 & 0 & 1 \\ M & 0 & N & 0 \\ \sinh M & \cosh M & \sin N & N \\ M \cosh M & M \sinh M & N \cos N & -N \sin N \end{vmatrix} = 0 \quad (2.22)$$

$$(M^2 - N^2) \sin N \sinh M + 2MN(1 - \cos N \cosh M) = 0 \quad (2.23)$$

Substituting the values of M and N in terms of V and Ω in Equation 2.23,

$$\begin{aligned} &\Omega - V \sin \sqrt{(V + \sqrt{V^2 + \Omega^2})} \sinh \sqrt{(-V + \sqrt{V^2 + \Omega^2})} - \\ &\Omega \cos \sqrt{(V + \sqrt{V^2 + \Omega^2})} \cosh \sqrt{(-V + \sqrt{V^2 + \Omega^2})} = 0 \end{aligned} \quad (2.24)$$

The characteristic equation expressed in Equation 2.24 gives variation in natural frequencies for the compressive load. MATLAB code is used to solve Equation 2.24 numerically, and frequency-compressive load plots are obtained and compared with experimental values.

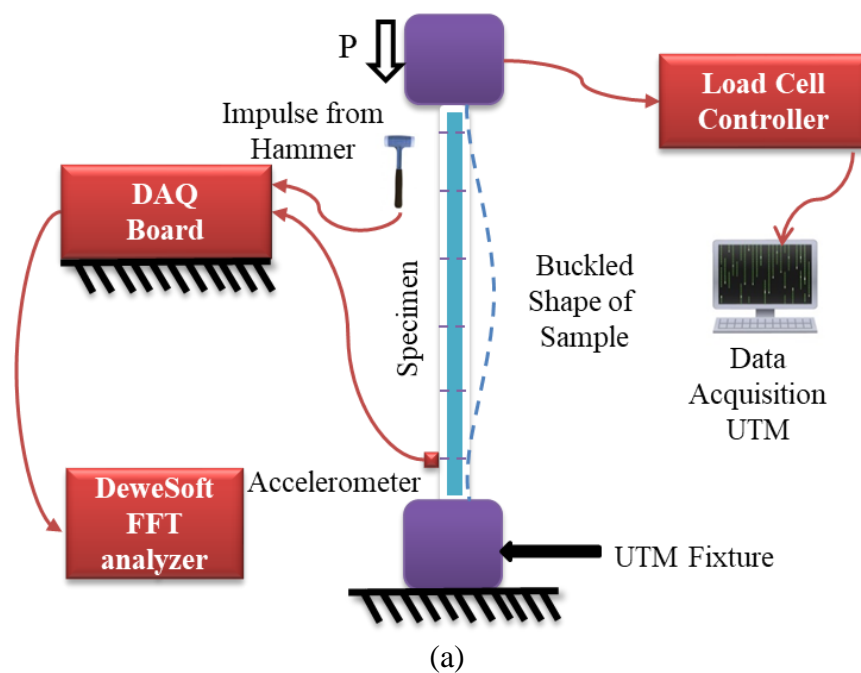
2.12.5 Vibration correlation technique (VCT)

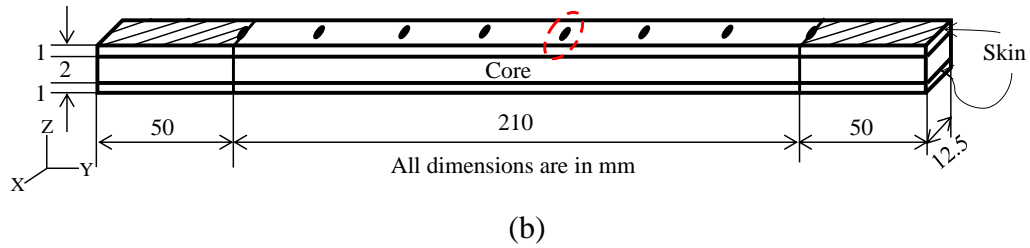
Estimation of critical buckling load from the pre-buckling stage for composites beams is carried out using a non-destructive method known as vibration correlation technique (VCT). There are two types of VCT methods, namely, an indirect and direct method (Singer et al. 2003). The indirect method estimates the actual boundary conditions enabling the buckling load estimation (Singer et al. 2003), while the direct method is based on the extrapolation of an experimental functional relationship between the applied compressive load and the natural frequency. In this present investigation, a direct approach is utilized to extrapolate the buckling load of the 3D prints.

2.12.6 Buckling of 3D printed foam cored sandwich

Buckling analysis has become increasingly important, particularly in engineering design safety as the actual stress at the point of failure is much lower than the material's ability to sustain the applied loads (Goel et al. 2021). H75KS UTM (50 kN loading capacity) supplied from Tinius Olsen, UK, is used for performing buckling investigations with a 0.2 mm/min cross-head displacement. Figure 2.10a represents the actual buckling test setup of sandwich samples. The end shortening is limited to 0.70 mm for observing the behavioral deflection changes in both, i.e., pre and post buckling scenarios. The experimental P_{cr} is estimated graphically by DTM - Double Tangent method and MBC - Modified Budiansky criteria approaches using load and deflection data acquired from a universal testing machine (Matsunaga 1996, Tuttle et al. 1999). DTM typically uses tangents drawn from the pre-buckling and post-buckling regimes to load-deflection curve wherein the two tangents point of intersection is considered as P_{cr} as mentioned in the preceding sections. The P_{cr} MBC

deals with a point bisecting the two tangents drawn to the load-deflection plots (Waddar et al. 2018). Both the MBC and DTM are most widely used for P_{cr} estimations as they predict lower and upper bounds. Thereby, in the present work too, these methods are utilized. Figure 2.10a represents the representative sketch of the experimental setup used to compute the fundamental frequencies through modal analysis for the first three bending modes of concurrently printed sandwich composites having clamped-clamped boundary constraints. A lightweight uniaxial type Kistler accelerometer (sensitivity: 10 mV/gm, operating range: ± 500 gm) is used to acquire the response by exciting through Kistler's impulse hammer (10 mV/N sensitivity). For better adhesion of the accelerometer with samples, Bee's wax is used, as mentioned earlier. FFT is used to convert the time domain to frequency domain signal with the help of DEWE Soft. FRF is deduced from different locations along the length \times width area, as marked in Figure 2.10b. The DEWE Soft directly gives the frequency and vibration mode shape. The test is progressed from zero (no-load condition) to P_{cr} with 20 N load increments and a pause for 2 min post every load increment, extract the mode shapes by exciting at the marked locations (Figure 2.10b). A similar procedure is followed for all the printed samples.





(b)
Figure 2.10 Schematic representation of the (a) experimental setup and (b) sample configuration.

2.12.7 Numerical analysis

The numerical Eigen buckling and modal analysis of 3D printed foam cored sandwiches are performed using the FEA (Rajesh and Pitchaimani 2017, Waddar et al. 2019). The elastic moduli and Poisson's ratio of core and skin are also computed for frequency and load estimations. HDPE and GMB/HDPE core modulus are calculated using the Bradella-Genna model (Bardella and Genna 2001). The Poisson's ratio of the HDPE is taken as 0.425 (Kumar et al. 2016), while for GMB, it is considered to be 0.25 (Tagliavia et al. 2010). Poisson's ratio of GMB/HDPE core is estimated using the rule of the mixture as,

$$\nu_{12} = \nu_m V_m + \nu_f V_f \quad (2.25)$$

The experimental results are compared with numerical predictions using the steps as illustrated in Figure 2.11a. The elastic properties of SFs are calculated using the homogenization approach from the Bradella-Genna model based on the radius ratio and volume fraction (Bardella and Genna 2001). The sandwich is modeled as a layered entity using four noded SHELL181 elements (Figure 2.11b). The skin and core of the sandwich are modeled as an isotropic layer with respective material properties.

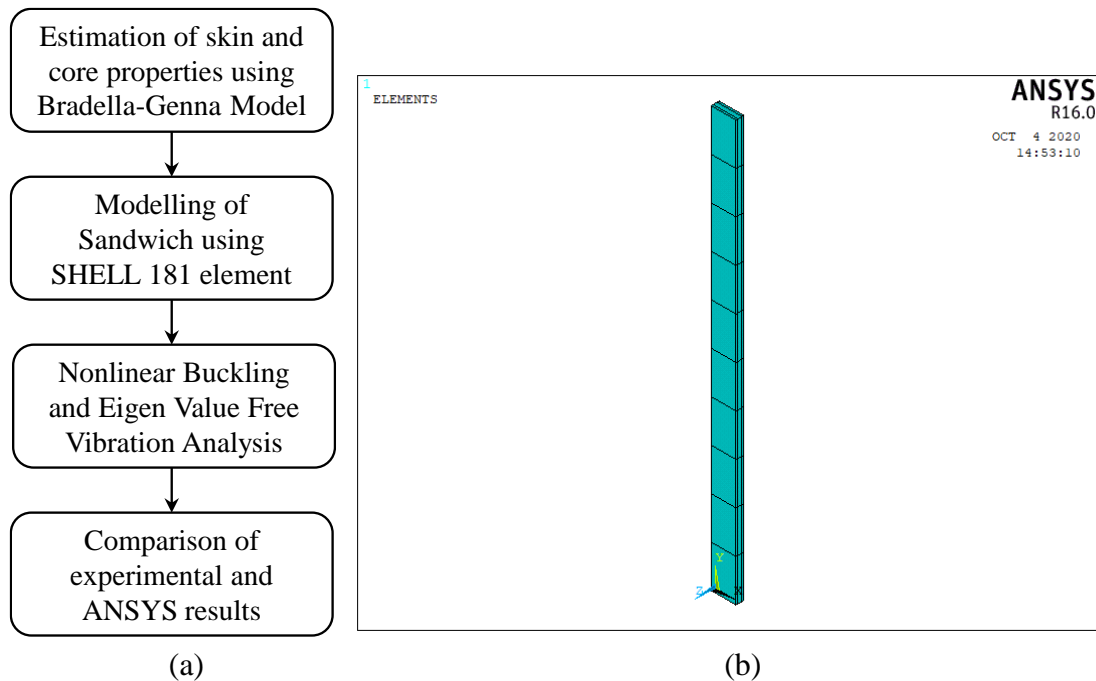


Figure 2.11 (a) Numerical analysis steps and (b) FEA Model of the Sandwich composite.

The displacement boundary condition and compressive load are applied. In the absence of an axial compressive load, the first three natural frequencies of the sandwiches obtained from the experiment are compared with numerical predictions of the modal analysis. The natural frequency is estimated by solving the Eigenvalue problem and compared with experimental values. The non-linear buckling analysis is carried out using finite element software (ANSYS). Initially, the fundamental buckling modes of sandwiches are derived from linear Eigenvalue buckling analysis. Furthermore, to obtain the load-deflection curves, the fundamental buckled mode shape and a selected geometrical imperfection factor are fed to the non-linear analysis. The numerically obtained load-deflection curve is governed by the geometrical imperfection factors (SH20 - 0.001, SH40 - 0.00015, and SH60 - 0.0001). S denotes Sandwich.

2.13 Microstructural characterization

Extensive micrography is carried out on extruded filaments, as printed core and sandwiches, and post-tested filaments and prints using a scanning electron

microscope (SEM) JSM 6380LA JEOL, Japan. All the samples are coated with gold sputter covering using JFC-1600 auto fine coater.

3 MATERIAL CHARACTERIZATION AND PROCESSING ASPECTS

3.1 Blend characterization

GMB/HDPE blends are characterized for MFI and rheology.

3.1.1 MFI of HDPE and GMB/HDPE blends

Flowability is quantified by MFI. An increase in GMB content reduces MFI due to filler resistance to the flow of polymer (Escócio et al. 2015). HDPE has recorded the highest MFI (17.94 gm/10 min) when compared with H20 (13.76), H40 (8.11), and H60 (4.85). MFI decreased by 23.29, 54.79, and 72.97 %, with increasing GMB by 20, 40, and 60 volume %, respectively (Escócio et al. 2015, Mohanty and Nayak 2010). Decreased MFI needs to be carefully looked into either by raising the temperature of printing or increasing the print extrusion multiplier, especially for foams with higher filler loadings. The printing temperature is kept constant for H - H60 to consolidate the warpage, and hence multiplier factor is changed for higher GMB %.

3.1.2 Rheology of HDPE and GMB/HDPE blends

Frequency sweep

An increase in filler infusion increases melt viscosity of the polymer (Shaikh et al. 2016) and is observed in the entire frequency sweep (Figure 3.1a). At higher frequency, HDPE shows a shear-thinning region. H20 - H60 shows similar behavior with a slight increase in complex viscosity (η') and is due to the restriction of polymer chain movements by GMBs. Among foams, H60 shows the highest η' . At 0.1 and 50 rad/sec, complex viscosities for H, H20, H40 and H60 are in the range of 1080.52 - 636.75, 2045.4 - 1048, 2729.6 - 1324.2 and 4331.4 - 1701.5 Pa-s respectively. Compared to H (11808 Pa at 50 rad/sec), foams have higher storage modulus (G') owing to the presence of a greater number of stiffer particles (Figure 3.1b). Storage modulus increases from 20,019 - 32,163 Pa for H20 - H60 foams. HDPE and H20 display standard homopolymer-like terminal behavior at lower frequencies due to the complete relaxation of polymer chains (El Achaby et al. 2013). Compared to pure HDPE, H20 has a higher modulus. The Plateau region is observed at a lower frequency for H40 and H60, indicating viscoelasticity. Loss modulus (G'') increases

with increasing frequency and filler content for all the samples (Figure 3.1c). The loss modulus for H - H60 ranges between 107.56 - 429.56 Pa, respectively, at 0.1 rad/sec, which is ~4 times for H60 as compared to H. Such a multifold increase in G'' could be due to restrained matrix flow around stiff intact GMBs.

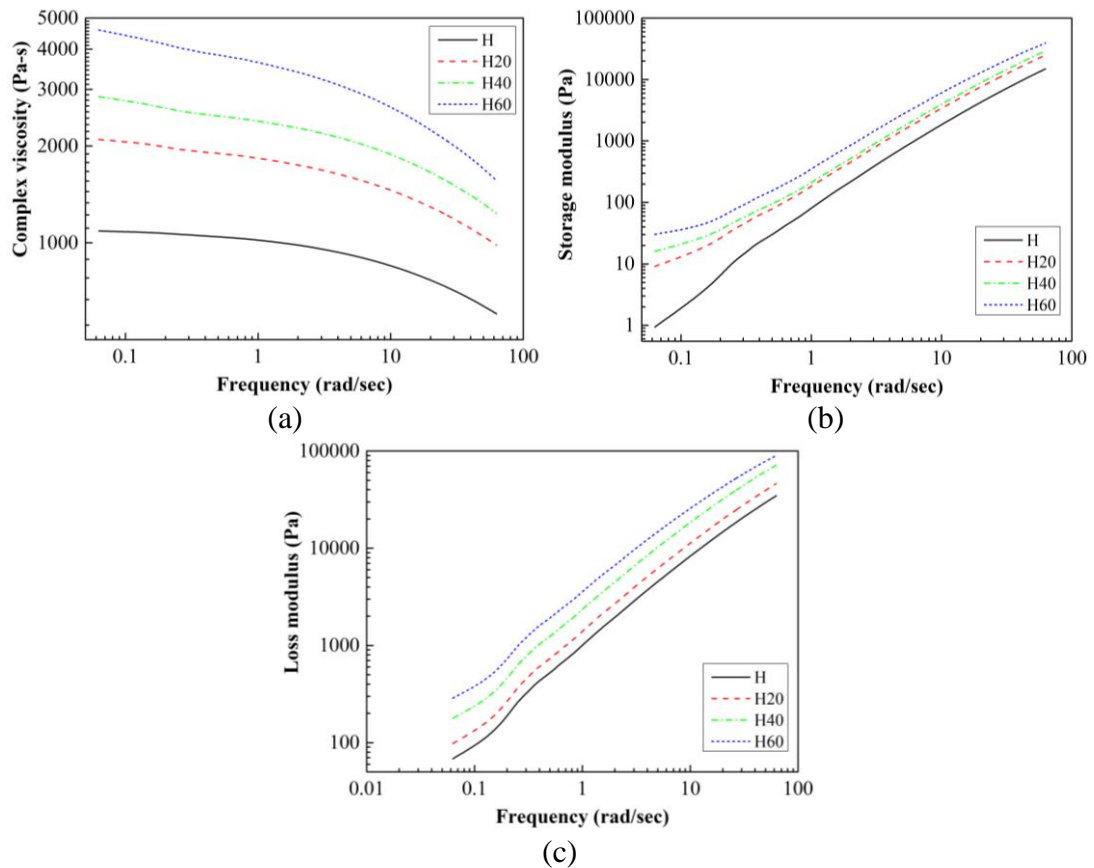


Figure 3.1 (a) Complex viscosity (b) storage modulus and (c) loss modulus as a function of frequency for HDPE and their blends.

Temperature sweep

Temperature sweep plots of HDPE and their foams at 1 Hz are depicted in Figure 3.2. Figure 3.2a shows that the storage modulus of neat HDPE and foams decreases as the temperature increases throughout the temperature sweep. The gap between storage modulus curves tends to decrease as temperature increases. This implies that GMB content has a lower impact on storage modulus at higher temperatures than at lower temperatures. The gap between storage modulus curves increases at low temperatures, and all curves are significantly separated. Since the storage modulus in viscoelastic

materials represents the molecular elastic response, its effect decreases as the temperature increases. Lower bonding strength and higher mobility of polymer chains may explain the reduced storage modulus at higher temperatures. A similar observation is deduced from loss modulus as in Figure 3.2b. The loss modulus is greater than the storage modulus, suggesting viscous segmental friction between GMB and the polymer melt resulting in higher viscosity. Figure 3.2c shows the results of $\tan \delta$ plotted against temperature. $\tan \delta$ is the proportion of viscous (loss modulus) to elastic section (storage modulus). The values of $\tan \delta$ determine the melting behavior (liquid or solid). From the $\tan \delta$ curve, it is clear that the viscous component contributes the most in the temperature sweep. It is also evident from the existing discussions that, as GMB content increases, melt viscosity increases.

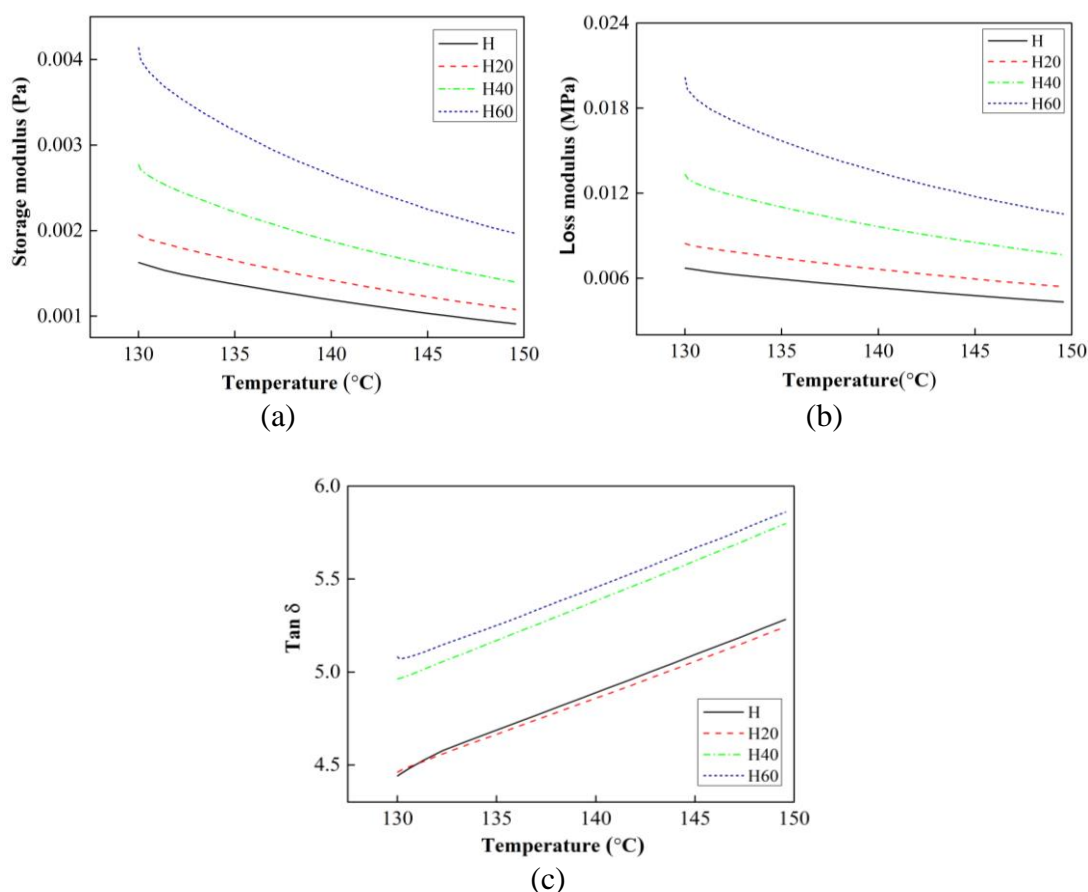


Figure 3.2 (a) Storage modulus (b) loss modulus and (c) $\tan \delta$ as a function of temperature for HDPE and their blends.

Rheological and MFI properties act as a guideline for selecting appropriate process parameters for printing quality components. As a result, processing parameters must be carefully studied based on MFI and rheological investigations.

3.2 Filament development

Single screw extruder (Figure 2.5b) of type 25SS/MF/26 supplied by Aasabi Machinery Pvt. Ltd., Bombay, India, with an L/D ratio (flight length of screw to its outside diameter) of 25:1 is used to extrude HDPE and foam filaments. The HDPE granules (Figure 2.1b) and H20 - H60 blends (Figure 2.2c) are dried at 80 °C in the oven for 24 h before gravity feeding into the hopper to eliminate the moisture if any. The quality of extruded filament depends on barrel temperature, die temperature, screw speed, and take-off unit speed. The suitable barrel and die temperatures convert solid pellets into semi solid-state and extrude them from the die without any material blockage. The extruder's semi viscous mass is passed through a water tank to be pulled by the take-off unit. The filament size depends on the extrusion rate (screw speed and take-off speed). HDPE and foam pellets are fed to the extruder having a temperature profile of 145-150-155-145 °C. The extruder screw rotates at a speed of 25 rpm. The extruder's filaments are spooled using a take-off unit having a speed of 11.5 rpm. Using all these suitable extrusion parameters, filaments of diameter 2.85 ± 0.05 mm are extruded (Figure 3.3). Ovality of the extruded filaments can be minimized by suitably adjusting the distance between two rollers at the take-off side of the extruder in addition to the speed regulations. All these parameters have been chosen by considering HDPE melting temperature, uniform and homogeneous mixing of GMB in HDPE without breakage, rheological behavior of blends, and presence of porosity, if any, during extrusion.

The performance and behavior of the extruded foam filaments are influenced by the interaction of filler-matrix, filler %, and matrix porosity. For filaments to be used in a 3D printer, adequate spooling stiffness and strength are needed. Hence, tests to find the density, morphology (in this section) of extruded filament, and tensile properties

(Chapter 4) are performed before printing to check the quality, stiffness, and strength necessary for filament feasibility to be used in a commercially available printer.



Figure 3.3 Representative extruded H60 feedstock filament.

Table 3.1 presents density estimations, void %, and the weight reduction potential of filaments (F) and prints (Pnt). The experimental and theoretical densities of HDPE filaments are very close, indicating lower void formations due to their hydrophobic nature. Mechanical properties of HDPE and foams are influenced by voids presence, as an effective load bearing area reduces. GMB content increases void content in filaments (2.50 - 7.70%) and prints (6.14 - 9.73%). Higher void content in print compared to filaments indicates matrix porosity is transferred from the filaments to prints. Further, additional porosity of 1.58, 3.64, 4.2, and 2.03% is observed in H, H20, H40, and H60 prints, respectively. Such additional porosity in prints amid 100% infill is due to air gaps (residual micro-porosity) between the raster. These additional porosities form three-phase (HDPE, GMB, and raster gap) SFs enhancing damping capabilities further.

Table 3.1 Physical Properties of Filament (F) and Prints (Pnt).

Material	Φ_f (vol. %)	ρ^{th} (kg/m ³)	ρ^{exp} (kg/m ³)		Φ_V (%)		Weight saving potential (%) w.r.t H	
			F	Pnt	F	Pnt	F	Pnt
H	0	950	942±8	927±12	0.84	2.42	---	---
H20	20	880	858±15	826±13	2.50	6.14	8.92	10.90
H40	40	810	780±11	746±18	3.70	7.90	17.20	19.53
H60	60	740	683±12	668±10	7.70	9.73	27.49	27.94

The extruded filaments did not break even after keeping them in liquid nitrogen for 24 h. Hence, micrographs are taken by cutting them using a knife. The usage of the knife makes the material flow lines visible in the micrographs (Figure 3.4). The circular cross-section in Figure 3.4a of representative H20 filament affirms the suitability of chosen extrusion parameters. Figure 3.4b shows a low magnification micrograph of H60, showing the uniform distribution of intact GMB particles and few voids in the compliant HDPE matrix. Such pores/voids, if transferred during 3D printing, may increase three-phase SFs compliance resulting in higher damping. Poor interfacial bonding between GMB and HDPE is evident from a higher magnification micrograph of H60 (Figure 3.4c). It is evident as constituent materials are used in received conditions, i.e., without any surface treatment, to avoid additional processing time, cost, and difficulty in correlating properties with inconsistently coated layer thickness.

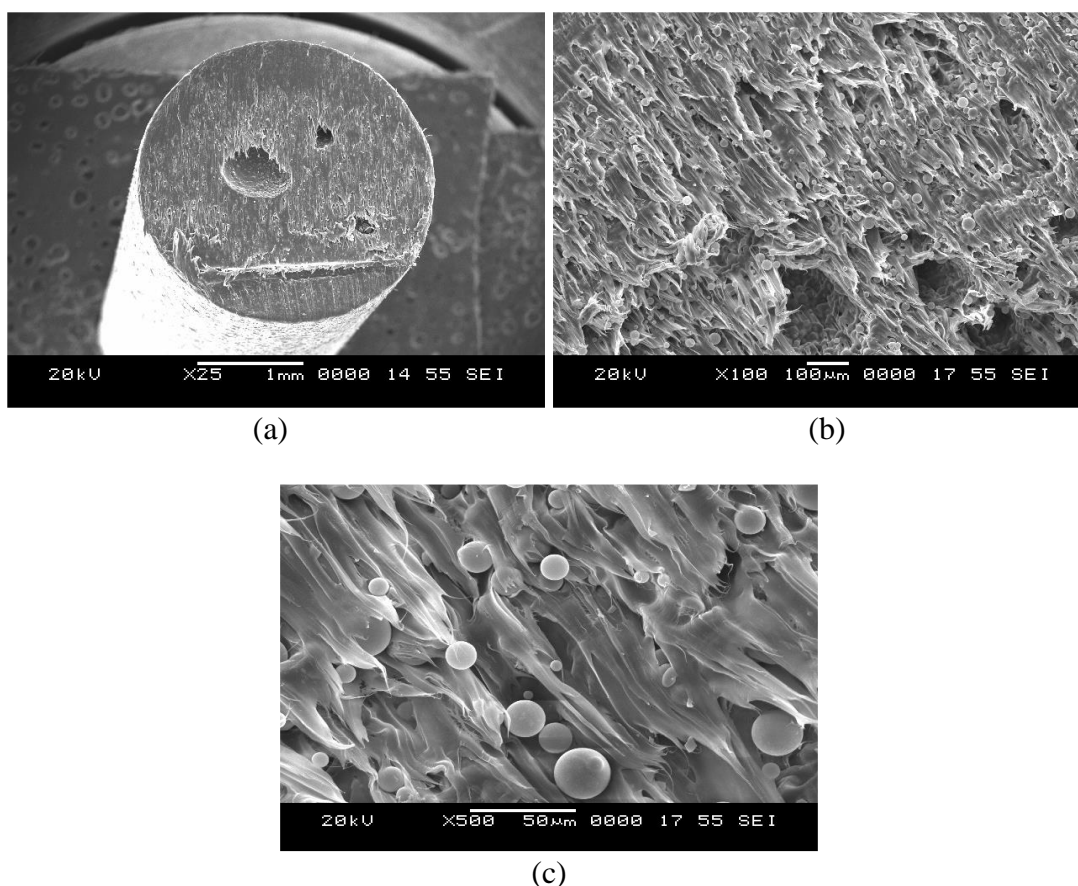


Figure 3.4 Extruded filament micrograph of (a) cross-sectional view for representative H20. H60 at (b) lower and (c) higher magnifications.

3.3 3D printing of syntactic foam core and sandwich

Obtained H - H60 filaments are used as input material for 3D printing of core and sandwich samples. Commercially available FFF based Star 3D printer supplied by AHA 3D Innovations Pvt. Ltd., Jaipur, India, has two nozzles of 0.5 mm diameter. Pilot studies (Table 3.2) are conducted to obtain the suitable printing parameters to print core and sandwiches. The suitable values of temperature and flow rates based on the pilot experiments are set to achieve completely rigid parts with 100% infill compared with fully dense molded components. Printing at higher temperatures can help achieve temperature distribution uniformly alongside the annealing effect, yielding better adhesion of layers and dimensionally stability. Nozzle and bed temperatures below 200 and 60 °C respectively resulted in improper material flow through nozzles and non-uniform bonding of the raft with the HDPE plate placed on the printer's glass bed. Higher material flow through the nozzle and HDPE plate distortion is observed for the nozzle and bed temperatures above 240 and 100 °C, respectively. Table 3.2 and Figure 3.5 show the observations about the experimental tests to identify suitable printing parameters for HDPE.

Table 3.2 Remarks on different 3D printing parameters.

Printing temperature (°C)	Print bed temperature (°C)	Observation	Figure 3.5
200	60	Improper layer deposition	a
220	60	Interlayer defects	b
220	100	Merging of the bottom layer with plate	c
240	100	Maximum warpage, Defective part	d
220	80	Proper layer deposition, Absence of interlayer defects, Easier removal of print from the plate, No warpage	e

Nozzle temperature is set above the Vicat softening point (124 °C) of HDPE. The printing and bed temperatures for printing HDPE are varied across temperature settings of 200 - 230 °C and 60 - 100 °C, respectively. The experiments are carried out based on 3DP of HDPE as it exhibits maximum warpage compared to foams.

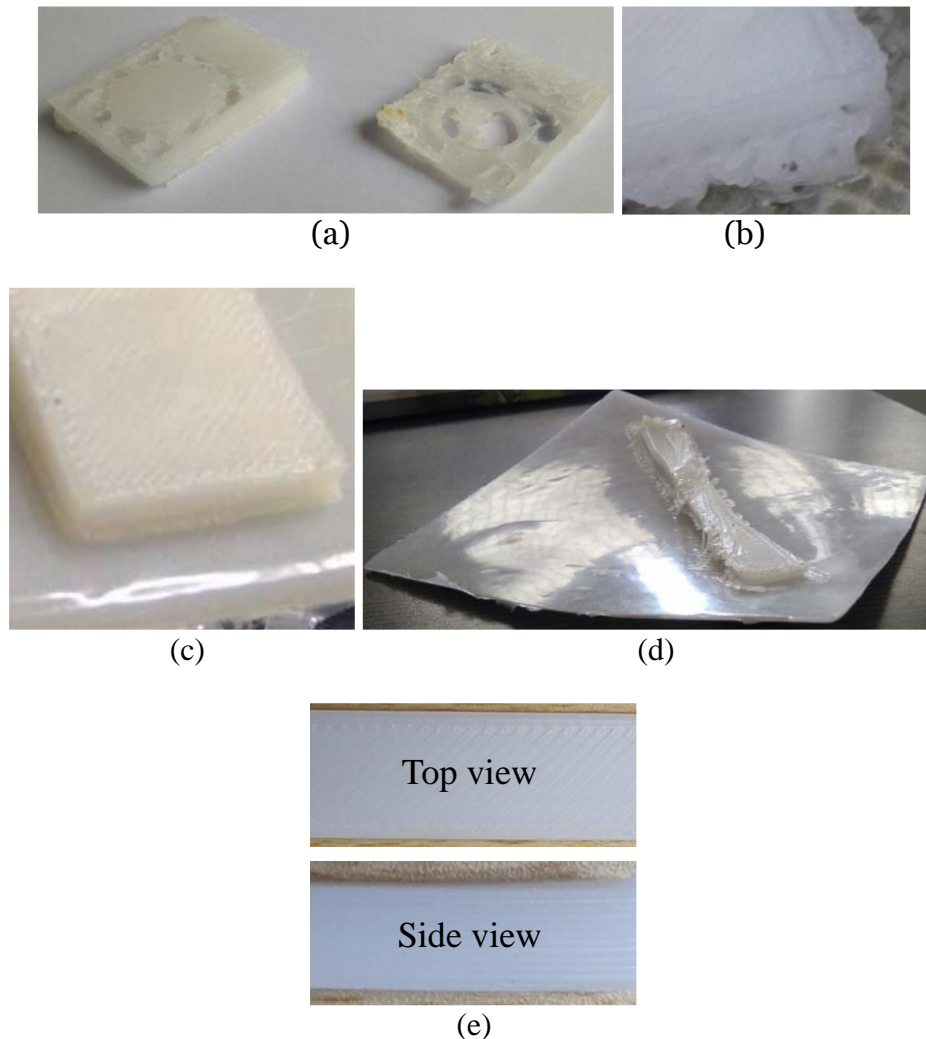


Figure 3.5 Challenges in 3D printing of HDPE (Table 3.2) (a) Improper layer deposition (b) Interlayer defects (c) excessive diffusion (d) maximum warpage and (e) defect free print.

3D printed samples are cooled within the build chamber till room temperature is reached. Printed samples exhibit consistent bonding between the layers with the least warpage (Figure 3.6a). The marked area in Figure 3.6a indicates excellent seamless diffusion between the layers at higher magnification. This fact reaffirms the suitability of printing parameters utilized for HDPE (Table 3.2). Micrographs of freeze-fractured HDPE print show very few voids, as seen from Figure 3.6b and Table 3.1.

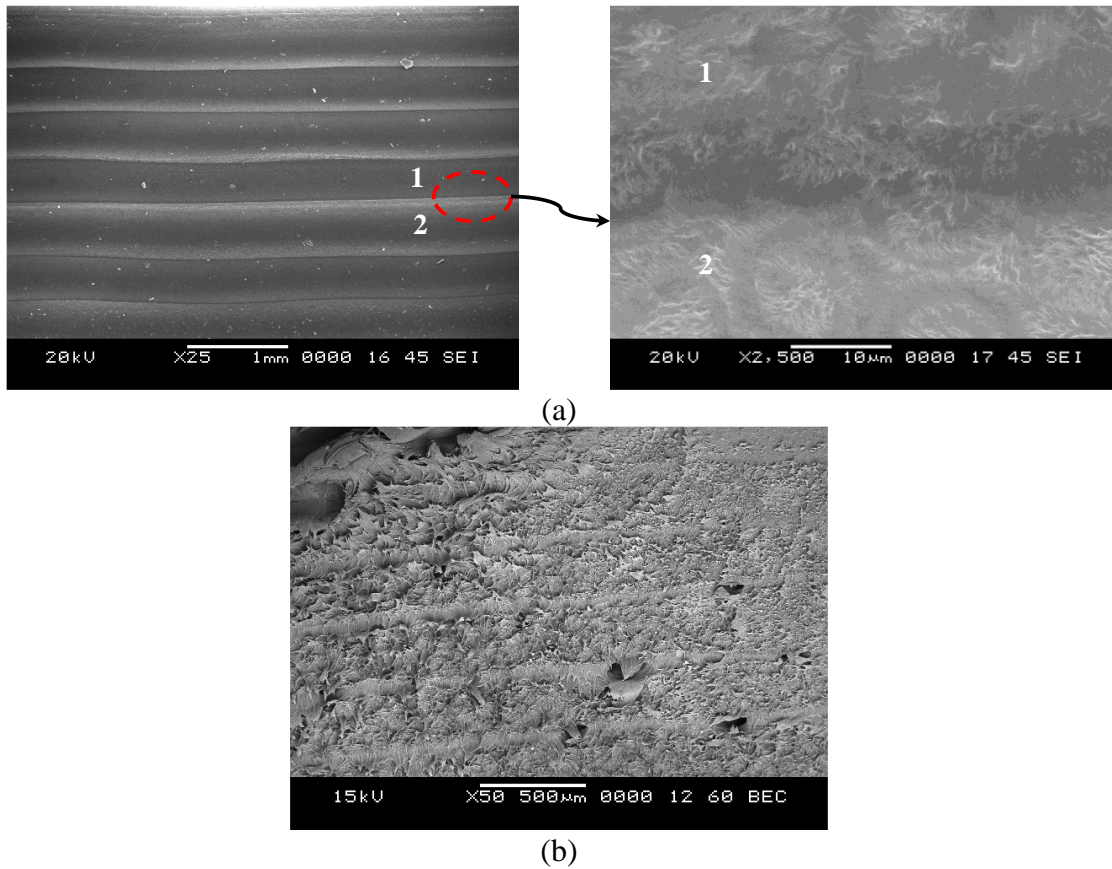


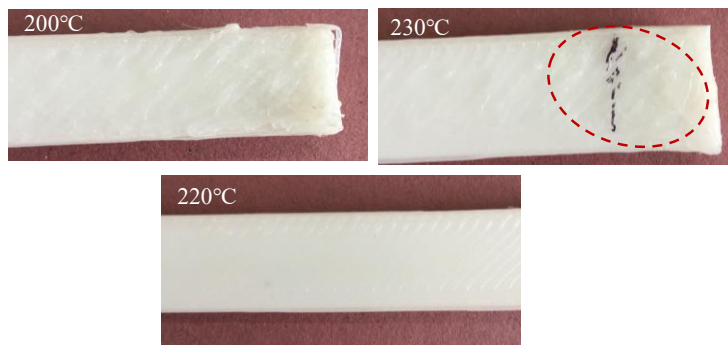
Figure 3.6 Micrograph of printed (a) H in thickness direction and (b) freeze fractured across the thickness.

The sandwich (S) printing all at once (concurrent) is executed by feeding H and H20 - H60 filaments in nozzle 1 (N1) and nozzle 2 (N2), respectively, for fabricating SH20 - SH60 syntactic foam cored sandwiches. The pilot studies (Table 3.3) are carried out to select suitable printing parameters to print SF cored sandwiches concurrently. The SF cored sandwiches of $180 \times 18 \times 8$ mm³ are printed with different nozzle, chamber, bed temperatures, and printing speed to get suitable values. Table 3.3 presents the observations about the experimental tests carried out to identify appropriate printing parameters for core and sandwiches by varying N1 (Figure 3.7a) and N2 (Figure 3.7b) temperature, bed, and chamber temperature (Figure 3.8a) with different printing speeds (Figure 3.8b). Table 3.4 lists the summary of the suitable printing parameters based on the observations of Table 3.3. All samples are printed on HDPE plate at the bed and chamber temperatures of 80 and 60°C respectively, to achieve good adhesion, avoid warpage, and reduce residual thermal stresses. N1 at a

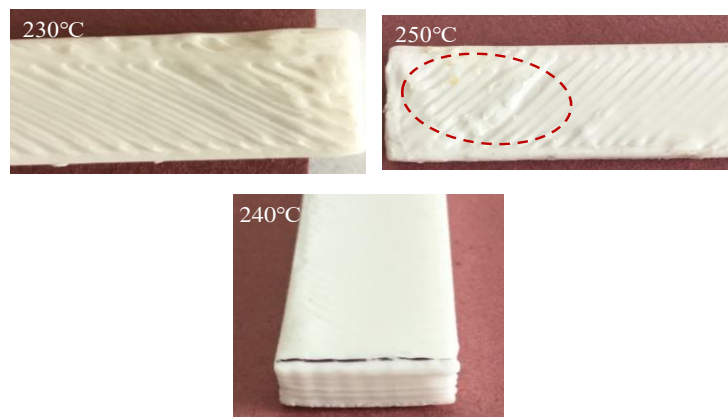
temperature of 220 °C deposits bottom HDPE skin (1 mm) first. Subsequently, the foamed core is deposited for the next 6 mm by N2 at a temperature of 220 °C for H20 and 240 °C for H40 and H60. Finally, again N1 prints HDPE skin having a thickness of 1 mm on top of the earlier printed core. G-codes are generated to follow the N1-N2-N1 sequence to build sandwich composites (SH20, SH40, and SH60) having a total thickness of 8 mm by using simplify 3D tool path. All the core and sandwich samples are printed in a rectilinear pattern having a print orientation in Y-axis. A layer thickness of 0.32 mm is set to provide adequate clearance between the nozzle and the printed part. A printing speed of 30 mm/s is kept constant for all the samples to improve the surface finish and lower the warpage. A multiplier is set to 0.9 for H - H40 and 1.3 for H60, based on the MFI estimations. For up to 60% MFI reduction, layers are deposited without any difficulties with 30 mm/s printing speed. For higher MFI reductions, nozzle blocking is encountered, and hence a multiplier of 1.3 is set for H60 for a given nozzle temperature setting.

Table 3.3 Experimental test observations during 3DP of SF cored sandwiches.

Parameter and range	Typical Value	Observation	Figure No.
Nozzle-1 Temperature °C (200-230)	200	Non-uniform layer deposition	Figure 3.7a
	230	More material flow leading to bulk material deposition at different locations along the sample length	
	220	The material flow is continuous and smooth without any difficulty	
Nozzle-2 Temperature °C (230-250)	230	Improper flow of material and rough surface finish	Figure 3.7b
	250	Material to flow out continuously but with lumped deposition at several locations	
	240	Good print with excellent surface finish	
Bed (60-100) °C and chamber temperature °C (40-80)	60 and 40	Post-printing warpage is observed at ends	Figure 3.8a
	100 and 80	Comparatively less Warpage at ends	
	80 and 60	Samples without any warpage	
Printing Speed mm/s (25 - 35)	25	Small islands formations on the surface	Figure 3.8b
	35	Formation small voids on the surface	
	30	Sample with smooth surface finish	

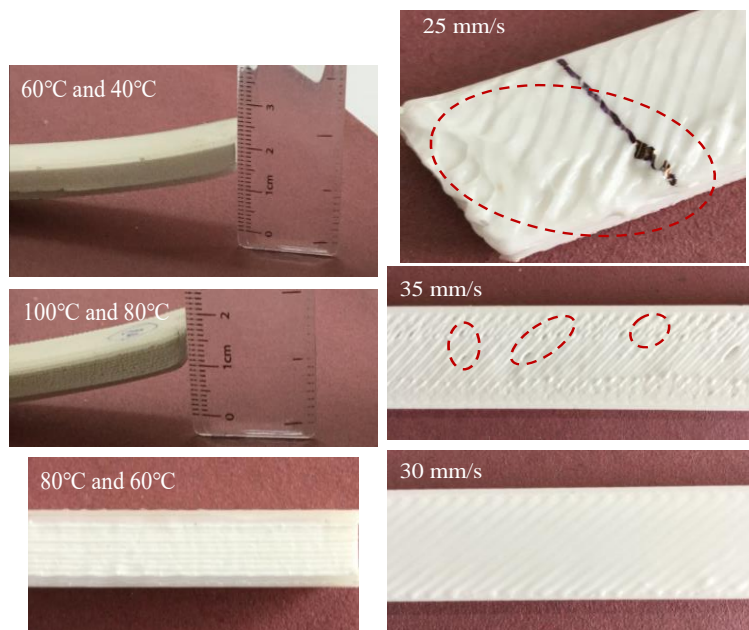


(a)



(b)

Figure 3.7 Prints with different (a) N1 and (b) N2 temperatures.



(a)

(b)

Figure 3.8 Prints with (a) different combination of bed and chamber temperatures and (b) different printing speeds.

Table 3.4 Suitable printing parameters used to print core and sandwich.

Parameters	H	H20	H40	H60	SH20	SH40	SH60
N1 (°C) - HDPE filament	220	-----	-----	-----	220	220	220
N2 (°C) - Foam filaments	-----	220	240	240	220	240	240
Extrusion Multiplier	0.9	0.9	0.9	1.3	0.9	0.9	1.3
Bed temperature (°C)				80			
Chamber temperature (°C)				60			
Printing speed (mm/s)				30			
Layer thickness (mm)				0.32			
Infill percentage (%)				100			
Raster pattern				Rectilinear			
Raster angle				±45°			

Figure 3.9a shows the micrograph of 3D printed H60 that exhibits uniform GMB dispersion along with elongated voids. Such elongated voids at higher filler volume % are the result of lower MFI and reduced melt viscosity. Printed samples have more void content than filaments (Table 3.1) because of air gaps/raster gaps/residual micro-porosities between adjacent raster (Figure 3.9b). Air gaps are increasing with GMB content due to lower matrix phase, higher melt viscosity, and reduced CTE values. Such air gaps might enhance damping and compressive capabilities, as mentioned earlier.

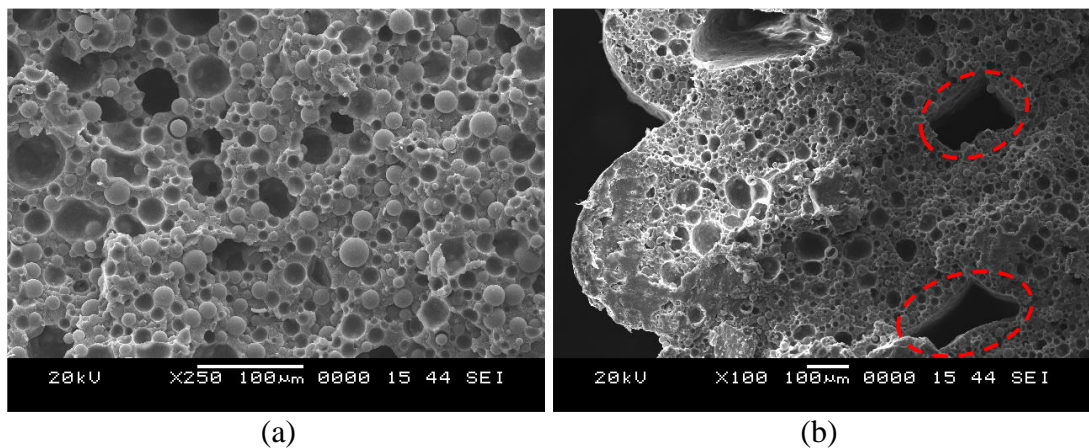
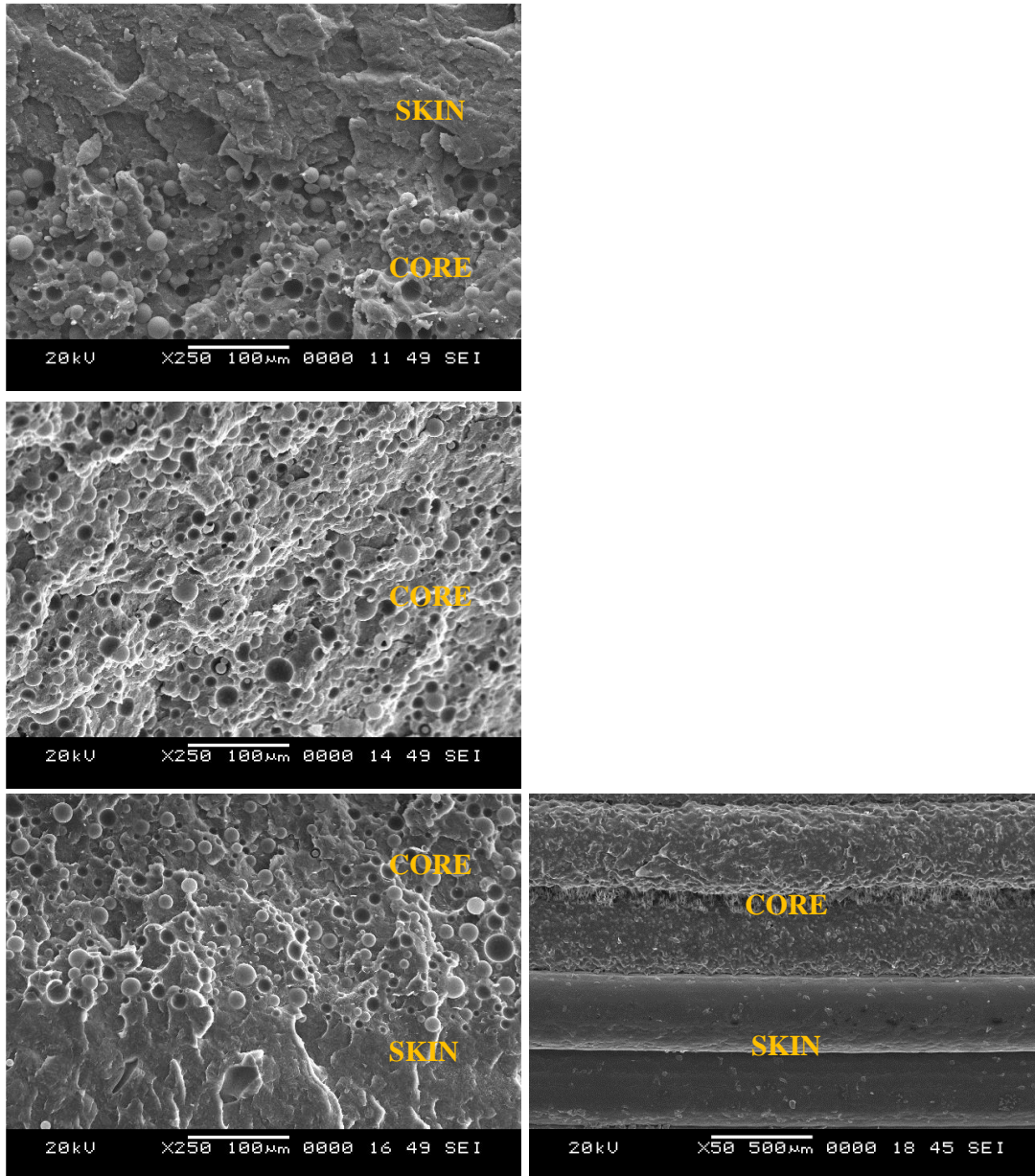


Figure 3.9 Micrograph of printed (a) H60 and (b) associated raster gaps (residual micro-porosity) in H60.

With the chosen printing parameters, SH20-SH60 sandwiches are printed, and a representative micrograph of SH60 print across three different zones from top to

bottom skin is presented in Figure 3.10a. Figure 3.10b shows the micrograph in the thickness direction. Both these micrographs indicate seamlessly diffused layers across and along the prints implying the printing parameters suitability as presented in this work.



(a) (b)
 Figure 3.10 As printed freeze fractured micrograph of sandwich (a) across the thickness and (b) along the thickness.

3.4 DSC investigations of filament and 3D prints

Thermal behavior (T_{Cryst} , T_{Melt} , and CTE) of H - H60 is presented in Table 3.5. DSC plots for H - H60 are shown in Figure 3.11. For pure HDPE, the endothermic peak is observed at 108 °C, which is noted to be in an increasing trend for foams. The decrease in the level of endotherm and crystallization temperature rise with higher GMB content is also indicated in Figure 3.11. This strongly affirms that, while HDPE cools, the nucleation of melt occurs on the filler surface at relatively higher temperatures forming thicker crystal lamellas leading to higher T_{Cryst} (Shaikh et al. 2016). Melt inertia is ignored as the crystallization temperature of foams varies in a very narrow range of 2.2% as compared to H (Table 3.5). An increase in filler volume % has an insignificant influence on T_{Melt} of both filaments and prints, as seen from Table 3.5 indicating i) additional thermal history imposed by 3DP post extrusion has not induced higher residual thermal stresses and ii) printing temperatures can be kept similar for the samples (elaborately discussed in the earlier section). A decrease in α_{Cryst} (56.68%) for foam filaments is observed with increasing GMB content.

Table 3.5 Thermal behaviour of H - H60.

Material	T_{Cryst} (°C)		α_{Cryst} (%)		T_{Melt} (°C)	
	F	Pnt	F	Pnt	F	Pnt
H	105.70	110.82	59.54	61.74	131.47	130.88
H20	112.67	113.12	49.12	50.72	132.51	131.24
H40	112.92	113.23	33.71	37.01	130.45	131.29
H60	112.59	113.27	25.79	28.59	130.86	130.90

Printed samples also show similar behavior where α_{Cryst} dropped from 61.74 (H) to 28.59% (H60). Compared to filaments, the corresponding prints have a higher α_{Cryst} and are anticipated to provide higher dimensional stability and reduces warpage, as mentioned in the earlier section. Extruded filaments are subjected to sort of quenching as it passes through the water bath post extrusion. Thereby, very little time and energy are available for melt crystallization of filaments (Wasiak et al. 1999, Yang et al. 2017) compared to prints wherein samples cool slowly within the printer chamber. Due to the resistance offered by GMB to the flow of polymer chain α_{Cryst} decreases in foams along with the reduction of the crystal domain of H (Panupakorn

et al. 2013, Sewda and Maiti 2010). Hence dimensionally stable foam prints without any warpage can be successfully 3D printed, having a potential weight saving of ~28% (Table 3.1).

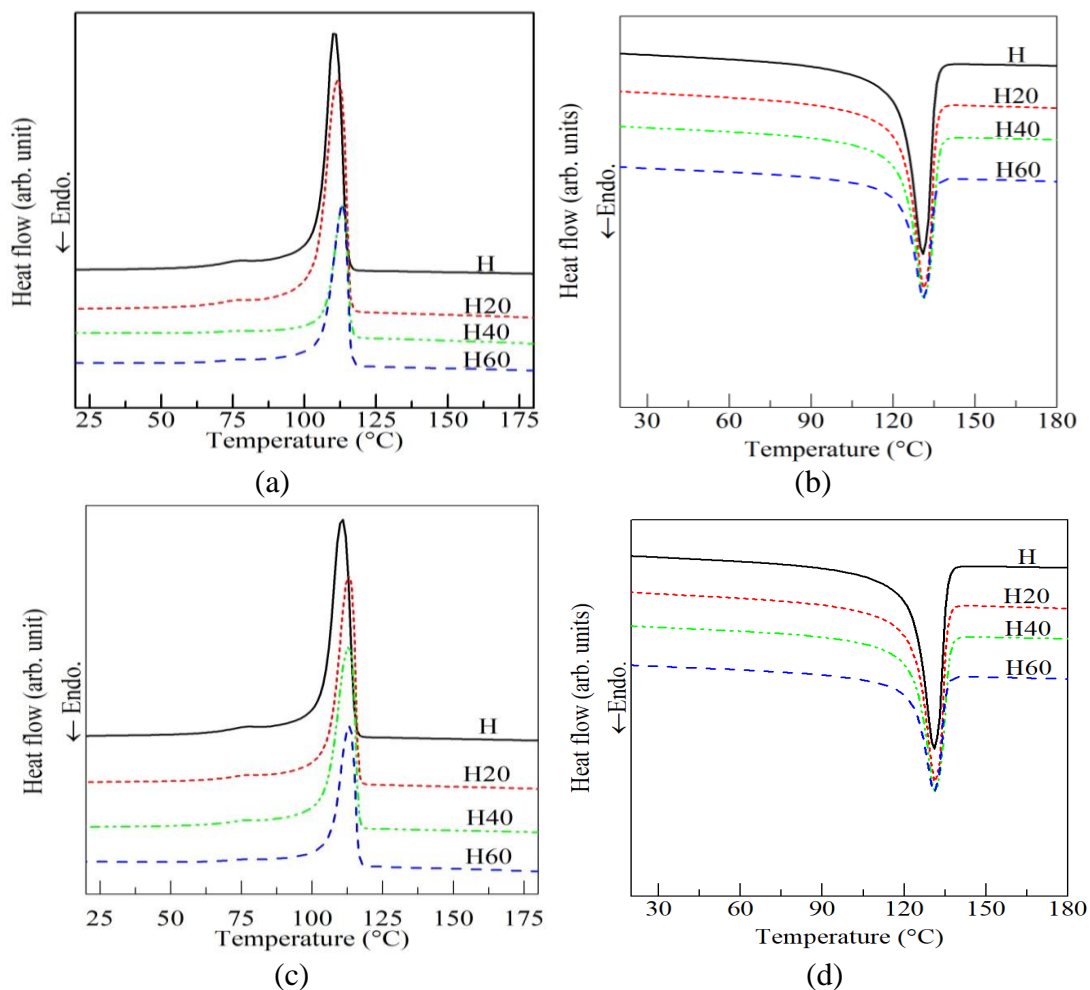


Figure 3.11 DSC for crystallization peaks: Cooling cycle in (a) filaments and (c) prints. Melting peaks from heating cycle (2nd) in (b) filaments and (d) prints.

3.5 CTE of prints

The addition of GMB in the HDPE matrix lowers CTE, as seen from Table 3.6, (Baglari et al. 2011, Shunmugasamy et al. 2012). At higher printing temperatures, dimensional stability can be achieved by adding GMB into HDPE, which is affirmed in the earlier section as substantial warpage reduction is observed in printed components with dimensional stability and lower residual thermal stresses (Baglari et al. 2011). The entrapped gas inside the hollow GMB offers resistance against heat

flow resulting in lower thermal conductivity in addition to the more considerable difference in the CTE values of both GMB and HDPE. Further, CTE also helps in understanding the raster diffusion mechanism and air gap formation in 3DP. As clearly evident from Figure 3.5d, warpage is a crucial and challenging while printing neat HDPE due to higher CTE values. Nonetheless, appropriate printing and bed temperatures have effectively addressed this issue. Dimensionally stable prints are observed in foams due to lower CTE due to lower thermal conductive gases within hollow GMB limiting heat flow (Atagür et al. 2018, Labella et al. 2014). H60 print showed the lowest CTE among foams, leading to minimal raster diffusion, thereby resulting in air gaps (Figure 3.9b). Such air gaps/residual micro-porosities make SFs lighter (~2 - 4%), as evident from Table 3.1.

Table 3.6 CTE of printed samples.

Material	CTE $\times 10^{-6}$ ($^{\circ}\text{C}$)	% reduction w.r.t 'H'
H	135 \pm 3.29	-----
H20	106 \pm 3.85	21.48
H40	88 \pm 2.65	34.81
H60	75 \pm 1.15	44.44

4 TENSILE BEHAVIOR

4.1 Tensile behaviour of HDPE and foam filament

The tensile response is governed by the dispersion of reinforcement, filler size, matrix interaction, and inherent properties of the matrix (Ponnamma et al. 2019). In order to use filament as feedstock material in the 3D printer, it must meet specific requirements like shape retention without excessive bending to absorb frictional forces while going through drive rollers (Lombardi et al. 1997). Bending can be avoided by keeping the filament rigid enough to withstand the push of the drive roller without damaging the associated printer elements. Figure 4.1 presents the tensile stress-strain plots of filaments. Stiffer intact GMB particles increase filament modulus by 8.17, 14.40, and 46.81% in H20, H40, and H60, respectively, compared to H (Table 4.1 and Figure 4.1b). HDPE filament is strained to more than 1000 % without any breakage due to its ductility. However, only up to 400% strain is graphed in Figure 4.1a. H40 and H60 failed within ~25% strain, as seen from Figure 4.1b. H20 exhibits more than 40% strain with the highest UTS of 12.63 MPa among foams. A higher amount of matrix in H20 resists the tensile load effectively by the plastic deformation of the entire cross-section, as observed from Figure 4.1c. The marked area in Figure 4.1c shows the formation of a new surface at the bulk scale, enhancing strain. H60 has the highest void content of 7.7% (Table 3.1) among foams resulting in much earlier filament fracture due to a reduction in the effective area arising from elongated pores coalescence (locations 1 - 4 in Figure 4.1d). Nevertheless, H60 exhibits the highest modulus because of a higher number of intact GMB particles (marked area in Figure 4.1d).

Strength decreases with increasing filler content because of weaker bonding between GMB and HDPE, as seen in Figure 3.4c. Further, with increasing GMB content, HDPE volume decreases, lowering the ductile phase substantially, resulting in lower strength values. Filament strength can be increased by surface treating of GMB particles that lead to enhanced interfacial bonding and is not within the scope of this work. Such a surface treatment approach needs careful attention as coupling agents increase the brittleness and hamper spooling flexibility. The current work focuses on

developing lightweight composite foam filaments for 3DP using as received constituent materials. The processing time and cost are kept minimum, enhancing the industrial adaptability for components where modulus and comparable strength are the design criteria.

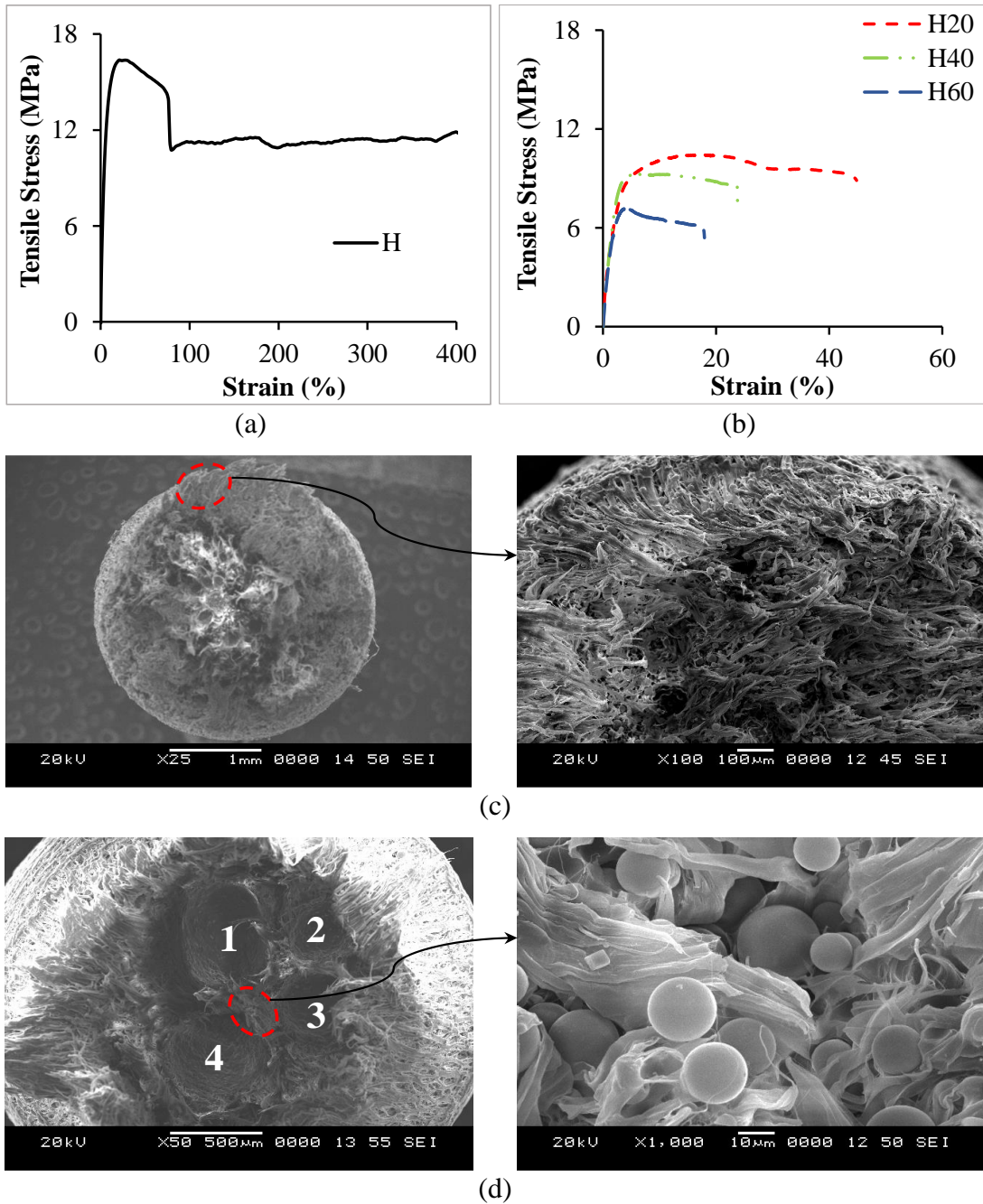


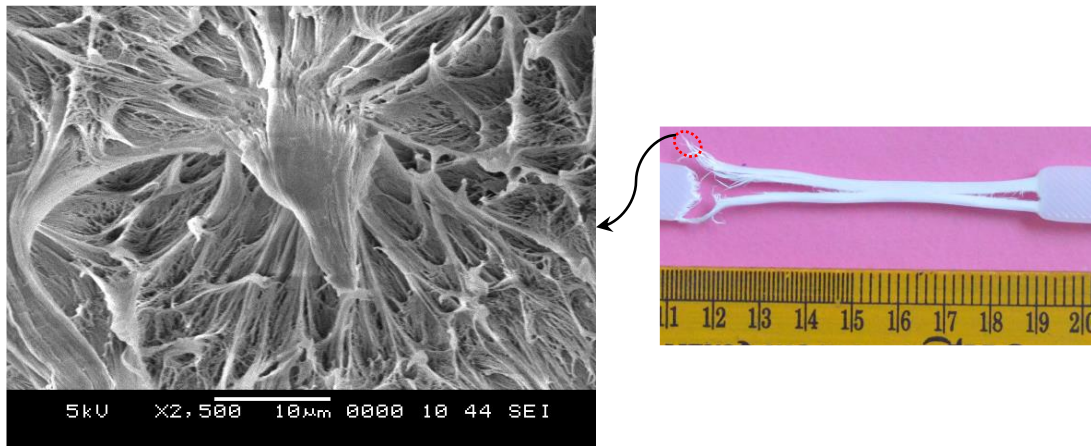
Figure 4.1 Representative filament stress-strain plot of (a) H and (b) H20 - H60. Micrographs of (c) H20 and (d) H60 filament post tensile tests.

4.2 Tensile behaviour of 3D prints

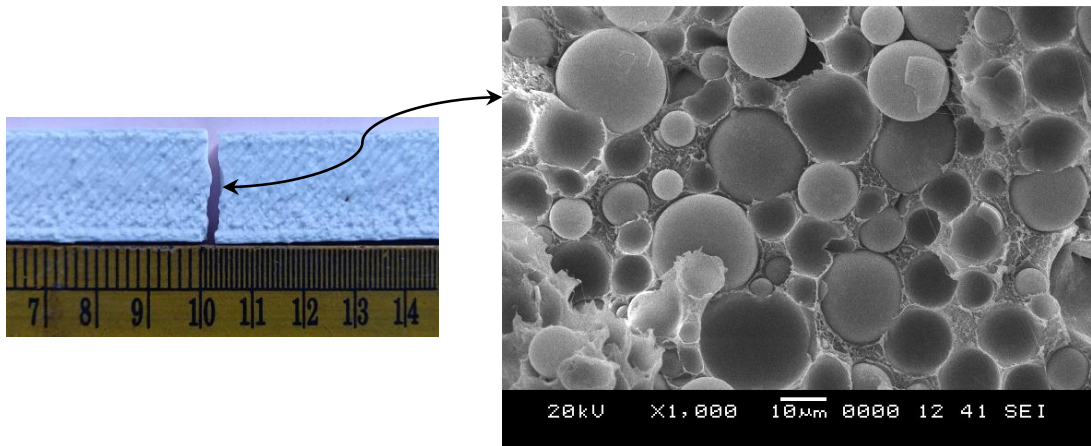
A similar trend of stress-strain response is exhibited by 3D printed H - H60, and the values are listed in Table 4.1. Breakage of pure HDPE filament is not seen even after a strain of up to 1000%, while HDPE print could sustain only up to ~45% strain, indicating a behavioral change from ductile to brittle phase post 3DP. HDPE is extruded twice, once during filament formation and secondly in printer nozzle extruder. Such multiple extrusion cycles result in polymer chain alignment, associated crosslinking due to thermal processing leading to the hardening process. Failure strain for 3D printed H40 and H60 foams are 21.66 and 14.49%, respectively, whereas H20 shows up to 30.48% strain. In HDPE, a long necking region is observed (Figure 4.2a) due to raster fibrillation resulting in broom-like fibrous ends. Such fibrous ends result from new surface formations because of extensive plastic deformation (micrograph of the marked area in Figure 4.2a). H40 and H60 foam prints show no necking region and fracture in a typical brittle manner, which is seen in the fractographic area wherein matrix plastic deformation is hardly seen (Figure 4.2b).

Table 4.1 Tensile properties of filament and 3D prints.

Material	Modulus in MPa		UTS in MPa		Elongation at UTS in %		Fracture strength in MPa		Fracture strain in %	
	F	Pnt	F	Pnt	F	Pnt	F	Pnt	F	Pnt
H	722 ±16.73	810.25 ±16.73	16.4 ±0.22	17.68 ±0.21	17.90 ±0.26	15.04 ±0.23	---	6.68 ±0.11	---	93.00 ±1.03
H20	781 ±17.95	865.56 ±17.79	10.45 ±0.42	12.8 ±0.35	12.63 ±0.33	5.68 ±0.29	8.93 ±0.23	10.39 ±0.29	44.27 ±0.23	30.48 ±0.10
H40	826 ±14.27	1125.68 ±12.41	9.25 ±0.39	9.49 ±0.49	5.27 ±0.35	3.11 ±0.31	7.01 ±0.19	8.24 ±0.25	23.81 ±0.22	21.66 ±0.06
H60	1060 ±18.53	1199.26 ±11.53	7.16 ±0.17	8.45 ±0.18	2.39 ±0.21	4.69 ±0.11	5.90 ±0.14	7.78 ±0.19	16.53 ±0.31	14.49 ±0.07



(a)



(b)

Figure 4.2 Fractographic analysis of representative 3D printed (a) H (Patil et al. 2019) and (b) H60 post tensile test.

All the microballoons are observed to be intact, signifying potential weight saving of ~28% (Table 3.1) is successfully achieved post-printing. Intact GMB particles at higher filler % make matrix responsible for load carrying, which succumbs early owing to induced brittleness post-printing. Comparative analysis between the filament and printed coupons about modulus and strength increased by 12.22, 10.83, 36.28, 13.14%, and 7.8, 22.49, 2.59, 18.02%, respectively. GMB/HDPE prints results are compared with injection molded cenosphere/HDPE foams. 3D printed HDPE shows appreciable UTS with a higher elastic modulus of 53.17% compared with injection molded foams. 3D printed foam elongates at UTS and fractures strength of 47.45% and ~3 times higher than injection molded specimens (Kumar et al. 2016). Modulus of foam increases with GMB % (Table 4.1). Among foams, H60 displays the highest

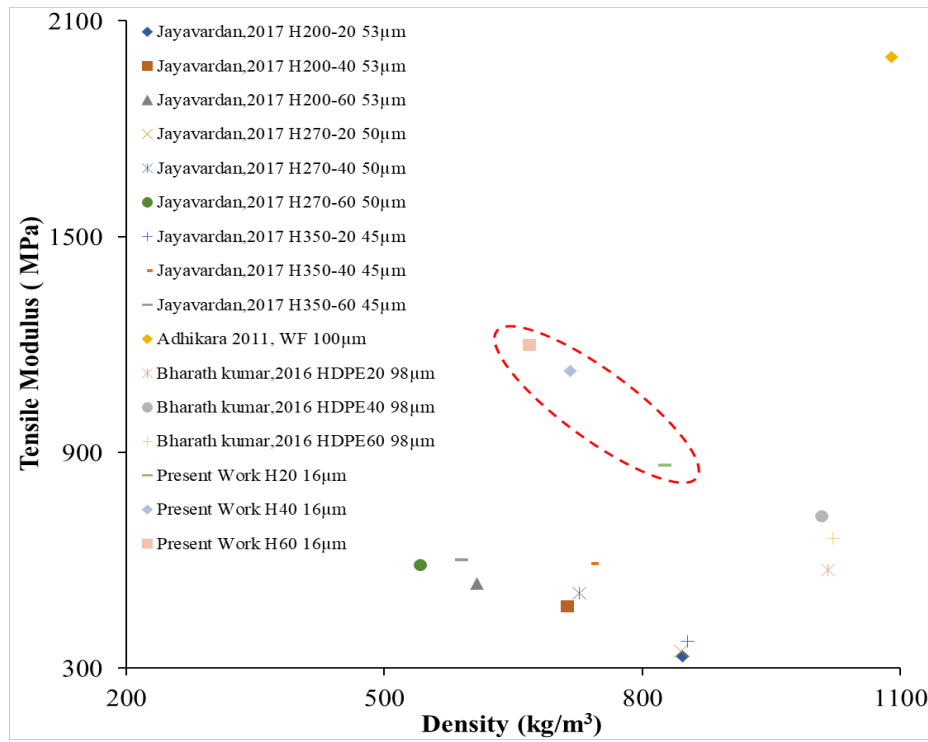
modulus and is 48.02% higher than HDPE print. 3D printed H - H60 registered 1.5 - 1.8 times higher modulus than molded counterparts with zero tooling cost. Foam prints fracture strength is 1.16 - 1.56 times higher when compared with H. For weight-sensitive applications, specific properties of foams are essential since printing allows flexibility in developing integrated (joint less) components with complex designs. Among all foams, H60 and H20 exhibit the highest specific modulus and strength, respectively. Table 4.2 shows the GMB/HDPE weight-saving potential through estimations of E/ρ^n ($n = 1, 2$ and 3). Values in Table 4.2 indicated that 3D printed GMB/HDPE foams can be used effectively in buoyancy modules, automotive and aerospace components of integrated complex designs.

Table 4.2 Weight saving quantification parameters of H - H60.

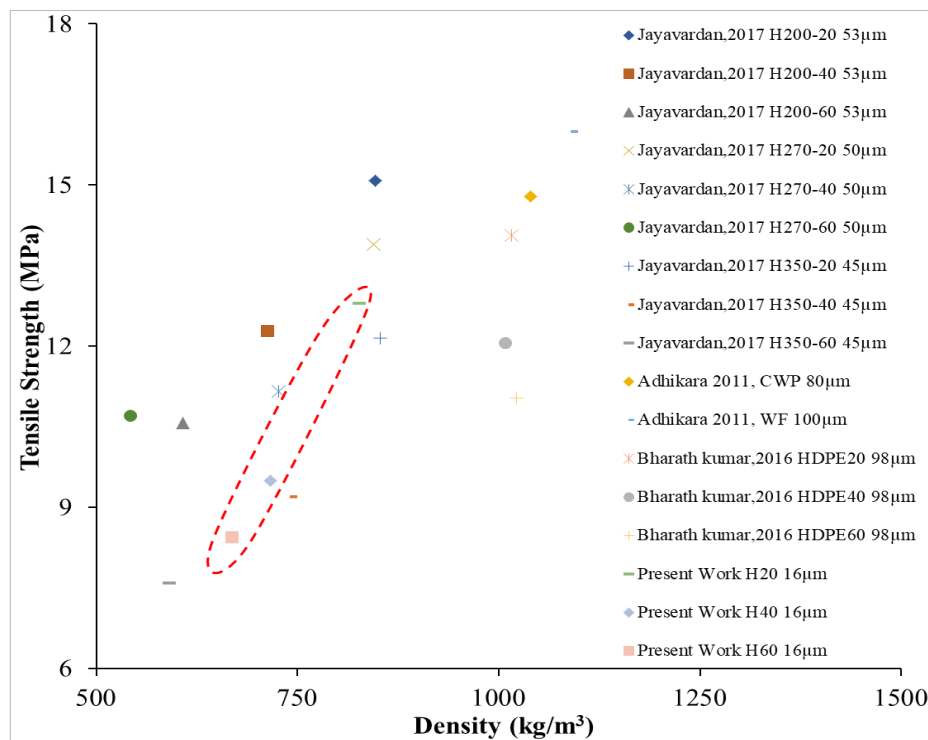
Material	$\frac{E}{\rho}$	$\frac{E}{\rho^2}$	$\frac{E}{\rho^3}$
	MPa/kg/m ³	MPa/(kg/m ³) ² ×10 ⁻³	MPa/(kg/m ³) ³ ×10 ⁻⁶
H	0.87	0.94	1.02
H20	1.05	1.27	1.54
H40	1.51	2.02	2.71
H60	1.80	2.69	4.02

4.3 Property map

Figure 4.3 (Jayavardhan and Doddamani 2018, Jayavardhan et al. 2017, Kumar et al. 2016) shows the tensile response as a function of composite density fabricated using different processing routes. Hollow particle-filled composites exhibit promising properties to be exploited in weight-sensitive applications compared to solid-filled material systems. The density of GMB based 3D printed foams is in between the injection and compression molded foams. The tensile modulus of printed composites outperforms injection and compression molded composites (Figure 4.3a) except wood-filled composites. The strength of GMB based printed foams is comparable to compression and injection molded samples (Figure 4.3b). Choosing suitable extrusion and printing conditions with no particle breakage results in a substantial weight reduction of ~28%, as successfully demonstrated as a path of this work. Such a weight reduction for complex integrated 3D printed components would enhance the performance with reduced carbon footprints.



(a)



(b)

Figure 4.3 Tensile (a) modulus and (b) strength of HDPE composite (Jayavardhan and Doddamani 2018, Jayavardhan et al. 2017, Kumar et al. 2016).

Conclusions

GMB based lightweight composite foam feedstock is successfully synthesized on a commercial printer for weight-sensitive applications. Filaments and 3D printed samples are tested for mechanical characterization to check their adaptability and feasibility for 3DP applications, and a summary of the results are presented below:

GMB/HDPE blends

- An increase in GMB content decreases the MFI of HDPE.
- Loss modulus, storage modulus, and complex viscosity increase with increasing GMB content. At lower frequency, complex viscosity is maximum and decreases as the frequency increases showing shear thinning behaviour in GMB/HDPE blends. Loss and storage modulus showed an increasing trend with an increase in GMB % and frequency.
- Filler content has no significant effect on the peak melting temperature (T_{Melt}) of filaments and prints. The degree of crystallinity (α_{Cryst}) decreases by 56.68 and 53.69 % for foam filaments and prints, respectively, with increasing GMB content as compared to HDPE. Compared to filaments, the corresponding prints have a higher α_{Cryst} and positively signify dimensional stability and warpage-related issues.
- The addition of GMB in HDPE decreases the CTE of prints substantially, making the prints dimensionally more stable.

3D printing

- The syntactic foam cores sandwich is successfully 3D printed at once using suitable printing parameters without defects.
- The micrographs of printed syntactic foam cored sandwich exhibit the seamless, defect-free interface between the skin and core and within the core layers.
- Sandwiches printed at once using the proposed methodology, as presented in this work, avoids the need for adhesive/glue (absence of parent material) used in conventional manufacturing of sandwich composites for assembling core and skin.

- Void contents increase in filaments and prints by 0.84 - 7.70% and 2.42 - 9.73%, respectively, with increasing filler content. 3D printed foams exhibit a 3-phase foam structure.
- 3D printed GMB/HDPE foams having substantial weight saving potential (28%) with superior specific mechanical properties and reduced carbon footprints are successfully realized.

Tensile behavior of filaments and prints

- Stiffer intact GMB particles increase the filament modulus by 8.17 - 46.81% in H20 - H60, respectively, as compared to H.
- Among foams, H60 displays the highest modulus, which is 48.02% higher than HDPE print. 3D printed H - H60 registered 1.5 - 1.8 times higher modulus than molded counterparts. Printed H20 - H60 has 1.16 - 1.56 times higher fracture strength than the printed H.
- A property map illustrates the capabilities of 3D printing in comparison to other processing techniques.

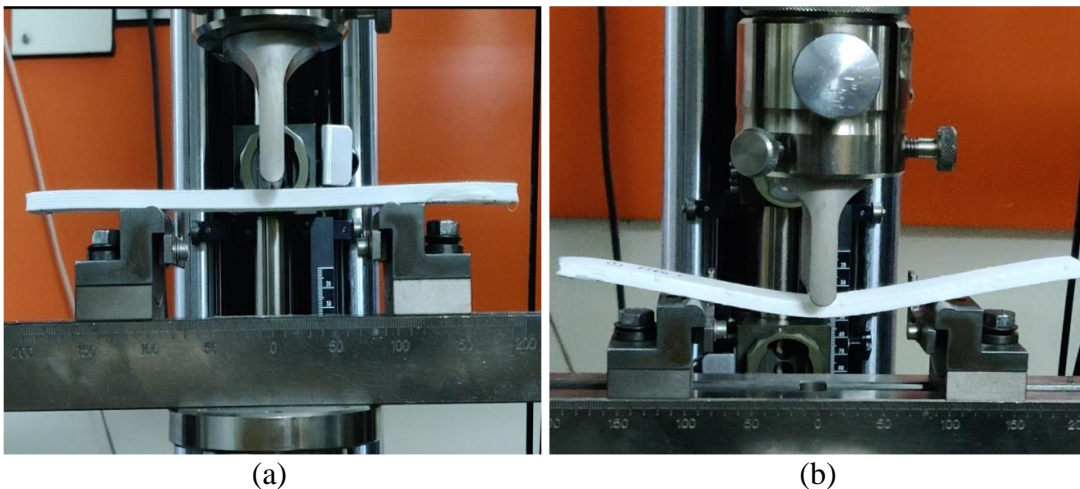
The properties of the produced filaments are equivalent to those of injection-molded specimens, indicating that they have the potential to be employed in 3D printing.

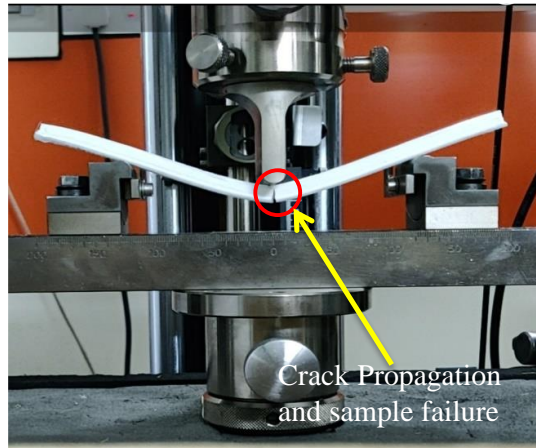
Further, the cost of neat HDPE is reduced by 60 vol. %.

5 FLEXURAL RESPONSE

5.1 Flexural behavior of 3D printed core

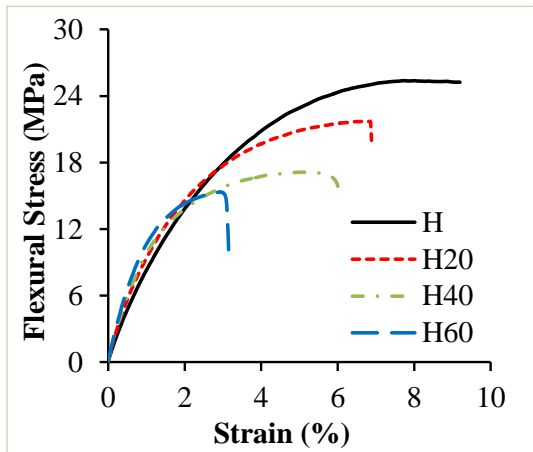
The flexural test is carried out in a three-point bending configuration where samples are mounted, as shown in Figure 5.1a. The printed core starts to yield with the gradual application of load, as evident from Figure 5.1b. Crack initiated from the tensile side and propagated along the loading direction until it meets the compressive side (Figure 5.1c). This is a typical flexural failure mode. Interestingly, the crack did not propagate along with the deposited layers, confirming again the suitable printing parameters chosen for printing (Table 3.4). Foams displayed brittle fracture compared to H, which did not fail until 10% strain (Figure 5.2a). Brittleness is due to the inclusion of GMB in HDPE. An increase in GMB content increases flexural modulus, as clearly seen from Figure 5.2b. The values are tabulated in Table 5.1. The flexural strength is observed to be decreased (Figure 5.2c) due to poor interface bonding between constituent elements and the presence of rasters gaps (Figure 5.2d). HDPE has the highest strength compared to foam samples, which is 1.20, 1.48, and 1.68 times higher than H20, H40, and H60 foams strength. It is observed that the modulus of H60 is enhanced by 1.37 times compared to H, which is due to intact GMB particles even at the highest filler loading (Figure 5.3c). The extensive plastic deformation is seen at lower filler contents (Figure 5.3a and Figure 5.3b) as against H60 (Figure 5.3c).



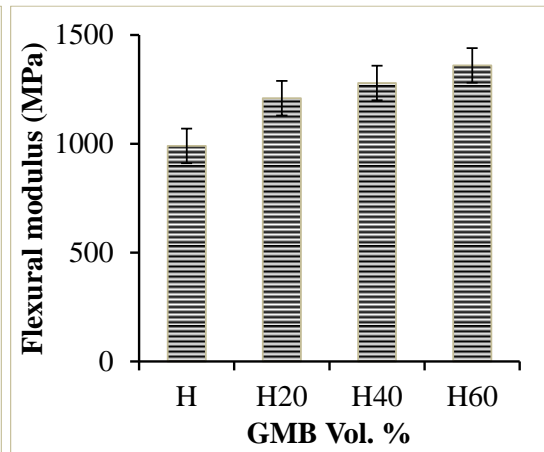


(c)

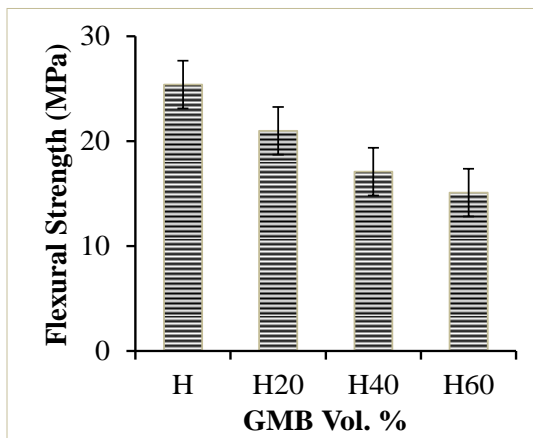
Figure 5.1 (a) Representative H60 mounting in flexure mode (b) yielding (c) and crack initiation.



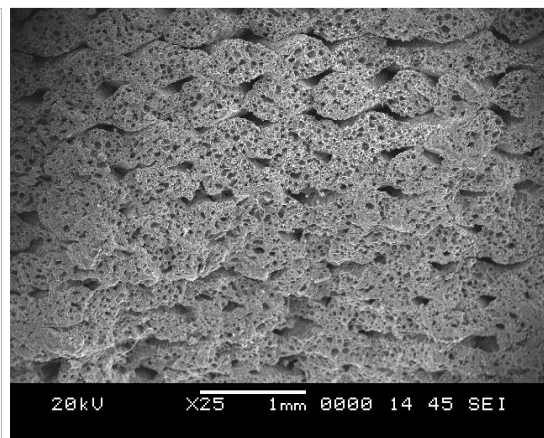
(a)



(b)



(c)



(d)

Figure 5.2 Representative (a) stress-strain plots for prints (b) flexural modulus (c) flexural strength as function of GMB % and (d) H60 micrograph showing raster gaps.

Table 5.1 Flexural Response of H - H60 Prints.

Material	Modulus in MPa	Strength in MPa	Fracture strength in MPa	Fracture strain %	Specific modulus in MPa/kg/m ³	Specific strength in MPa/kg/m ³ ×10 ⁻³
H	990 ±11.28	25.4 ±0.12	---	---	1.068	27.40
H20	1210 ±19.56	21.0 ±0.58	20.34 ±0.32	6.88 ±0.09	1.465	25.42
H40	1280 ±11.87	17.1 ±0.47	16.89 ±0.41	6.04 ±0.11	1.716	22.92
H60	1360 ±11.23	15.1 ±0.72	15.00 ±0.79	3.15 ±0.07	2.036	22.60

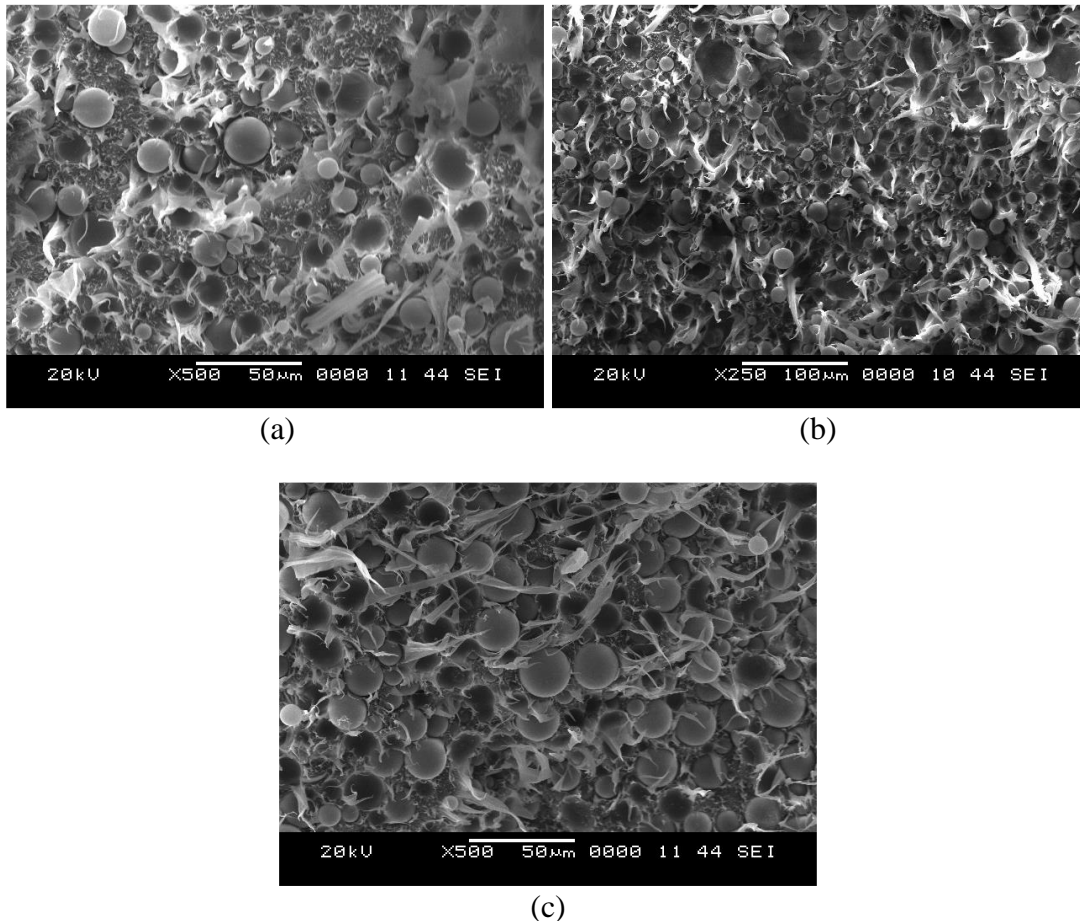


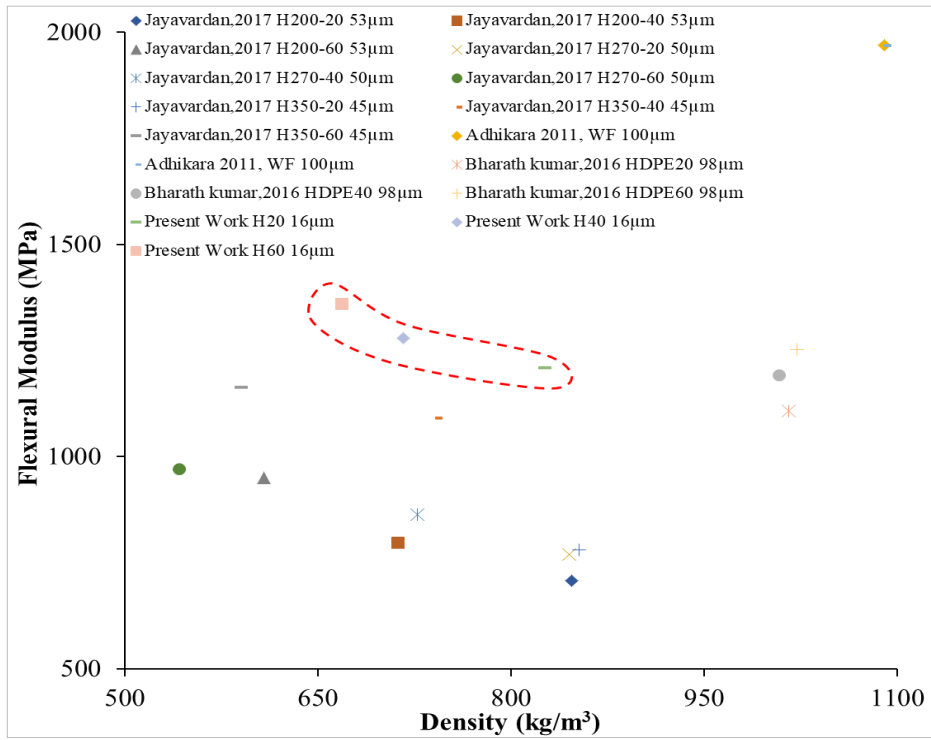
Figure 5.3 Micrographs of post flexure tested (a) H20 (b) H40 and (c) H60 printed cores.

GMBs embedded in the HDPE matrix increase the specific modulus by ~2 times compared to H (Table 5.1). Modulus of H - H60 printed foams is higher by 1.39 -

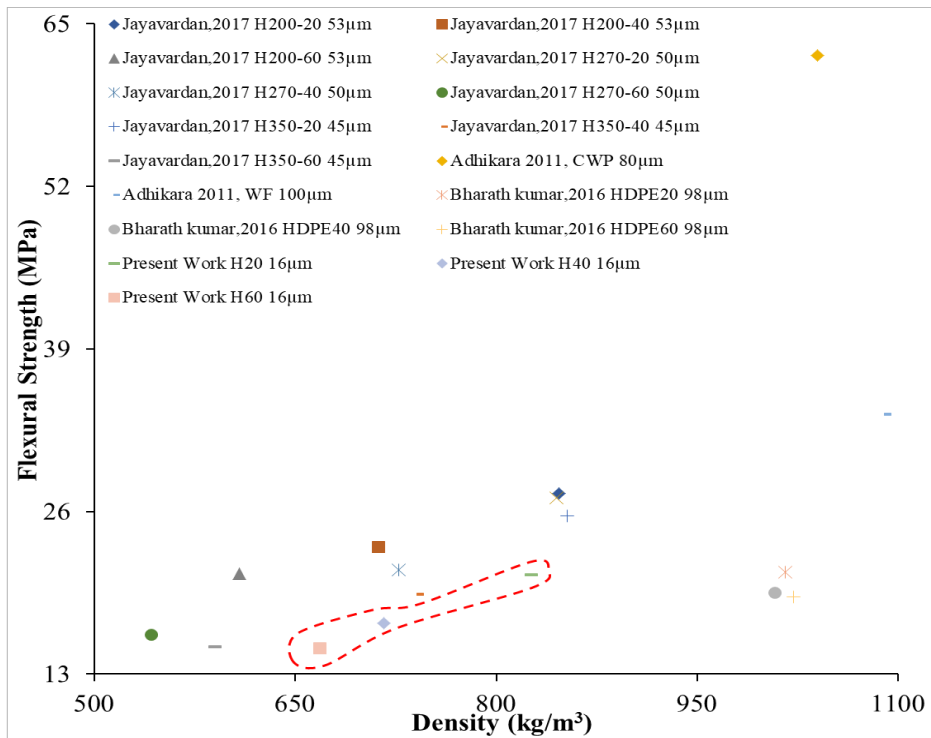
1.08 times against molded counterparts, whereas strength is observed higher and comparable in H and H20 foams. Drop-in strength by 1.14 and 1.27 is noted for printed H40 and H60 respectively against fully dense molded samples and is obvious owing to higher matrix porosity resulting from raster gaps (Bharath Kumar et al. 2016). With increasing filler loadings, these raster gaps volume increases due to lower CTE values. Nevertheless, these gaps can be minimized by overlapping layers and will be explored in future investigations. The flexural strength is observed to decrease as constituent materials are used in the received condition, as mentioned earlier. Furthermore, filler addition increases amorphous fraction leading to more restrained matrix flow and polymer chain mobility resulting in weaker interfaces. Enhancing the bonding between the constituents through appropriate coupling agents might increase the strength but at the expense of a substantial reduction in ductility, which may hamper filament extrusion and the 3DP process.

5.1.1 Property map

Figure 5.4 (Jayavardhan and Doddamani 2018, Jayavardhan et al. 2017, Kumar et al. 2016) shows the flexural response as a function of composite density fabricated using different processing routes. The density of GMB based 3D printed foams is in between the injection and compression molded foams. The flexural modulus of GMB based 3D printed composites is greater than other syntactic foams realized by conventional manufacturing processes (Figure 5.4a). Flexural strength is comparable to composites produced from compression and injection molding (Figure 5.4b). Density reduction can be achieved by selecting optimal extrusion and printing parameters with little filler breakage. Flexural response can be exploited across a wide range by manipulating filler % and parameters of printing, as shown in Figure 5.4.



(a)



(b)

Figure 5.4 Flexural (a) modulus and (b) strength of HDPE composite (Jayavardhan and Doddamani 2018, Jayavardhan et al. 2017, Kumar et al. 2016).

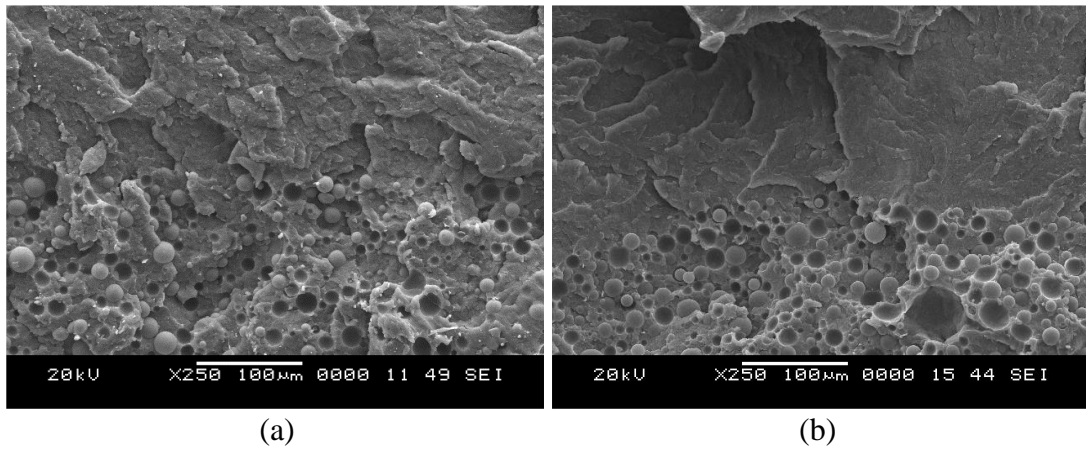
5.2 Flexural behavior of 3D printed sandwich

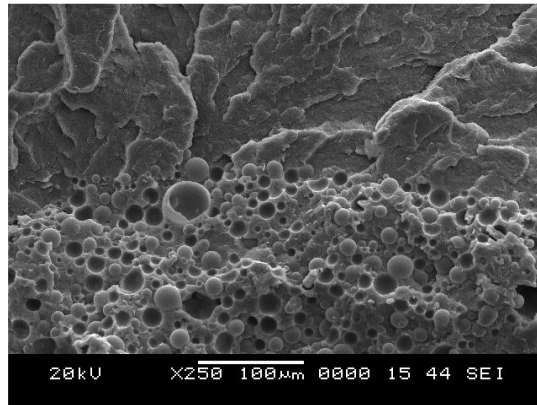
The physical properties of the concurrently 3D printed sandwich are listed in Table 5.2. It is observed that the density of the sandwich decreases as GMB content increases. SH20-SH60 densities are higher (6.45 - 8.36%) than the H20 - H60 counterparts and are expected due to the additional HDPE skin on the foam cores. The maximum weight-saving potential is noted to be ~22% in SH60. Such a weight-saving potential indicates that the developed syntactic foam cored concurrently printed sandwich can potentially replace a few of the components in buoyancy modules, having enhanced specific mechanical properties with integrated (without any joint) complex geometrical features.

Table 5.2 Physical properties of the printed sandwiches.

Material	Φ_f (vol. %)	ρ^{th} (kg/m ³)	ρ^{exp} (kg/m ³)	Φ_V (%)	% Weight saving w.r.t H
SH20	20	879.35±14	897.5	2.02	5.14
SH40	40	777.38±16	845	8.00	16.14
SH60	60	723.87±11	792.5	8.66	21.91

The printed syntactic foam cored sandwich flexural prints are freeze fractured, and the micrographs are presented in Figure 5.5. The seamless bonding at the skin-core interface in all the representative printed sandwiches is visible from these micrographs, implying the printing parameters suitability.





(c)

Figure 5.5 Freeze fractured micrographs of (a) SH20 (b) SH40 and (c) SH60 at skin-core interface.

In the bending test of sandwich samples, the stress varies across the sample thickness from compression (top skin where the loading wedge touches the specimen) to the tensile (bottom skin) side. Additionally, the shearing stress act along the specimen length predominantly in conventionally manufactured sandwich composites leading to skin-core debonding and subsequent failure. Therefore, locations of crack origin and directions of propagation helps in determining the types of stresses causing failure. Figure 5.6 presents the yielding and maximum mid-point deflection of representative SH20. SH20 did not fail until 10 % strain and, as anticipated, registered the highest strength compared to other sandwiches. SH40 and SH60 showed a brittle fracture (Figure 5.7a). In sandwich composites, the crack is initiated in the bottom HDPE skin and later propagated along with the core, just below the loading point. Failure begins at the tensile side, just below the loading point, and develops toward the compressive side. For all the 3D printed syntactic foam core sandwiches, slimier failure features are observed owing to the suitable printing parameters used, avoiding shear crack/failure along with the printed layers. The modulus increases with GMB content (Table 5.3 and Figure 5.7b). SH60 showed the highest modulus compared to other sandwich compositions. Intact GMBs at higher filler loading, as clearly evident from Figure 5.8b, enhances the moduli of SH60. With increasing GMB content in the core, flexural strength decreases, as seen from Figure 5.7c. SH20 and SH40 failed completely in two pieces exhibiting the typical brittle fracture. SH20 is the best in strength, which might be due to effective load

transfer between the constituents. This observation is based on the absence of plastic deformation of HDPE, as seen in Figure 5.8a. The excessive plastic deformation of the matrix at higher filler loading makes SH60 perform lower than SH20.

Nonetheless, the specific strength of SH60 is 1.1 times higher than that of SH20. In SH40 and SH60, the crack has initiated near the mid-span, propagated vertically across the thickness of the core, and reaches the upper HDPE skin. The top skin's progressive failure lowers the drop rate in stress and provides extra strain before failure. The interfacial failure is a common thing in shear stress that influenced sandwich composites. Nevertheless, in the concurrently printed syntactic foam core sandwiches presented in this work, none exhibited interfacial separation between core and skin due to perfect and seamless bonding (Figure 5.5).

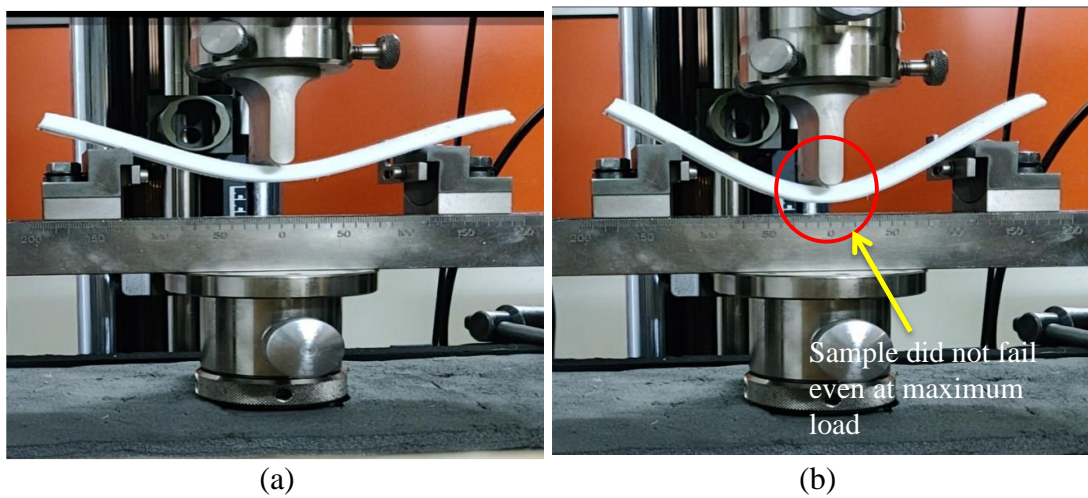


Figure 5.6 Flexural test of representative SH20 (a) yielding and (b) maximum mid-point deflection.

Table 5.3 Flexural response of sandwich prints.

Materials	Experimental Modulus in MPa	Theoretical Modulus in MPa	Strength in MPa	Fracture Strength in MPa	Fracture strain (%)
SH20	927±18.46	1067.83	21.80±0.45	-----	-----
SH40	1000±13.58	1126.09	20.53±0.52	20.25±0.57	7.13±0.15
SH60	1050±12.86	1186.57	19.72±0.80	19.72±0.77	5.20±0.10

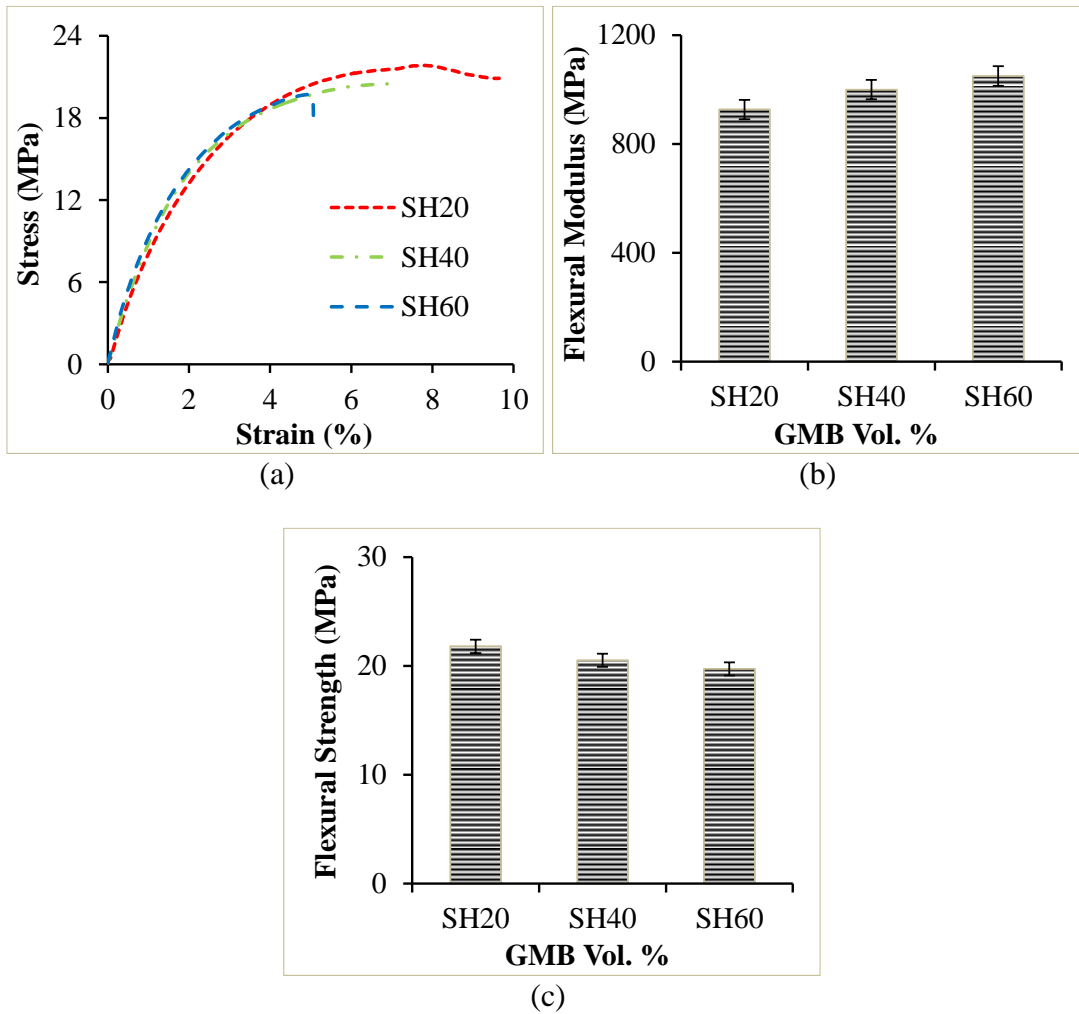


Figure 5.7 (a) Stress - strain plots (b) Modulus and (c) strength as function of GMB content in printed sandwiches.

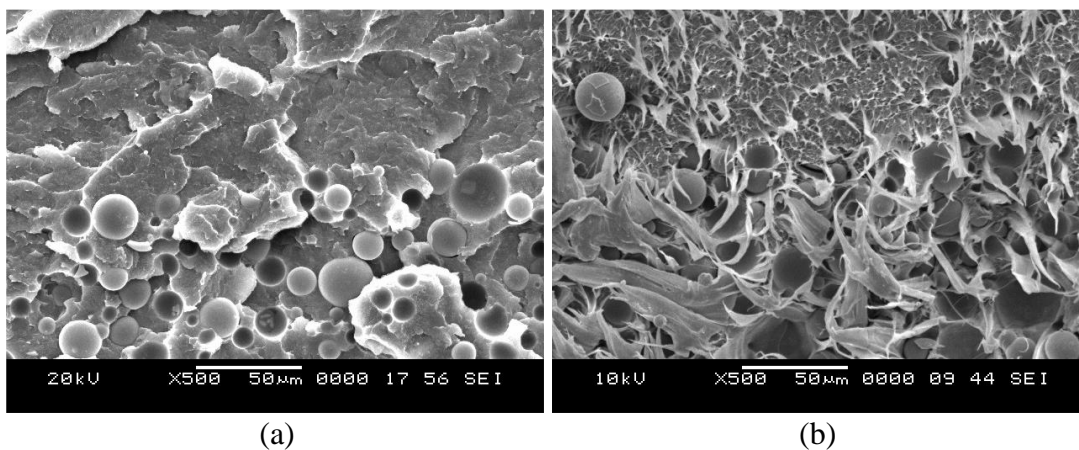


Figure 5.8 SEM of post flexure tested representative (a) SH20 and (b) SH60.

5.2.1 Comparison of core and sandwich flexural properties

The measured flexural properties of 3D printed sandwich composites are compared with respective cores. Figure 5.9 presents a flexural property comparison between printed core and respective sandwiches. Though strength is decreasing with GMBs addition, specific flexural strength increases and is a crucial factor in weight-sensitive structural applications. The flexural strength of SH20, SH40, and SH60 is 1.05, 1.22, 1.35 times higher than their respective H20, H40, and H60 cores, indicating the potential benefit of realizing all at once 3D printed syntactic foam cored sandwich. The flexural strength of 3D printed sandwich composites is 1.04, 1.17, 1.18 times higher than 3D printed cenospheres based cores (Patil et al. 2019). Based on the experimental investigations in this study, SH60 has the highest specific modulus and strength values, which can be exploited for potential weight applications without compromising the mechanical properties.

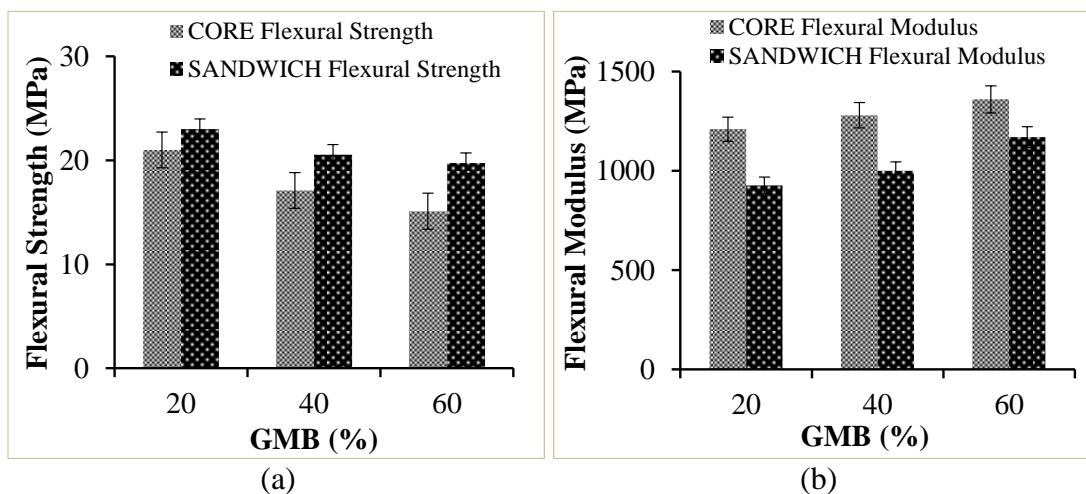


Figure 5.9 Flexural (a) strength and (b) modulus comparison for printed Core and Sandwich.

5.2.2 Theoretical prediction of sandwich properties

The mechanics of composite beam theory (Ugural and Fenster 2003) are used for theoretical calculations. This theory assumes homogeneity in core and face-sheets. Figure 5.10a illustrates a sandwich beam of span length L , width b , and the total thickness of h . The specimen is over-hanged by two rollers of the radius R separated by a distance L , and the load P is applied on the top through anvil of the radius R .

Theoretical values of modulus and failure load of the printed syntactic foam cored sandwiches are estimated using properties of the skin and core evaluated individually using an experimental approach. The terminologies used for theoretical predictions and comparative load-deflection plots for printed sandwiches are presented in Figure 5.10b.

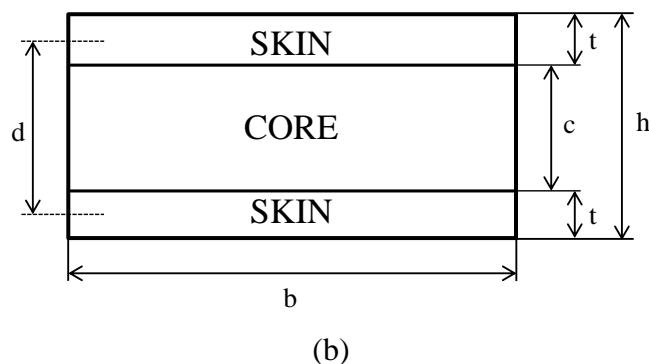
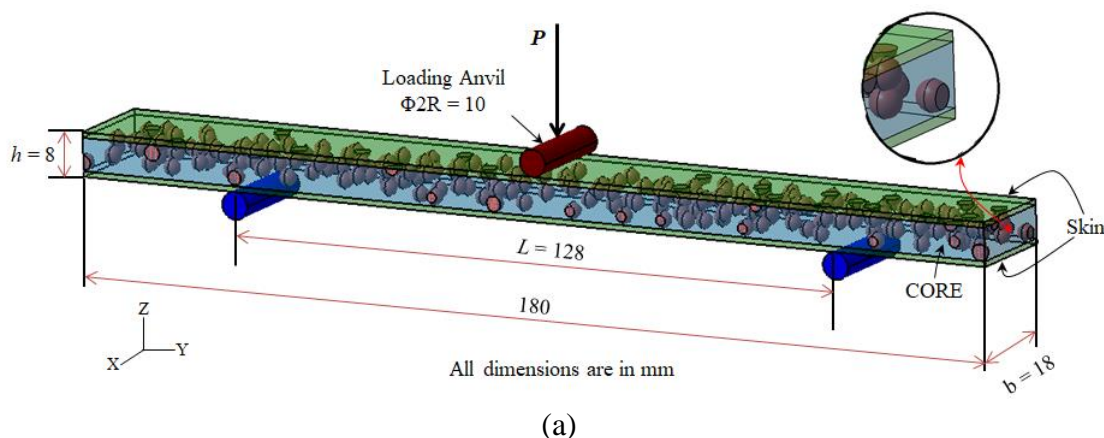


Figure 5.10 (a) Print dimensions and flexural test configuration (b) Schematic representation of sandwich with the terminologies.

In flexure loading conditions, the load is applied gradually at the center and, the deflection includes deformation of both the skin and core. The mechanical properties of top skin degrade in multi-axial stress presence when the wedge comes directly in contact with top skin. Therefore the thickness of top skin where the load is applied is neglected in theoretical calculations of deflection (Budiansky and Fleck 1993, Manalo et al. 2010). This deflection can be calculated using Equation 5.1 (Omar et al. 2015). The effectiveness of skin-core bonding on the properties of the 3D printed

sandwich structure can be estimated by the theoretical modulus of the sandwich, which is calculated using the rule of mixtures (Equation 5.5). The overall deflection at the mid-point is the sum of the deflections due to the bending of the face sheets and core shear (Allen 1969) and is expressed as,

$$\delta = \frac{PL^3}{48(EI)_{eq}} + \frac{PL}{4(AG)_{eq}} \quad (5.1)$$

Here EI_{eq} is called flexural rigidity, which is estimated using Equation 5.2 and $(AG)_{eq}$ is shear rigidity calculated using Equation 5.3. The Shear modulus of the core is (G_c) computed using Equation 5.4.

$$EI_{eq} = \frac{bt^3E_s}{12} + \frac{btd^2E_s}{4} + \frac{bc^3E_c}{12} \quad (5.2)$$

$$AG_{eq} = \frac{bd^2G_c}{c} \quad (5.3)$$

$$G_c = \frac{E_c}{2(1+\mu)} \quad (5.4)$$

$$E = E_sV_s + E_cV_c \quad (5.5)$$

The skin and core moduli are extracted from Table 4.1. Table 5.3 lists experimental and theoretical flexural modulus values which are observed to be in good agreement (Figure 5.11a). The deviations between the theoretical and experimental modulus results for SH20, SH40, and SH60 are 13.18, 11.19, and 11.50 %. These deviations are attributed to void contents in the printed sandwiches. In addition to sandwich stiffness, strength also plays a crucial role. Estimating the critical load attained for a sandwich after the elastic region requires understanding the failure mechanisms discussed in the later section. The failure load evaluation of the sandwich depends on the neutral axis (Equation 5.6) and the total moment of inertia (Equation 5.7), and the moment of resistance (Equation 5.8). As the loading condition in the three-point

bending is supported, the moment at the center is considered, and by using Equation 5.9, the critical load is evaluated.

$$Y = \frac{(A_s E_s Y_s) + A_c E_c Y_c}{(A_s E_s) + (A_c E_c)} \quad (5.6)$$

$$I_t = \frac{(E_c I_c + E_s I_s)}{E_c} \quad (5.7)$$

$$\sigma_{fmax} = \frac{nMY_{max}}{I_t} \quad (5.8)$$

$$M = \frac{P}{2} \times \frac{L}{2} \quad (5.9)$$

Table 5.4 presents the theoretical and experimental critical load estimations for printed sandwiches and is noted to be decreasing with higher GMB volume %. This is due to higher void contents at higher filler loadings. These voids may form three-phase SF morphology and help in enhancing the damping property. The deviation between the experimental and theoretical loads is noted to be in very good agreement, up to half of the maximum load (Figure 5.11b). Such theoretical approaches help predict the sandwich properties, which decides a broad range of possible applications. The load-deflection curve for experimental and theoretical predictions is represented in Figure 5.11c.

Table 5.4 Experimental and theoretical critical load estimations.

Material	Experimental Critical load (N)	Theoretical Critical load (N) from Equation 5-9	Deviation (%)
SH20	135	138.67	2.64
SH40	133	138.57	4.01
SH60	118	135.60	12.97

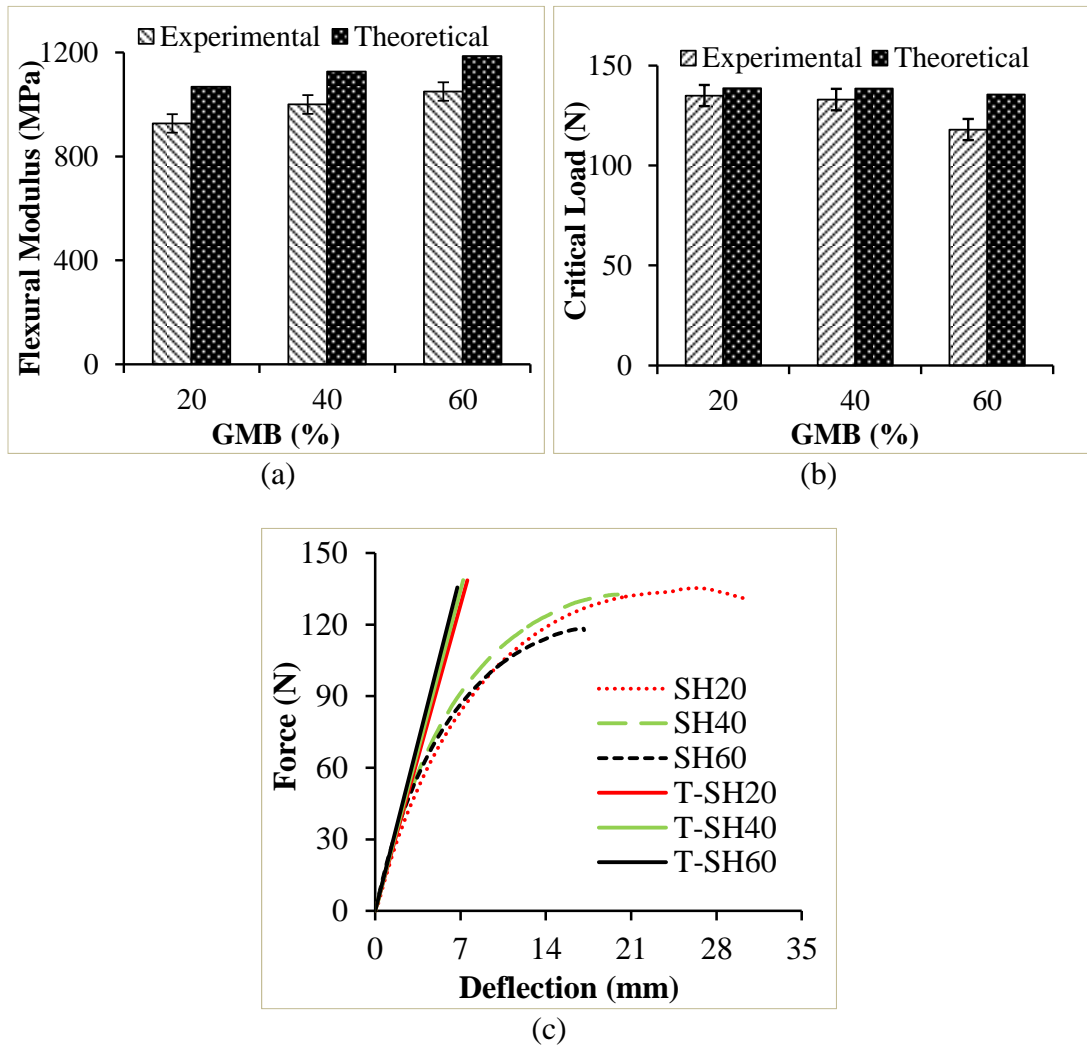


Figure 5.11 Sandwich experimental and theoretical comparison of (a) flexural modulus (b) critical load and (d) force–deflection plots. Note: T denotes “theoretical”.

5.2.3 Failure mode of 3D printed sandwich

The type of sandwich failure strongly depends on skin geometry, strength, and core material (Ashby et al. 2002, Gibson and Ashby 1999). The three possible failure modes in sandwich composites under flexure are indentation, shear, and micro buckling/face wrinkling. The sandwich faceplates remain elastic during core indentation and shear failures (Steeves and Fleck 2004). Indentation creeps in when compressive yield strength matches with stresses developed through the thickness of the core, as seen in Figure 5.12a. The plastic indentation zone (λ_p - core reactive force equals core compressive strength) and elastic indentation zone (λ_e - reactive force equals k_w) form the total indentation region. In the case of shear failure, radial

shear strain in the core exceeds failure strain. In earlier efforts, faceplates contribution is ignored (Allen 1969, Plantema 1966) while circumferential hinges work is accounted for their consideration (Ashby et al. 2002). The bottom skin fails first as it is subjected to tension while micro buckling/face wrinkling surfaces on the top skin (compressive side). Sandwich structures with ductile skins failed in the bottom skin, while those with the brittle ones failed with micro-buckling in the top skin (Triantafillou and Gibson 1987). Generally, when the load is applied to the sandwich structure, the skin undergoes tensile/compressive failure, whereas the core undergoes shear failure. The shear is not observed for all the tested sandwiches. A linear indentation is observed at the point where the wedge directly comes in contact with top skin, and when the load gradually increases, compressive stresses are induced on the top skin resulting in wrinkling at the center for SH20 (Figure 5.12c). In the present work, the indentation failure is observed in SH40 and SH60 samples, as seen from the representative image in Figure 5.12d. None of the samples failed in shear. All the samples except SH20 fractured just below the loading point in an approximately straight line (Figure 5.12d). The indentation is located in the marked area of Figure 5.12d on the fractured surface of the top skin. Also, crack initiation at the bottom skin, and shear failure of the core is observed in SH40 and SH60 due to a higher amount of stiffer GMBs inclusion leading to brittle behavior. Similar failure features, except for shear, are observed for the printed sandwiches developed in the present work (Lingaiah and Suryanarayana 1991, Omar et al. 2015, Theotokoglou 1996, Triantafillou and Gibson 1987, 1987).

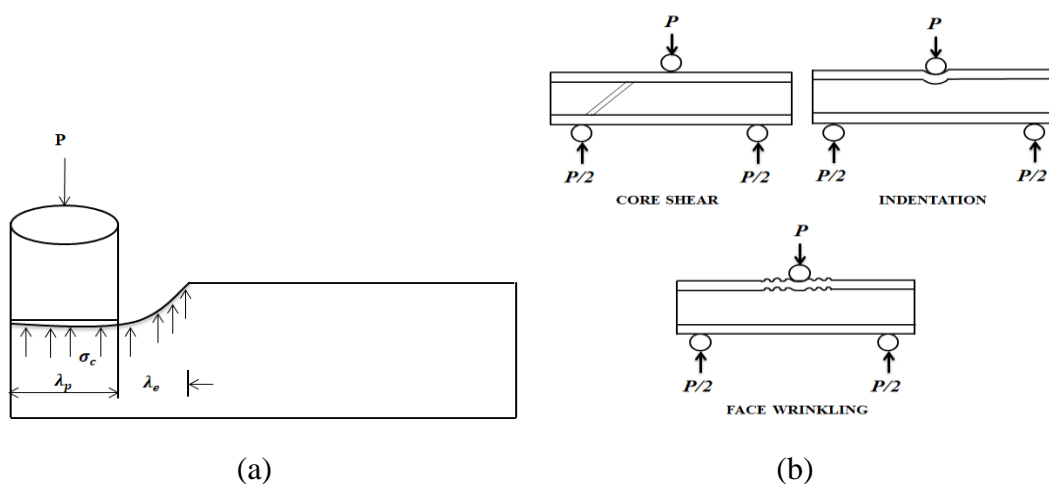




Figure 5.12 Schematic representation of (a) core indentation and (b) failure modes observed in 3D printed SF core sandwiches (c) face wrinkling in SH20 and (d) indentation failure (SH40 and SH60).

Conclusions

- The flexural modulus of H - H60 printed foams is higher by 1.39 - 1.08 times against molded counterparts. In contrast, strength is observed to be higher and comparable in H and H20 foams, respectively.
- GMBs embedded in the HDPE matrix increase the specific flexural modulus by ~2 times compared to H.
- The measured density of all at once 3D printed syntactic foam sandwiches is lower than HDPE, signifying the weight-saving potential. The printed SH60 has a weight-saving potential of ~22%.
- Void % increases with GMB loading, and it ranges from 2.02 to 8.66 % for SH20-SH60. These voids in the core enhance energy absorbing capabilities and make them three-phase SFs.
- The experimental flexural modulus is found to increase with an increase in GMB content. SH60 sandwich exhibits the highest specific modulus of 1050 ± 12.86 MPa and is 6.06 % higher than neat HDPE.

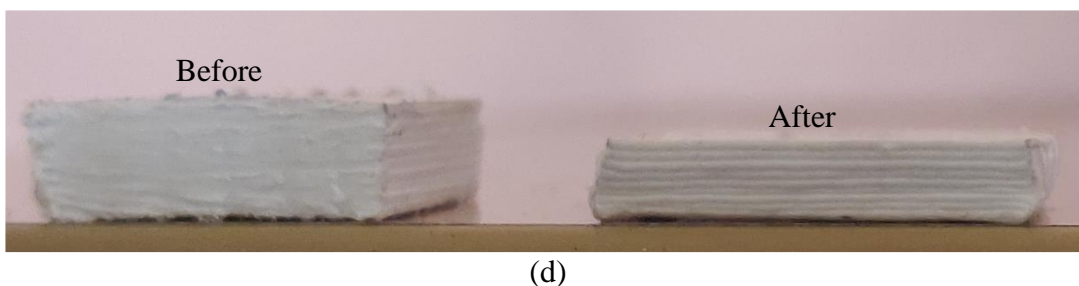
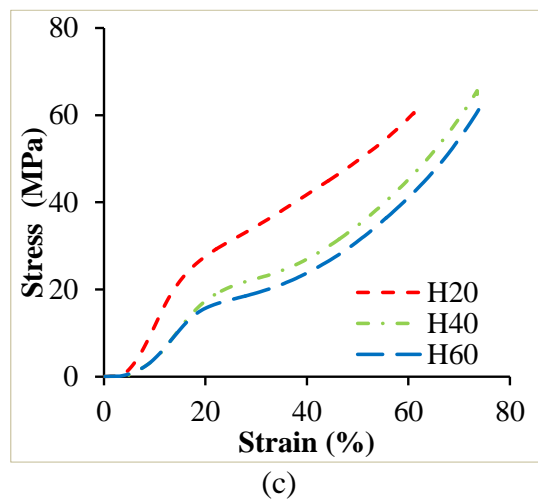
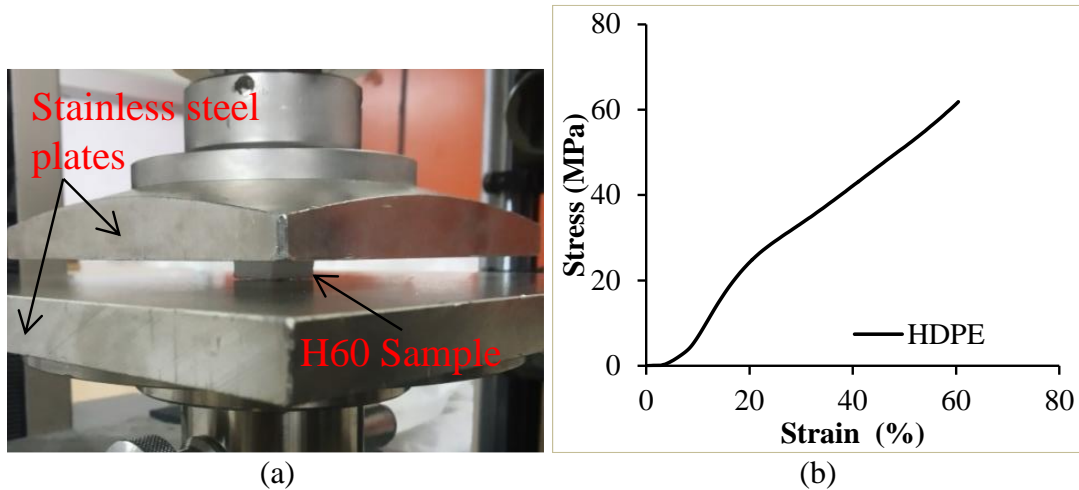
- The 3D printed sandwich has superior strength and is in the range of 1.05 - 1.35 times compared to their respective foam cores.
- SH20 did not fracture even at 10 % strain, whereas SH40 and SH60 fractured due to their brittle nature and increased GMB content. The shear failure is not observed in 3D printed sandwiches.
- Experimental results are in good agreement with theoretical predictions. The deviation between experimental and theoretical modulus and critical load for SH20, SH40, SH60 is 13.18, 11.19, 11.50 %, and 2.64, 4.01, 12.97 %, respectively.

6 COMPRESSIVE BEHAVIOR

6.1 Compressive behavior of 3D printed core

The experimental setup of the compression test is presented in Figure 6.1a. Compressive stress-strain plots of 3D printed neat HDPE and H20 - H60 are depicted in Figures 6.1b and Figure 6.1c. The compressive properties of the 3D printed core samples are calculated using in-house built MATLAB code, and the results are tabulated in Table 6.1. Due to viscoelastic behavior and lower glass transition temperature of HDPE it has higher modulus and is 1.06 times higher than H60. The modulus of foams increases with GMB content (Figure 6.1e). H60 displayed the highest modulus among foams and is 1.18 and 1.08 times higher than H20 and H40. This is due to the presence of intact GMBs at higher filler loading. HDPE displayed 1.23 times higher yield strength compared to H60. SF's yield strength decreases (Figure 6.1f) with an increasing filler loading because of poor interface bonding between constituent elements and raster gaps. At filler loadings, these raster gaps volume increases due to lower CTE. Among foams, H20 (Table 6.3d) displayed the highest yield strength, which may be due to effective load transfer between the constituents and is 1.18 times higher than H60. The excessive plastic deformation of the matrix at higher filler loading makes H60 perform lower than H20. One of the significant aspects of SFs and hollow particles is the stress plateau when subjected to compressive loads. With increasing filler content, the stress plateau region becomes distinguishable. As the GMB volume fraction increases, the stress plateau region becomes more prominent. Compared to H20, the plateau region is distinguishable in H40 and H60 and is observed to be between 20 - 40% strain in the compressive stress-strain graph (Figure 6.1c). Energy absorption at 50 % strain in foams increases with an increase in filler content. H60 showed maximum energy absorption at 50% of 8.33 MJ/m^3 . Moreover, as the load is increased, the plateau region is accompanied by an increase in stress with minimal deformation, resulting in the strain hardening effect. The densification caused by the collapse of in-situ voids and the hollow GMBs causes this significant increase in stress with lower strains. The filler particles start to collapse once the load exceeds the plateau region. Due to continued compressive forces, the void space left after the collapse of GMB particles is filled by the HDPE

matrix, resulting in the densification phenomenon. Foams exhibited better specific properties (Table 6.2) than neat HDPE, indicating their usage in weight-sensitive applications. H60 displayed the highest specific modulus and strength among foams and is, respectively, 1.31 and 1.12 times higher than HDPE.



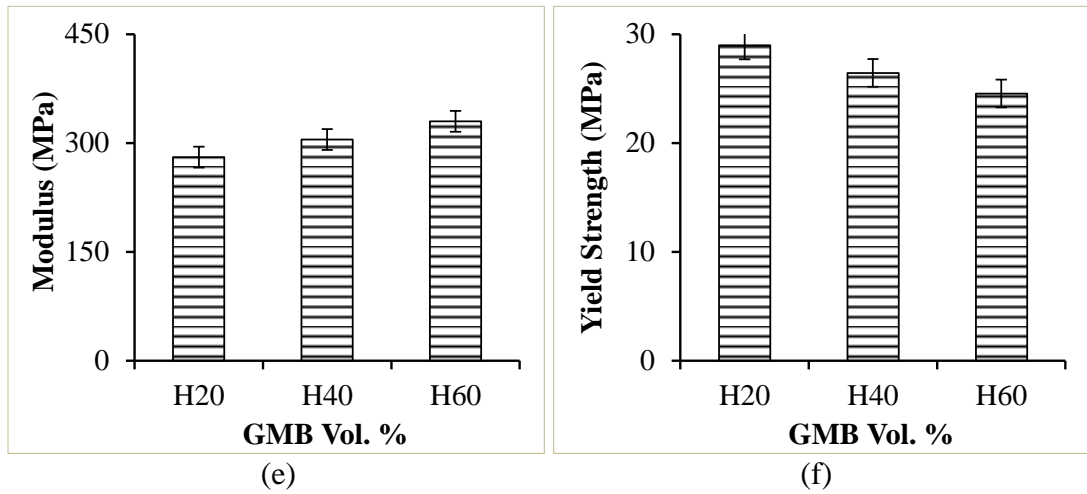


Figure 6.1 (a) Experimental setup (b) compressive stress-strain plots for HDPE (c) foam (d) H20 - before and after compression (e) compressive modulus and (f) yield strength as function of GMB Vol. %.

Table 6.1 Compressive properties of 3D printed H - H60.

Material	Modulus in MPa	Yield Strength in MPa	Yield Strain (%)	Peak Stress in MPa	Plateau Stress in MPa	Energy observed at 50% Strain (MJ/mm ³)
H	348.26 ±10.35	30.25 ±0.85	8.68 ±0.19	68.54 ±0.15	-----	7.96 ±0.55
H20	280.46 ±12.25	28.98 ±1.28	10.33 ±0.24	59.85 ±0.18	-----	6.94 ±0.26
H40	304.84 ±11.58	26.45 ±1.05	8.67 ±0.15	66.42 ±0.13	21.46 ±0.02	7.49 ±0.37
H60	329.95 ±14.85	24.56 ±0.98	7.44 ±0.18	60.25 ±0.09	19.73 ±0.05	8.33 ±0.48

Table 6.2 Specific compressive properties of 3D printed H - H60.

Material	Specific Modulus (MPa/kg/m ³)	Specific Yield Strength (MPa/kg/m ³)×10 ⁻³
H	0.376	32.63
H20	0.339	35.08
H40	0.408	35.46
H60	0.494	36.77

The initial densification is initiated by matrix porosities collapse (Figure 6.2a, c, and e). As the stress level rises, GMB starts to break, resulting in further densification. At higher magnification (Figure 6.2b, d, and f), deformed resin, intact GMB, and debris are visible. Since all the compression samples are tested with constant cross-head

displacement, there is no remarkable difference in the appearance of the fracture surface for these materials concerning strain rate.

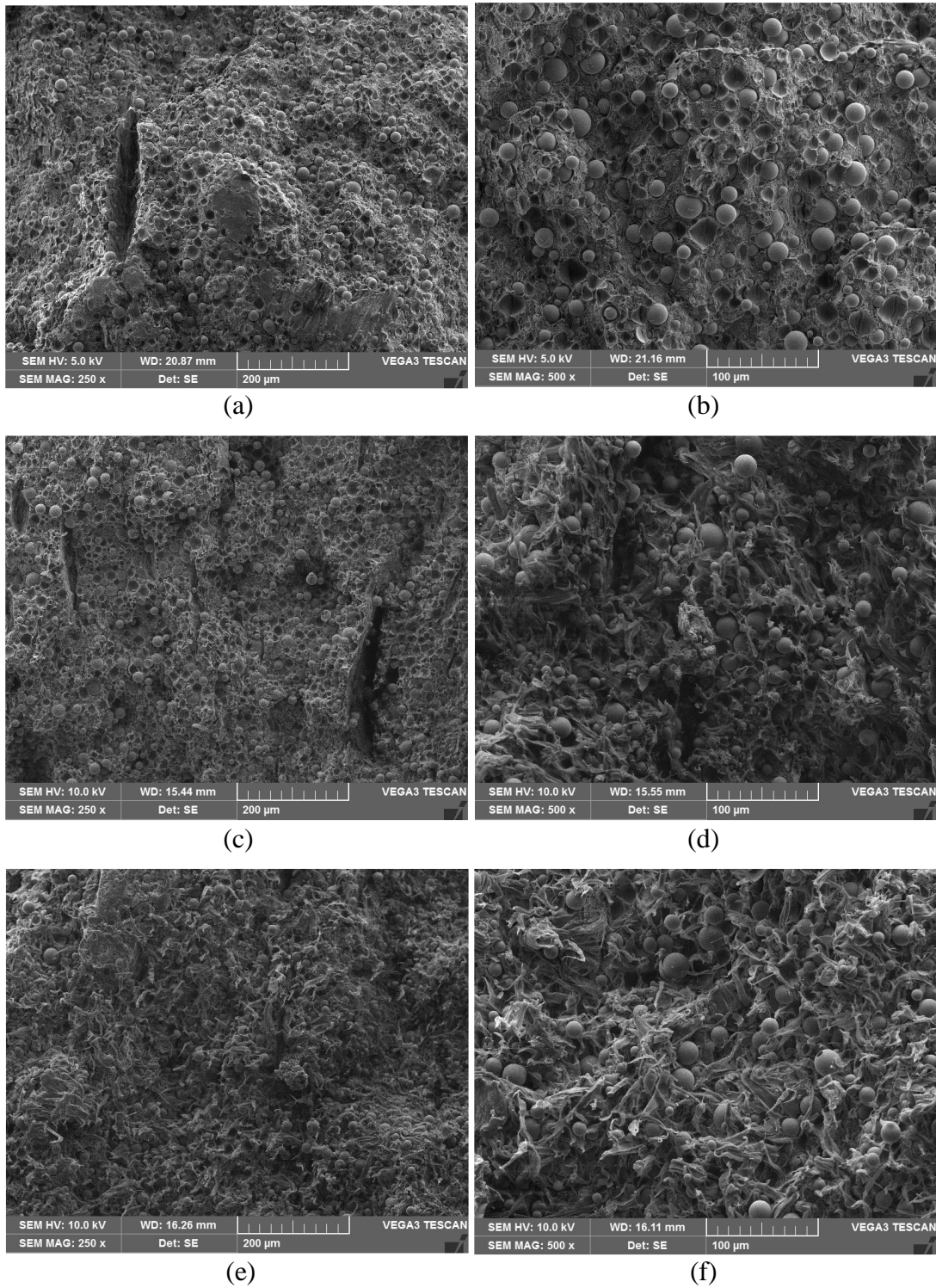
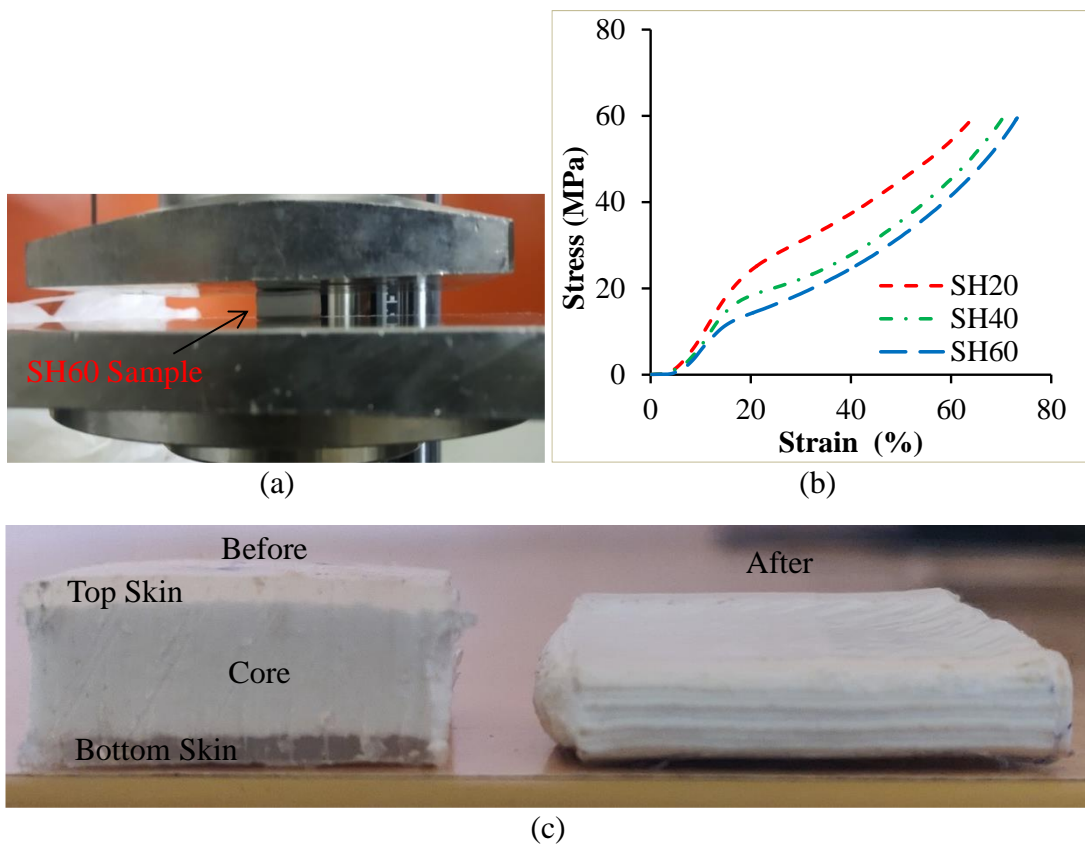


Figure 6.2 Micrographs of compressive tested H20 (a-b) H40 (c-d) and H60 (e-f).

6.2 Compressive behavior of 3D printed sandwich

The 3D concurrently printed sandwich samples show similar compression behavior as that of the core. Figure 6.3a shows the experimental setup of the sandwich SH60 sample under compression. The stress-strain plots of 3D printed neat sandwich samples are shown in Figure 6.3b. Similar to foam core, sandwich compression properties are calculated using in-house built MATLAB code, and the results are tabulated in Table 6.3. The modulus of foams increases with GMB content (Figure 6.3d). SH60 displayed the highest modulus and is 1.48 and 1.33 times higher than SH20 and SH40. Intact GMBs at higher filler loading enhance the moduli of SH60. The yield strength of sandwiches decreases (Figure 6.3e) with an increase in filler loading because of poor interface bonding between constituents and raster gaps with higher filler loadings. The excessive plastic deformation of the matrix at higher GMB content decreases the yield strength. SH20 is the best strength, which might be due to the effective load transfer between the matrix and filler.



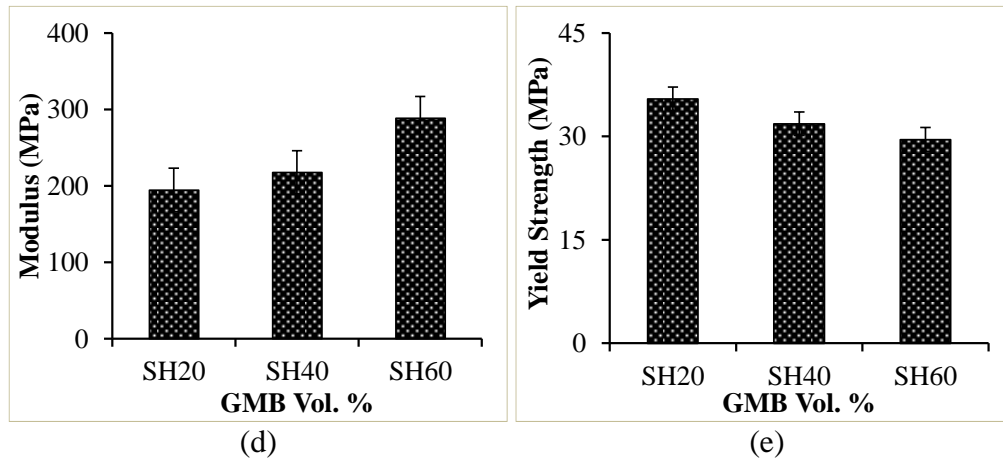


Figure 6.3 (a) Experimental setup (b) sandwich compressive stress-strain plots for 3D printed sandwich (c) SH60 before and after compression (d) compression modulus and (e) yield strength as function of GMB Vol. %.

Table 6.3 Compressive properties of 3D printed sandwiches.

Material	Modulus in MPa	Yield Strength in MPa	Yield Strain (%)	Peak Stress in MPa	Plateau Stress in MPa	Energy observed at 50% Strain (MJ/mm ³)
SH20	194.67 ±13.45	35.47 ±1.05	20.71 ±0.18	58.45 ±0.12	23.56 ±0.04	8.54 ±0.36
SH40	217.62 ±10.27	31.85 ±0.98	16.21 ±0.15	59.23 ±0.11	19.45 ±0.02	9.73 ±0.27
SH60	288.83 ±12.75	29.57 ±1.20	10.23 ±0.25	60.05 ±0.17	17.68 ±0.15	10.22 ±0.58

The yield strength of SH20 is 1.12 times higher than SH60. The stress plateau region becomes more prominent with increasing filler content. The plateau region for sandwich SH20 - SH60 is observed between 20 - 40% of strain (Figure 6.3b). In sandwiches, the energy absorption at 50 % strain increases with increasing filler content. SH60 showed the highest energy absorption at 50% of 10.22 MJ/m³. SH60 has the highest specific modulus and strength (Table 6.4), which can be exploited for potential weight-saving applications without compromising the mechanical properties.

Table 6.4 Specific properties of 3D printed sandwich samples.

Material	Specific Modulus (MPa/kg/m ³)	Specific Yield Strength (MPa/kg/m ³) × 10 ⁻³
SH20	0.221	40.33
SH40	0.279	40.97
SH60	0.399	40.85

The measured compression properties of 3D printed sandwich composites are compared with respective cores. Figure 6.4a presents a yield strength comparison between printed core and respective sandwiches. Though strength is decreasing with GMBs addition, specific yield strength increases and is a crucial factor in weight-sensitive structural applications. The yield strength of SH20, SH40, and SH60 is 1.22, 1.20, and 1.20 times higher than their respective H20, H40, and H60 cores, indicating the potential benefit of realizing concurrently 3D printed SF cored sandwich. Though modulus is less for sandwiches than the core (Figure 6.4b), the specific modulus of sandwiches is higher, an essential design parameter in developing weight-sensitive structures.

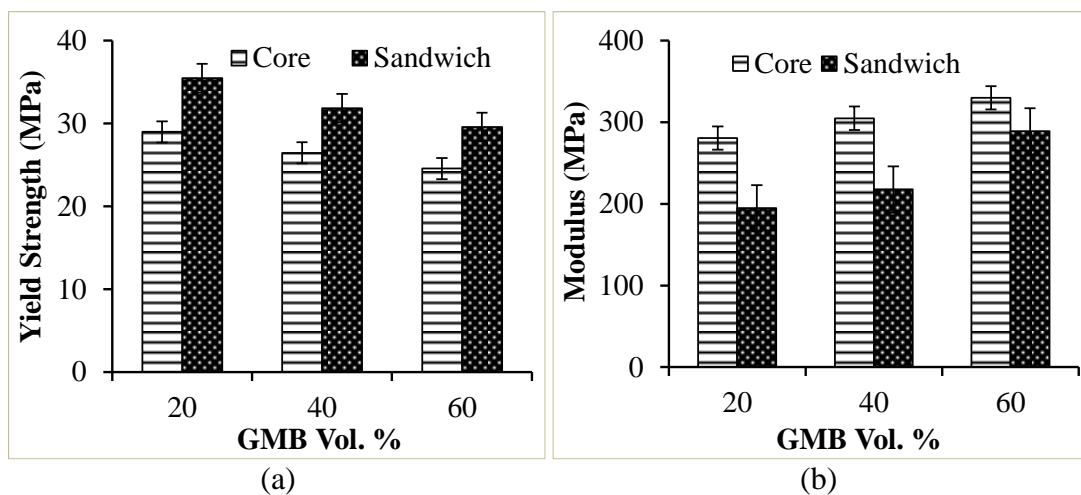
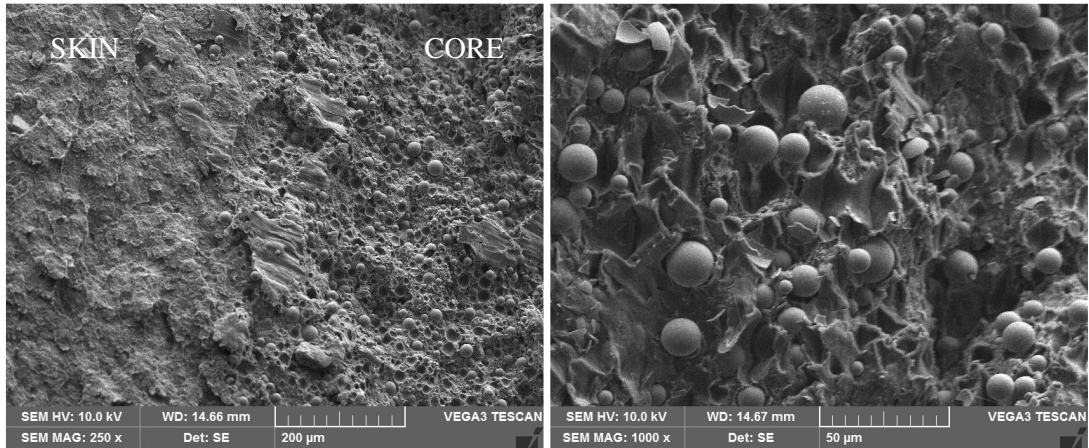


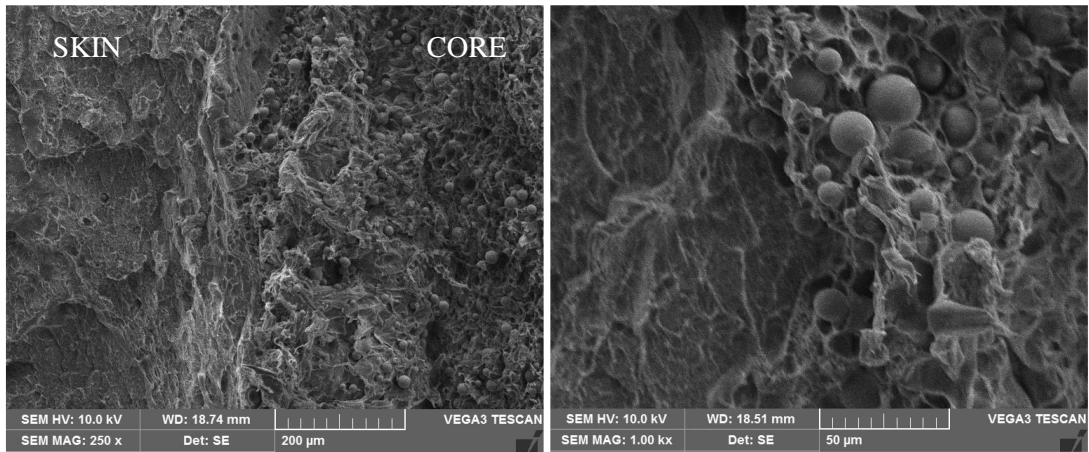
Figure 6.4 Compression property comparison of 3D printed core and sandwich.

With 1 mm HDPE skin at the top and bottom of the core in the sandwich, the densification phenomena take place at higher stress as the HDPE skin resists the applied compressive load. Once the maximum stress level is reached, the initial densification starts by collapsing the voids formed inside the core (Figure 6.5a, c, and e). Further, as the stress level increases, GMB breakage starts resulting in further densification. Figure 6.5b, d, f shows the deformed resin, intact GMB, and debris of sandwich samples at higher magnification. Nonetheless, none of the printed SF cored sandwiches exhibited interfacial separation between core and skin due to the perfect and seamless bonding of skin and core.



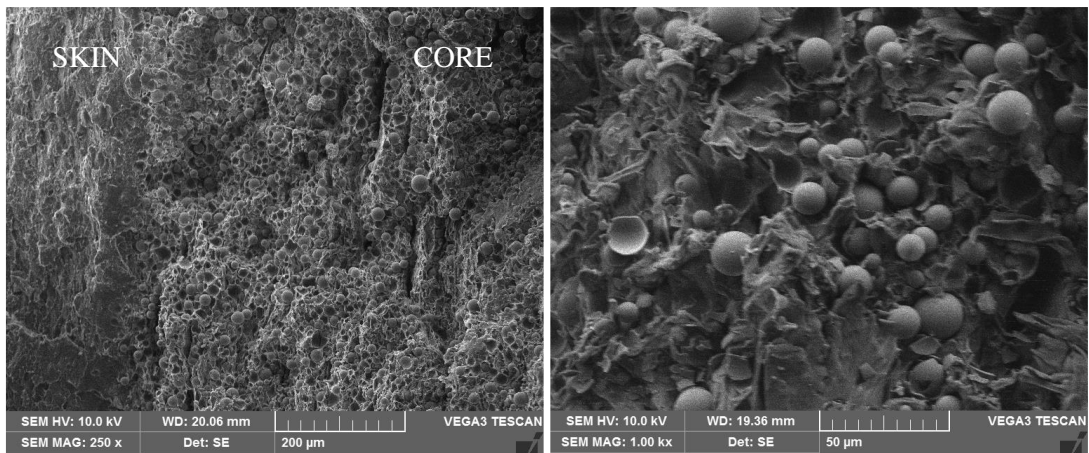
(a)

(b)



(c)

(d)



(e)

(f)

Figure 6.5 Compressive tested SH20 (a-b) SH40 (c-d) and SH60 (e-f).

Conclusions

- The highest specific compressive modulus and yield strength are observed for H60 at 0.5 mm/min of cross head displacement among foam core.
- The yield strength of SH20, SH40, and SH60 is 1.22, 1.20, and 1.20 times higher than their respective H20, H40, and H60 cores, indicating the potential benefit of realizing all at once 3D printed SF core sandwich.
- Specific compressive properties of 3D printed sandwich composites are higher than the core. 3D printed three-phase syntactic foams may be used to create complicated shapes, making them viable promising alternative for buoyant weight-sensitive structures.

7 BUCKLING AND FREE VIBRATION RESPONSE

7.1 Buckling and free vibration of foam core under axial compression

Micrographs of 3D printed freeze fractured H - H60 buckling and vibration samples are presented in Figure 7.1. All the samples are printed using suitable printing parameters (Table 3.4), having a uniform distribution of GMB particles in the HDPE matrix in the case of foams. The microballoons are intact post blending, extrusion, and printing, as seen from Figure 7.1, affirming the suitability of the printing parameters used in the present investigations.

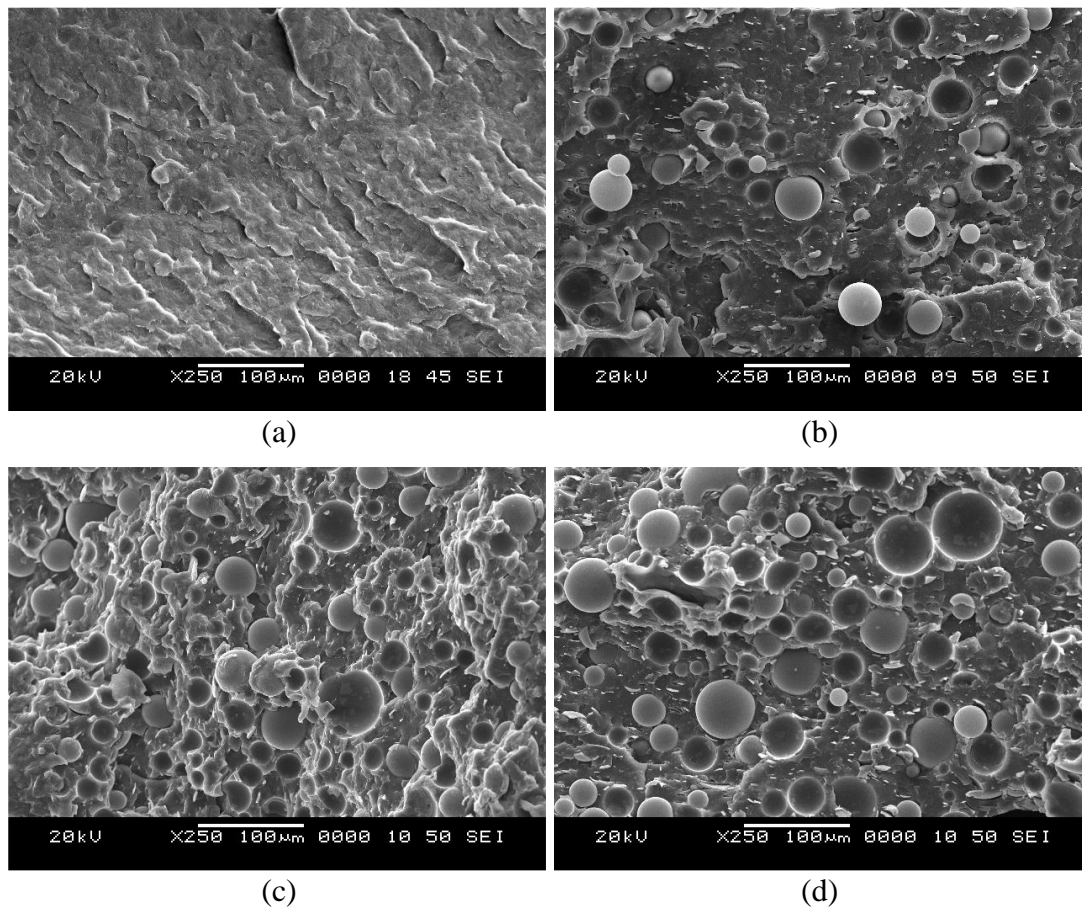


Figure 7.1 Micrographs of 3D printed freeze fractured (a) H (b) H20 (c) H40 and (d) H60.

7.1.1 Buckling investigation

In the buckling test of 3D printed HDPE and foams, it is noted that buckled mode shapes of SF exhibit a typical global buckling mode. All buckled modes have

maximum transverse deflection at the middle and zero deflection at the fixed ends, as seen from Figure 7.2a. The observed buckling behavior of HDPE and foams is presented in Figure 7.2b, and the results are tabulated in Table 7.1. It is noted that the buckling load increases with GMB %. This might be due to an increase in stiffness of foams with an increase in GMB particles in the HDPE matrix. An increase in critical buckling load can be attributed to an increase in the load-bearing capability of composite with an increasing GMB content. The theoretical buckling load for clamped-clamped HDPE and foams is calculated based on the Euler–Bernoulli assumption (Timoshenko 2004) and is expressed as,

$$P_{cr} = \frac{4\pi^2 EI}{L^2} \quad (7.1)$$

where E is the modulus by Bardella–Genna model. Compared to HDPE, the modulus of GMB is many times higher, resulting in a higher critical load for SFs. The experimental critical load for HDPE is 50 N. Compared to pure HDPE, the critical buckling load of H20, H40, and H60 is increased by 5, 36.6, 72.8, and 3, 37, 77.5 % in DTM and MBC methods, respectively. The critical buckling load estimated by DTM is higher than MBC. The difference between them is in the range of 3-8 %. Similarly, the theoretical buckling load of neat HDPE is 57.88 N, increased by 3.71, 40.27, and 89.09 %, respectively, in H20, H40, and H60. The theoretical and experimental buckling loads are in good agreement at lower filler contents. As the filler content increases, the void volume fraction increases, leading to higher deviations in experimental and theoretical results. The buckled mode shapes also noticed that both HDPE and foams did not fail due to delamination between the layers (Figure 7.2a). This can be attributed to the quality of composites printed using suitable printing parameters.

Table 7.1 Experimental and theoretical critical buckling load for 3D prints.

Material	Experimental P_{cr} in N		Theoretical P_{cr} (N)	Deviations in DTM (%)	Deviations in MBC (%)
	DTM	MBC			
H	50±1.5	47±1.3	57.88	13.61	18.79
H20	52.5±2.4	48.41±1.8	60.03	12.54	19.35
H40	68.3±3.5	64.39±2.6	81.19	15.87	20.69
H60	86.4±3.4	83.45±2.2	109.45	21.05	23.37

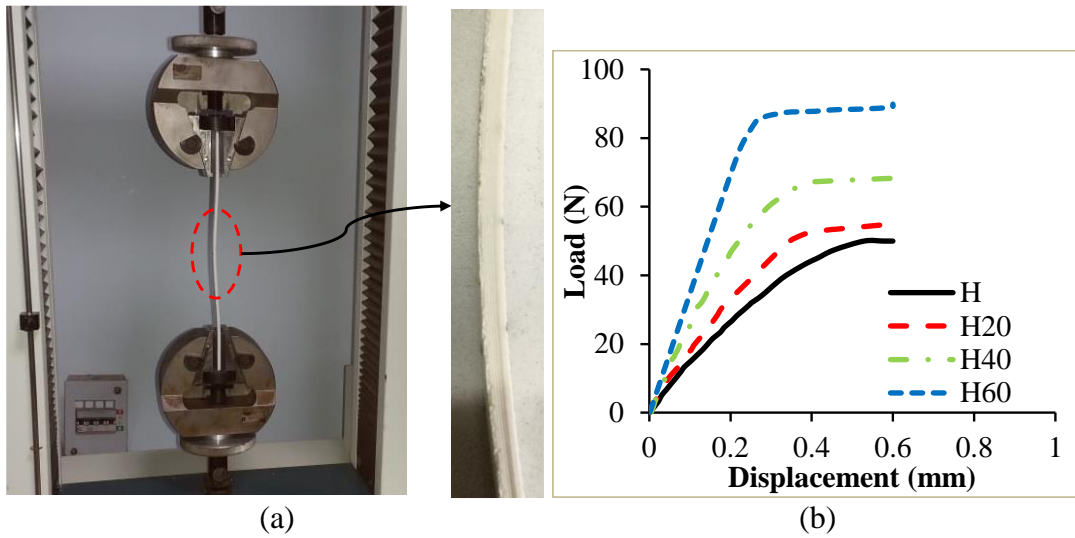


Figure 7.2 (a) 3D printed representative foam sample being tested and (b) plots showing buckling behavior of prints.

The modulus values computed from Bardella-Genna using Equation 2.11 and frequency data for HDPE, and their foams are listed in Table 7.2. Compared to H, the modulus of H20, H40, and H60 is increased by 6.29, 45.89, and 94.54 %, respectively. As GMB content increases, modulus increases posing the higher resistance against the buckling. GMB addition in the HDPE matrix increases the natural frequencies of SFs. The deviation in Young's modulus for H20 - H60 estimated from the Bradella-Genna model and frequency data using Equation 2.11 is 1.79, 2.69, and 2.24 %, respectively. By adding stiffer GMB particles, SFs natural frequency is increasing, which might increase the foams' overall stiffness.

Table 7.2 Modulus comparison between the frequency data and Bardella-Genna model for 3D prints.

Material	Young's Modulus in MPa		% Deviation
	Frequency Data using Equation 2.11	Bradella-Genna model	
H	970.05±13	970.05	-----
H20	1031.10±26	1012.6	1.79
H40	1415.30±24	1376.1	2.76
H60	1887.22±30	1874.1	0.69

7.1.2 Natural frequency of prints

Neat HDPE and SFs studied for their buckling strength under axial compression are investigated for free vibration behavior under the application of axial compressive load. The printed samples are marked into eight equal sections along the length, as shown in Figure 2.9. The frequency response function (FRF) is obtained by exciting the prints at the different marked positions using a roving impact hammer by measuring the corresponding response using an accelerometer. The natural frequency related to the first three forms of bending modes is compared with the analytical solution obtained by solving Equation 2.24. The natural frequency for the first three modes is identified using FRFs obtained using DEWESoft software. A typical frequency response function curve of H60 is presented in Figure 7.3. The natural frequency of all prints tends to decrease as the compressive load increases. It is necessary to maintain a constant amount of compressive load over a time period such that free vibration response can be measured efficiently and accurately under the applied compressive load, which is achieved by controlling the load program in the UTM by an increment of 20 N.

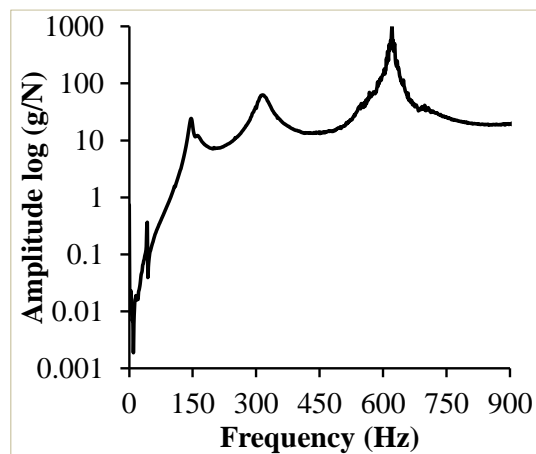


Figure 7.3 FRF of H60 at no load condition.

The load is kept constant after each increment for 2 minutes, during which the free vibration test is performed. The load increment is continued until the print is sufficient to withstand the applied compressive load. This load is usually slightly greater than the critical buckling load. Experimentally, owing to the attainment of

geometric stiffness resulting from beam deflection, the first natural frequency at the buckling site increases in the post-buckling region. A similar trend on isotropic/composite beam and columns is observed in previous studies (Rajesh and Pitchaimani 2017). The first natural frequency of H - H60 under axial compressive loads similar to P_{cr} tends to become zero theoretically (Figure 7.4). As the compressive load gets closer to the P_{cr} , the first natural frequency decreases gradually owing to the structural stiffness loss of prints.

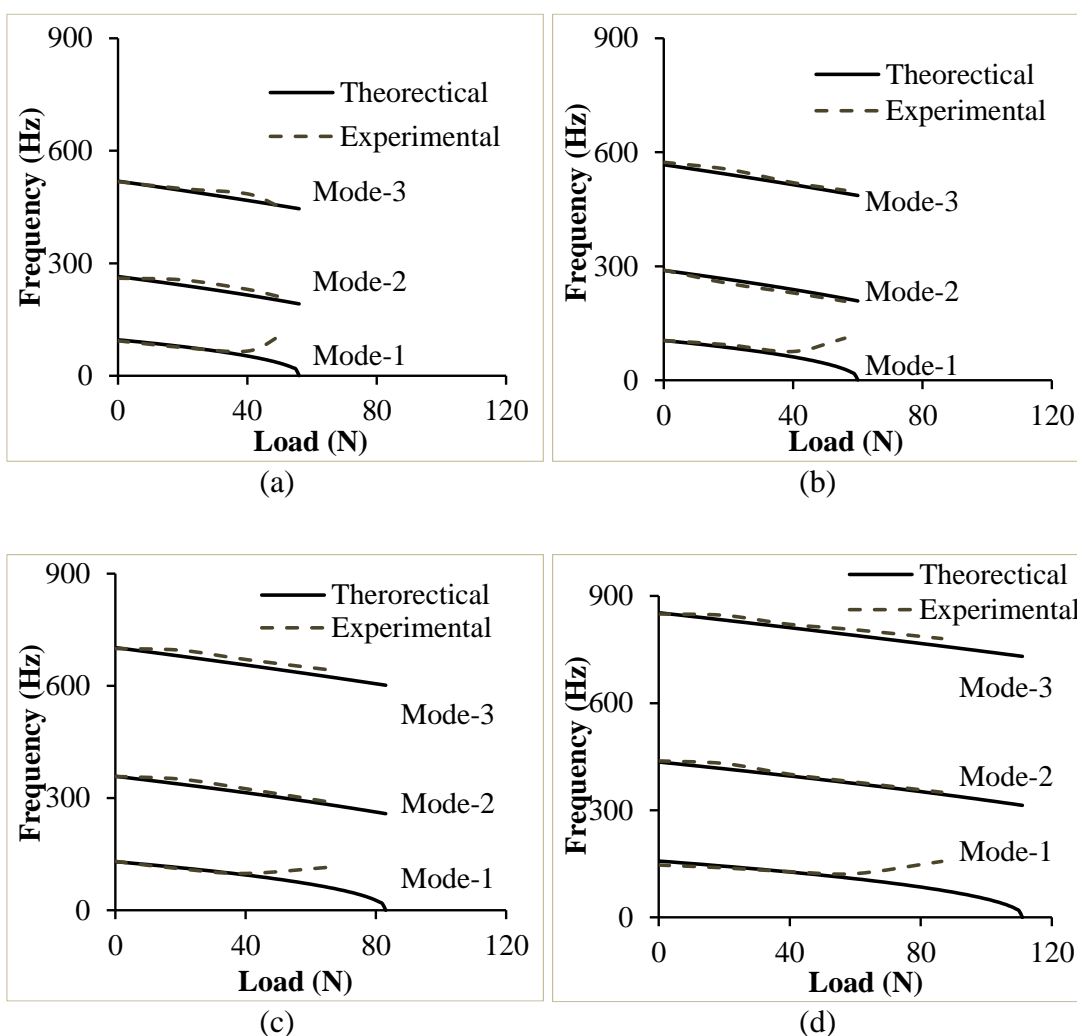


Figure 7.4 Natural frequency vs. compressive load for representative (a) H (b) H20 (c) H40 and (d) H60.

7.1.3 Critical buckling load estimation using VCT

The critical load of pure HDPE and SFs are calculated from vibration data using the vibration correlation technique (VCT) (Abramovich et al. 2015, Arbelo et al. 2014, Arbelo et al. 2015, Souza and Assaid 1991). It is a non-destructive test used to calculate critical load using vibration data. In this method, the natural frequency is evaluated experimentally by applying a compressive load lower than the critical load. The process is continued for several load trials, and the accuracy of the technique relies on the estimation of critical load with data that corresponds to reduced levels of compressive loadings. Figure 7.5a shows the crucial load for H - H60 by plotting the squared value of fundamental frequency against compressive load. By using second-order polynomial expression (Equation 7.2), the plot is extrapolated to obtain critical load.

$$\left(\frac{f}{f_n}\right)^2 = 1 - \left(\frac{P}{P_{cr}}\right) \quad (7.2)$$

where f_n and f are fundamental frequencies at no load condition subjected to compressive load, P .

Figure 7.5b presents the comparison of critical buckling load calculated using VCT, DTM, and MBC methods for variation in GMB content. As observed in buckling experiments, the buckling load estimated for each configuration from VCT increases with an increase in GMB content. It is observed that, for H and H40, the buckling load estimated through VCT is closer to that of load calculated from DTM and MBC methods. But in the case of H20 and H60, VCT over-estimated the buckling loads. The comparative analysis of these methods helps in quantifying the range of values with lower and upper bounds within which deviations may occur.

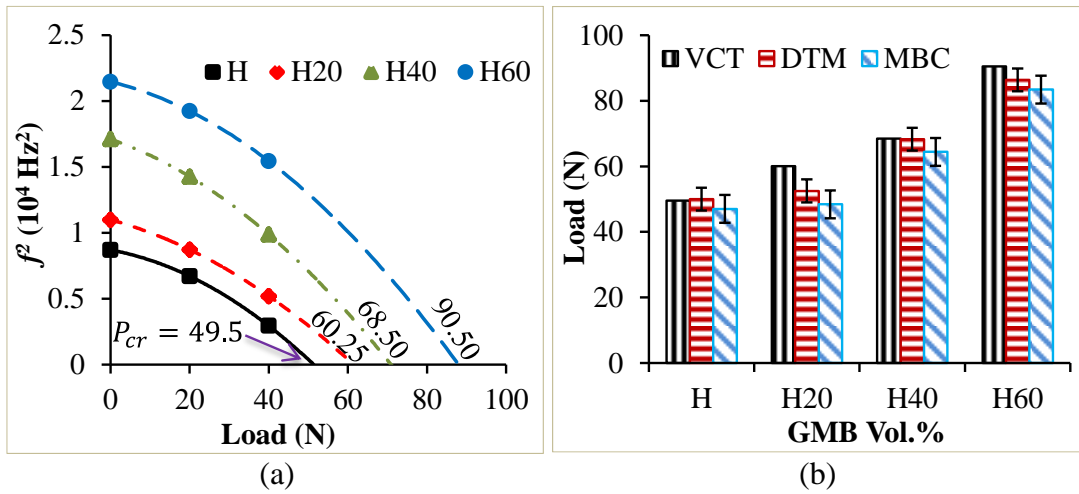


Figure 7.5 (a) Critical Buckling load for H – H60 using VCT and (b) comparison of critical buckling load through VCT, DTM and MBC.

7.1.4 Property map

For lightweight applications, composite density is a crucial factor, and the low density of SFs enables them to be used in weight-sensitive structures. Figure 7.6 presents the buckling load as a function of composite density available from the literature (Rajesh and Pitchaimani 2017, Waddar et al. 2018, Waddar et al. 2018). Data on thermoplastic-based SFs developed through conventional manufacturing methods cannot be compared with 3D printed foams. Hence, in this section 3D printed thermoplastic foams are compared with thermosetting foams. From the literature, extracted data of the density and buckling load for cenosphere reinforced epoxy-based foams (treated and untreated) and natural fiber embedded thermoset composite materials are presented in Figure 7.6.

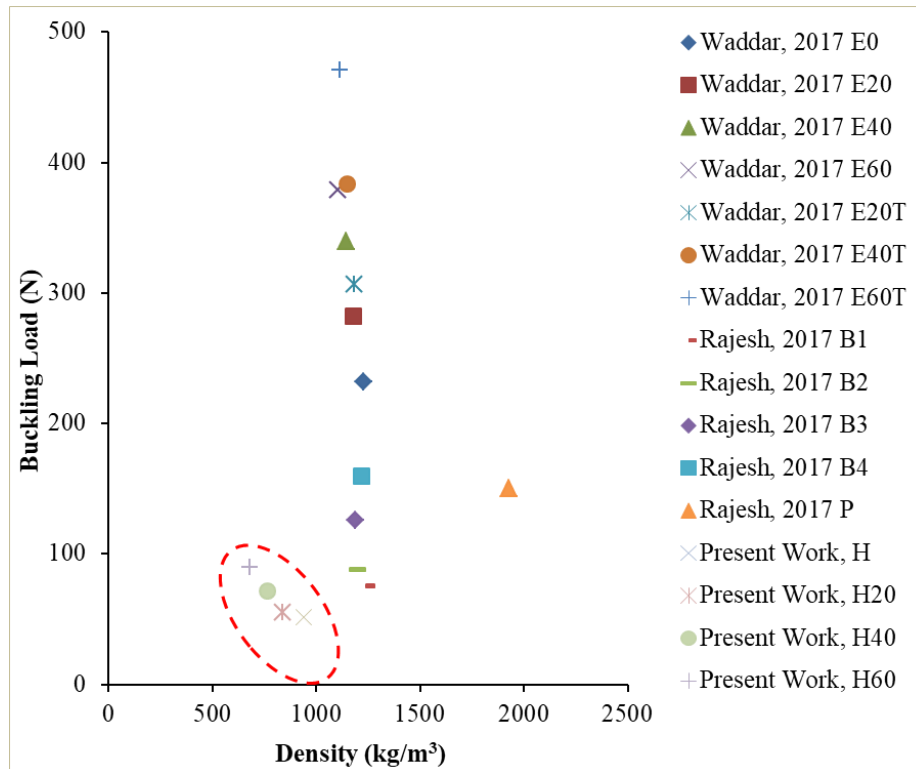


Figure 7.6 Buckling load as a function of density (Rajesh and Pitchaimani 2017, Waddar et al. 2018, Waddar et al. 2018).

Selection of suitable matrix, filler material, and volume fraction is important to build structural components exposed to axial compressive load wherein mode failure is predominantly buckling. It is found that both natural fiber and GMB based SFs are susceptible to buckling failure than cenosphere based foams. As mentioned earlier, 3D printed thermoplastic is being compared here with epoxy based (thermosetting) SFs. Nevertheless, such a comparison can guide industrial practitioners and designers to know the broad ranges of values across thermoplastic and thermosetting foams regimes. A very interesting point to note from this comparison is the superior performance of 3D printed H60 compared to woven natural fabric thermosetting composites indicating the potential of the 3D printed H60 as presented as part of this investigation. 3D printed HDPE/GMB SF integrated lightweight components (leak proof due to joint less feature) having complex geometries can replace few components subjected to axial compressive loading scenarios in aerospace, automotive and marine sectors.

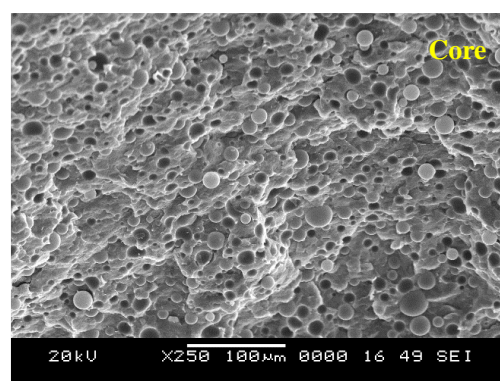
7.2 Buckling and free vibration of printed sandwiches under axial compression

The printing parameters used for realizing concurrently printed sandwich exhibits distinct parallel layers without any defects, as evident from Figure 7.7.

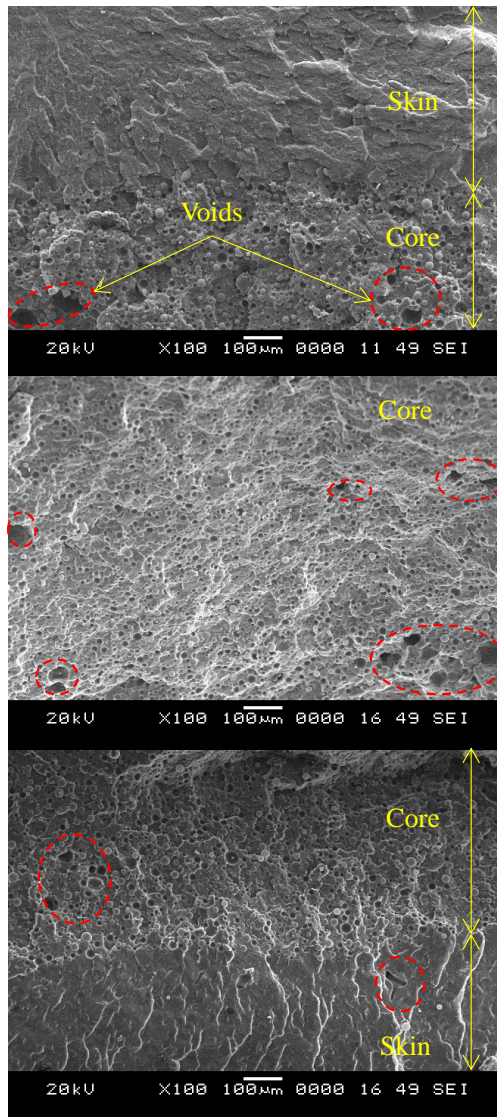


Figure 7.7 Concurrently 3D printed representative SH60.

It is observed that good quality samples can be printed using suitable printing parameters (Table 3.4). Figure 7.8a depicts intact GMBs being uniformly dispersed in HDPE. The micrographs of SH60 along the thickness of the sample are presented in Figure 7.8b, revealing seamless interface and opt diffusion between the skin and core interface without any delamination and layer shift issues. The formation of voids makes the foam core a three-phase structure (HDPE, GMB, and voids). The void content increases with GMB content, which might be due to residual micro-porosities between the two adjacent layers. Due to the lower MFI, raster gaps will be more at higher filler contents resulting in increased void content. These voids might act as additional cushioning zones enhancing damping capabilities and reducing weight further, which might not be possible with foam alone.



(a)



(b)

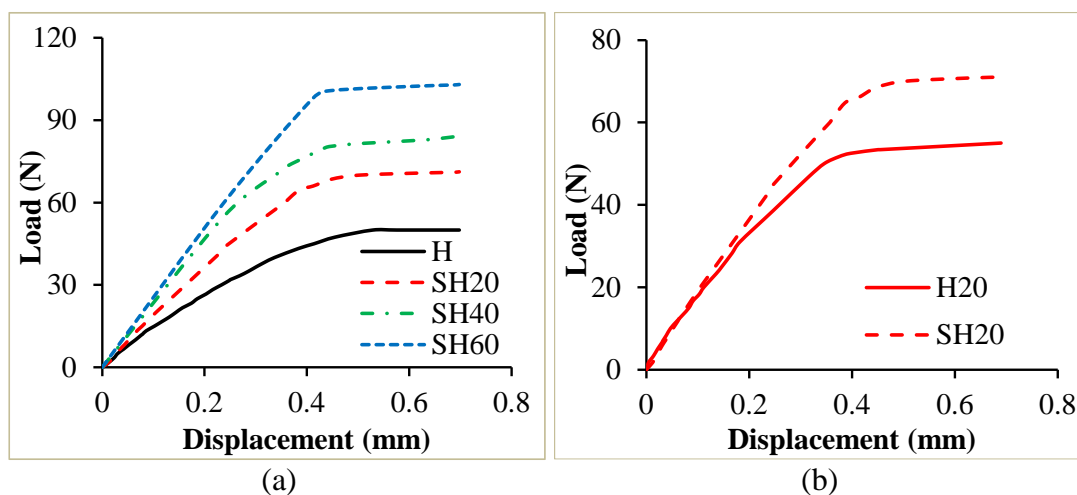
Figure 7.8 Micrographs of (a) SH20 core and (b) concurrently 3D printed SH60 across the thickness.

7.2.1 Buckling behavior

The concurrently 3D printed neat HDPE and sandwiches are subjected to axial compression through UTM with a clamped-clamped boundary condition, as shown in Figure 2.10a. Using the DAQ, the deflection along the sandwich axis is measured. DTM and MBC are applied to the load-deflection plots (Figure 7.9a) for P_{cr} estimations (Table 7.3). The sandwich buckling load increases with an increasing GMB content. This is due to the intact GMB particles enhancing the overall stiffness

of the sandwich in addition to seamless bonding between the skin and core. The concurrently printed sandwiches displayed global buckling mode during the buckling test, wherein the highest deflection is reported at the mid-section without skin wrinkling, delamination, and skin micro buckling (Figure 7.9c). This is due to the lower magnitude of compressive stresses in HDPE skin compared to the micro buckling and wrinkling strength of HDPE (Corigliano et al. 2000). The delamination of skin is the most common mode of failure of the sandwich structure under compression, which is seen to be absent for all concurrently printed sandwiches affirming a very good seamless bonding between the skin and core, as seen from Figure 7.8b.

Table 7.3 presents the lower and upper bounds P_{cr} , which vary in the range of 8.4-2.41% for SH20-SH60, respectively. SH20 - SH60, compared to H, exhibited a significant load enhancement of 39.96 - 96.56% and 37.36 - 104.19%, respectively, in DTM and MBC. Among sandwiches, compared to SH20, the P_{cr} of SH60 is increased by 40.44% by the DTM method and 48.65% by the MBC method. The P_{cr} of printed representative H20 and SH20 is presented and compared in Figure 7.9b.





(c)

Figure 7.9 Load-deflection behavior of (a) printed HDPE and sandwich (b) comparative analysis of representative H20 and SH20 and (c) buckled representative SH60.

Table 7.3 P_{cr} of printed sandwiches.

Material	P_{cr} (N)	
	MBC	DTM
SH20	64.56±1.75	69.98±2.80
SH40	73.78±2.49	76.85±3.52
SH60	95.97±2.86	98.28±3.74

From Table 7.4, P_{cr} H20 - H60 increased in the range of ~5-73, and 3-78 % respectively in DTM and MBC compared to H. This indicates that stiffer GMB additions significantly enhance the buckling load of the SF core. Furthermore,

compared to the corresponding H20 - H60, the P_{cr} of SH20 - SH60 is further enhanced by 33.30, 12.52, 13.75% and 33.36, 14.58, 15% respectively, in DTM and MBC techniques. Among printed sandwiches, the enhancement of P_{cr} is substantial in SH20 compared to SH60, which might be due to the lower void contents in SH20 compared to SH60 (Table 5.2). Further, under the applied load, voids present in the buckled region might elongate more, decreasing the % enhancements. Nonetheless, SH60 registered the highest P_{cr} . The overall enhancement in P_{cr} can be attributed to intact GMBs, seamless defect-free skin-core interface, absence of delamination between layers, and absence of shear failure, which in turn is due to concurrent printing of SF cored sandwiches.

Table 7.4 P_{cr} estimations through DTM and MBC methods.

Syntactic foam	P_{cr} (N)		Type of Sandwich	P_{cr} (N)		% Increase in sandwich wrt core (DTM)	% Increase in sandwich wrt core (MBC)
	DTM	MBC		DTM	MBC		
H	50 ±1.5	47 ±1.3	----	----	----	----	----
H20	52.5 ±2.4	48.41 ±1.8	SH20	69.98 ±2.80	64.56 ±1.75	33.30	33.36
H40	68.3 ±3.5	64.39 ±2.6	SH40	76.85 ±3.52	73.78 ±2.49	12.52	14.58
H60	86.4 ±3.4	83.45 ±2.2	SH60	98.28 ±3.74	95.97 ±2.86	13.75	15.00

7.2.2 Free vibration response

The experimental modal analysis is performed using DEWETRON. The FRF curve for representative SH20 samples is presented in Figure 7.10. Furthermore, the experimental frequencies are compared with those obtained through numerical simulation through FEA. Table 7.5 lists the first three experimental sandwich natural frequencies as a function of applied axial compression. GMBs enhance sandwich frequency as their uniform dispersion in HDPE increases the structural stiffness. Figure 7.11 exhibits a declining frequency trend with increasing compression. It is also observed that the frequency rapidly decreases at the closest point of P_{cr} resulting in lower structural stiffness. The fundamental frequencies of sandwich approach to a

minimum when the applied load reaches near to P_{cr} and increases sharply beyond it due to the improved structural stiffness due to post-buckling geometric deformation (Figure 7.11). Similar findings are reported in (Mirzabeigy and Madoliat 2016, Rajesh and Pitchaimani 2017, Wu et al. 2015).

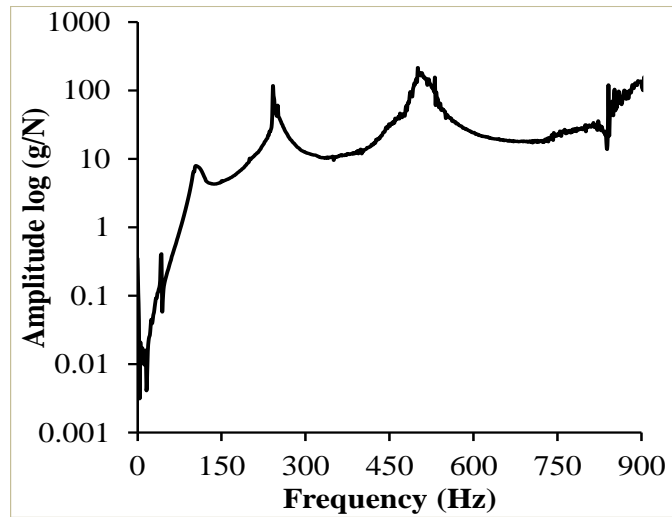


Figure 7.10 FRF curve of representative SH20 under axial compression.

Table 7.5 Natural frequency estimations through experimental route of all the prints.

Material	Mode	Load (N)						
		0	20	40	60	80	100	120
H	1 st	93.3	75.5	65.8	105.5			
	2 nd	260.2	255.6	230.5	210.8		$P_{cr} = 52$ N	
	3 rd	517.8	498.8	485.2	450.8			
SH20	1 st	119.5	106.8	100.5	90.5	135.7		
	2 nd	296.7	265.8	230.7	208.5	200.6		$P_{cr} = 73$ N
	3 rd	583.5	550.8	528.7	480.5	430.8		
SH40	1 st	126.6	110.3	103.2	98.8	127.8		
	2 nd	308.2	279.5	245.8	215.9	195.8		$P_{cr} = 80$ N
	3 rd	632.6	590.8	560.5	498.5	384.5		
SH60*	1 st	138.2	120.8	112.4	104.2	100.8	98.3	155.8
	2 nd	326.4	290.8	265.7	248.8	230.5	217.8	211.7
	3 rd	698.2	660.5	615.8	585.6	540.2	464.7	452.8

* $P_{cr} = 102$ N

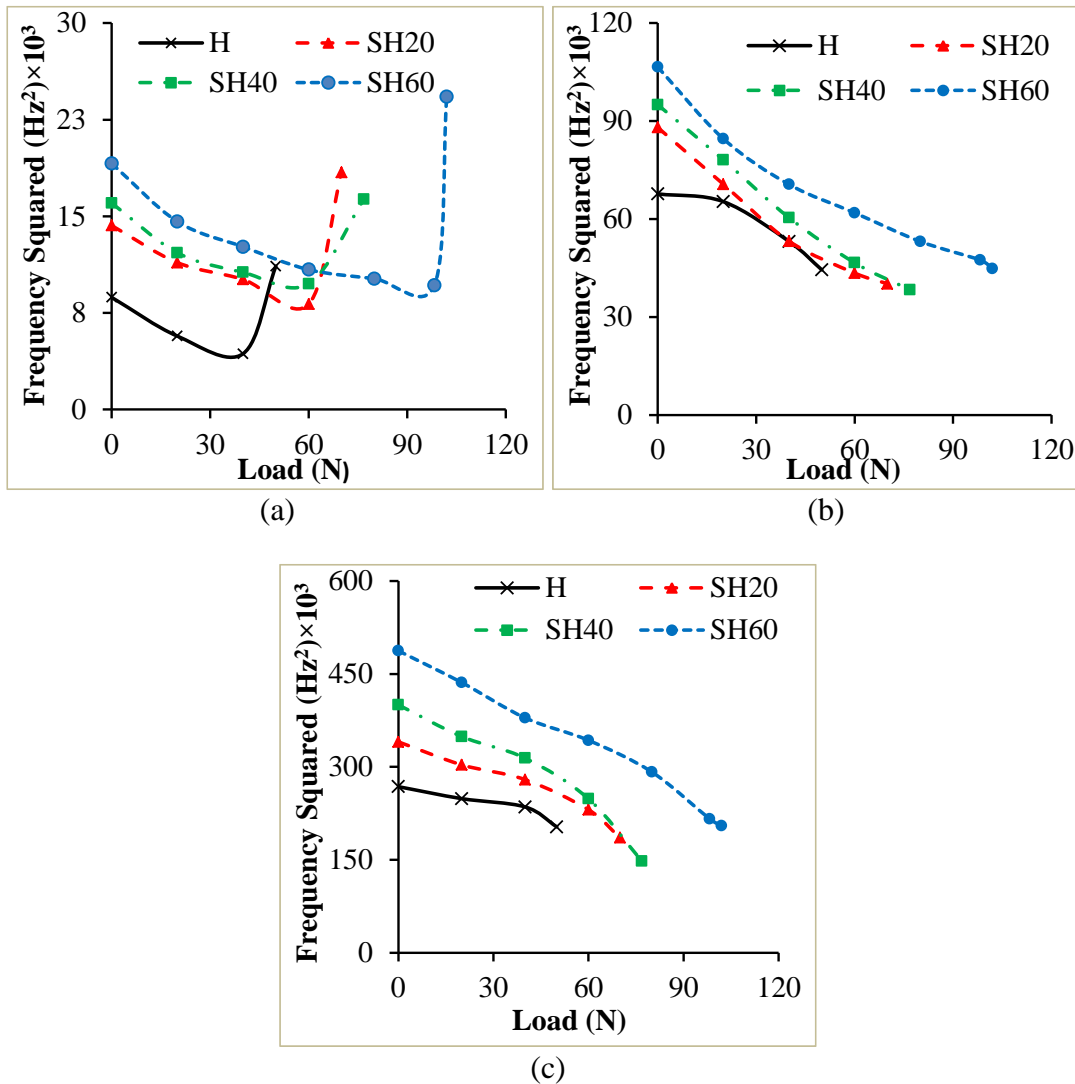


Figure 7.11 Axial compressive influence on the natural frequencies of (a) 1st (b) 2nd and (c) 3rd modes.

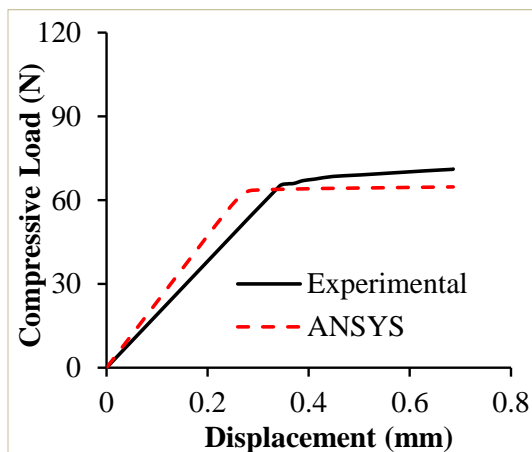
7.2.3 Comparative analysis

The Bardella-Genna route is used to obtain the elastic properties associated with HDPE and GMB based SF (Table 7.6) and, in turn, utilized as inputs for FEA. The calculated elastic properties of HDPE and sandwiches are presented in Table 7.6. Initially, the fundamental buckling mode deduced from linear Eigenvalue buckling analysis accounts for the geometrical imperfections. Then the non-linear structural analysis is performed to calculate the numerical buckling load using the load - deflection curve. The experimental and numerical load - deflection curves of sandwiches are presented in Figure 7.12. Table 7.7 shows the experimental and

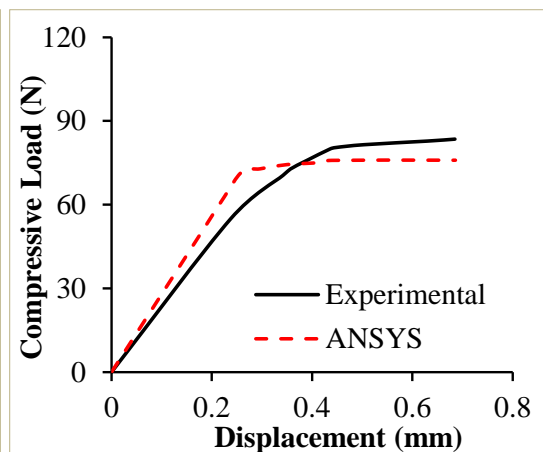
numerical buckling loads of sandwiches. Figure 7.13 represents the first buckling mode shaped of SH20. The maximum deviation between experimental and numerical buckling results is reported to be 10.29%. The experimental results presented in Table 7.7 are higher than the numerical predictions due to well-diffused layers leading to better stiffness in concurrent printing. The modal analysis is performed in ANSYS to extract natural frequencies of the first three modes of sandwich under no-load conditions. The results are listed in Table 7.8. It is observed that both the experimental and numerical results are in good agreement. The concurrently 3D printed sandwiches exhibited higher buckling and natural frequencies than their corresponding SF cores. In this study, concurrent printing of lightweight sandwiches is successfully demonstrated, opening new avenues of realizing complex-shaped integrated sandwich structures through 3D printing.

Table 7.6 Young's moduli predictions through Bardella-Genna model.

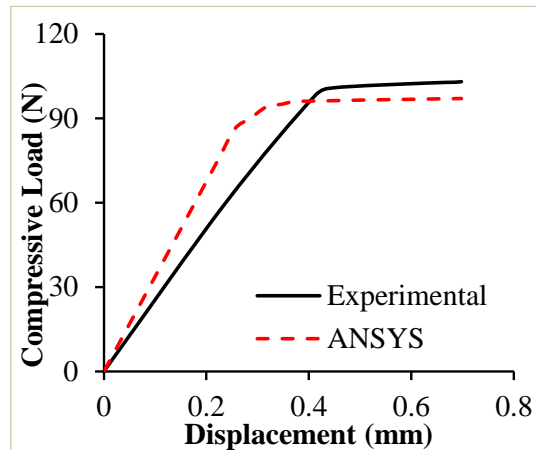
Material	Young's Moduli (MPa)	Poisson's ratio
H	970.05	0.425
H20	1012.6	0.382
H40	1376.1	0.339
H60	1874.1	0.296



(a)



(b)



(c)

Figure 7.12 Experimental and ANSYS comparative plots for (a) SH20 (b) SH40 and (c) SH60.

Table 7.7 P_{cr} using experimental and numerical approaches.

Material	P_{cr} Experimental (N)		P_{cr} Numerical (N)		% Deviations between experimental and numerical predictions	
	DTM	MBC	DTM	MBC	DTM	MBC
SH20	69.98 ±2.80	64.56 ±1.75	63.45	61.70	10.29	4.64
SH40	76.85 ±3.52	73.78 ±2.49	74.15	71.85	3.64	2.69
SH60	98.28 ±3.74	95.97 ±2.86	94.08	89.85	4.46	6.81

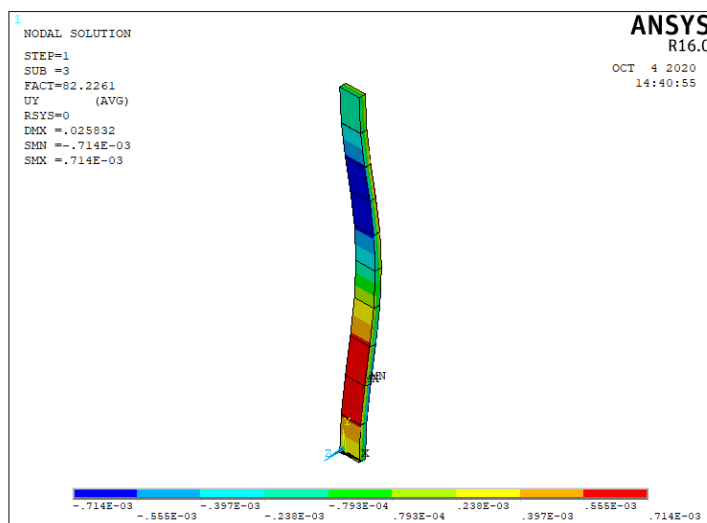


Figure 7.13 First Buckling mode shape of representative SH20.

Table 7.8 Comparison of natural frequencies at no load condition.

Material	Mode	Natural Frequency (Hz)	
		Experimental	Numerical
SH20	1 st	119.5	110.43
	2 nd	296.7	287.45
	3 rd	583.5	583.18
SH40	1 st	126.6	117.16
	2 nd	308.2	319.03
	3 rd	632.6	678.70
SH60	1 st	138.2	137.45
	2 nd	326.4	358.74
	3 rd	698.2	793.81

Conclusions

- Neat HDPE and foams of length 310 mm are printed without any delamination of layers and warpage using suitable printing parameters.
- The increase in GMB content increases both the buckling load and the natural frequency of the printed core and sandwiches.
- The critical buckling load of H20, H40, and H60 is increased by 5, 36.6, 72.8, and 3, 37, 77.5 % respectively compared to neat HDPE when estimated through DTM and MBC.
- Compared to pure HDPE, the modulus of H20, H40, and H60 is increased by 6.29, 45.89, and 94.54 %, respectively.
- The deviation in modulus for H20 - H60 calculated from the Bradella-Genna model and frequency data is 1.79, 2.76, and 0.69 %, respectively.
- Experimentally, the first natural frequency at the buckling site reaches a minimal value and is rapidly increasing in the post-buckling region.
- A decrease in natural frequency is observed with increasing compressive load for all the prints.
- By comparing critical buckling load through various methods, HDPE and H40 show the close agreement of critical buckling load across all methods except for H20 and H60, wherein VCT over-estimated the buckling loads.
- Property plot reveals the superior performance of 3D printed H60 foam as compared to natural fabric woven thermosetting composite.

- Printed sandwiches displayed global buckling mode shapes without any skin wrinkling or delamination.
- Compared to H20 - H60, the buckling loads and natural frequency of SH20 - SH60 are higher.
- The increase in frequency displays the lowest value at P_{cr} and subsequently increases after the post-critical buckling regime due to the geometrical stiffness gain.
- Experimental results match well with the numerical predictions.

8 3D PRINTED INDUSTRIAL COMPONENTS

3D printing allows for the fabrication of components without compromising the strength-to-weight ratio than conventional processing routes. 3D printed SF-based prints and their sandwiches provide a potential way for more direct industrial applications of geometrically complex parts. 3D printed syntactic foams can potentially replace parts made using traditional fabrication techniques which have limits in terms of complicated geometries higher production time, and expenses. The increasing popularity of 3DP over traditional processing has resulted in a number of benefits, including the production of highly specific intricate structures, material savings, design versatility, and customization. The accuracy of the 3D printed composite is determined by the printing method's accuracy, printing size, and the effect of external factors. Despite the challenges of print resolution, surface finish, quality, and layer adhesion, 3DP allows look-in components with micro-scale features. Hence, some of the industrial scale components are 3D printed in the present work to show the feasibility of developed filaments in 3D printers by considering the component's weight as the key factor. HDPE is the most commonly used polymer in producing consumer products. Many current parts can be benefited from GMB filled HDPE SFs to offer lightweight solution in addition to substantial HDPE usage reductions leading to a cost – effective proposition. For specific applications, a reduction in failure strain can be a limiting factor. Concerns about mismatches in the CTE of particle and matrix, which can lead to interfacial separation or material failure, are also important factors to be considered. As a result, the applications for such novel materials must be carefully considered. Many available HDPE parts are identified and the process parameters used in this study are utilized to print these components in syntactic foams. For lightweight applications, composite density is a crucial factor, and the lower density of SFs enables them to be used in weight-sensitive structures. From the present study, it is observed that among foams, H60 has a higher weight-saving potential of ~28% with respect to neat HDPE, and the presence of GMB offers resistance to the flow of the polymer chain. Thereby, dimensionally stable foam prints can be produced without any warpage. H60 filament is used to print some of the industrial components as shown in Figure 8.1.

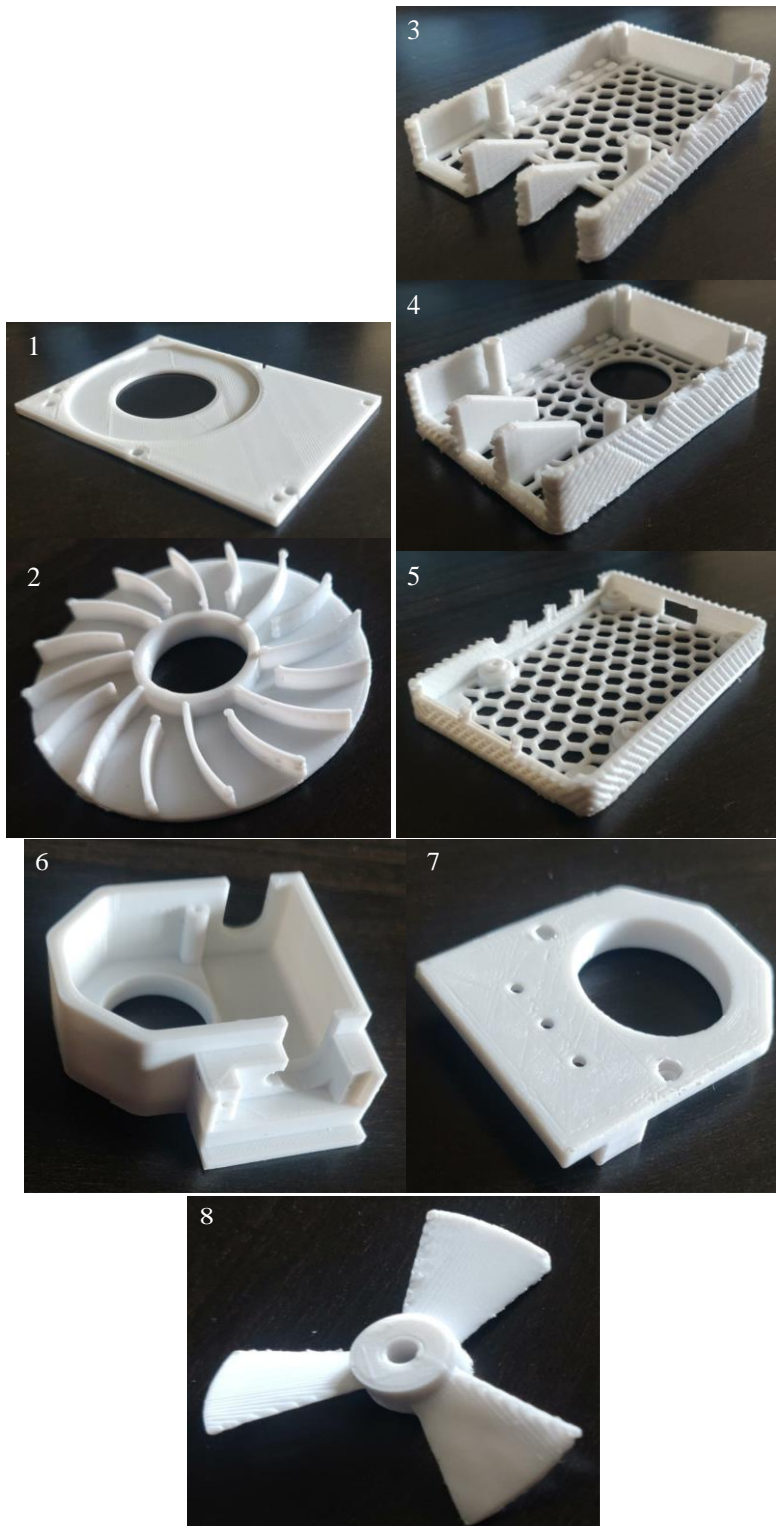


Figure 8.1 Representative components printed using H60 1. Hard disk fan cover 2. Hard disk cooling fan 3. External device connector - top case 4. External device connector - colling fan unit 5. External device connector - lower case 6. Power pac - lower case 7. Power pac - top case and 8. Thrust propeller.

Table 8.1 reports each of these materials, as well as the effect of manufacturing them with SFs. The parts are 3D printed to reduce the component's weight by using the H60 filament. Complex-shaped, thin sectioned, intricate details can be produced in large volumes, as shown in Figure 8.1, resulting in lower costs. It should also be known that, apart from blending GMB in the initial feed, the overall 3D printer settings and parameters have been kept stable, allowing for easy industrial adaptation of lighter components. Using H60 in HDPE, an average weight-saving potential of 21.8 % can be achieved in the selected eight parts.

Table 8.1 Details of 3D printed components.

No.	Component Name	Weight of HDPE component (g)	Weight of H60 component (g)	Weight saving potential w.r.t HDPE (%)	Average weight saving potential w.r.t HDPE (%)
1	Hard disk fan cover	236.24	184.03	22.10	21.81 %
2	Hard disk cooling fan	195.71	152.45	22.10	
3	External device connector - top case	846.73	659.56	22.11	
4	External device connector - colling fan unit	456.92	355.92	22.10	
5	External device connector -lower case	548.73	440.26	19.77	
6	Power pac - lower case	962.69	749.89	22.10	
7	Power pac - top case	215.03	167.50	22.10	
8	Thrust propeller	268.66	209.27	22.11	

SUMMARY AND CONCLUSIVE REMARKS

Summary

GMB-based lightweight composite foam feedstock is successfully synthesized to be used on a commercial printer for weight-sensitive applications. Filaments and 3D printed samples are tested for mechanical characterization to check their adaptability and feasibility for 3DP applications. The GMB/HDPE core with HDPE skin forms the printed sandwich through FFF. SF filaments are manufactured by dispersing GMBs (20 - 60 vol. %) in HDPE. The influence of GMB content is investigated on filament on prints. Further foam filaments are extruded by using suitable extrusion parameters with minimum to no filler breakage. Extruded filaments are used as feedstock material in a 3D printer to print core and sandwich samples concurrently and are subjected to various mechanical tests. Extensive SEMs are taken for correlating property-structure and failure mechanism discussions. The outcome of the thesis is presented in the form of data comparison of prints with the literature and representative printed components. The property map as presented in this thesis is very useful for industry practitioners and serves as a guideline for selecting the right process/composition for the envisaged application.

Conclusions

The main conclusions are summarized as:

Blend characterization

- The MFI of neat HDPE has decreased as the GMB content is increased. With increased GMB %, rheological data show a significant rise in complex viscosity, loss, and storage modulus.
- Values of complex viscosities are maximum at low frequencies and decrease as frequency increases.
- With increasing filler loading and frequency, both storage and loss modulus exhibited an increasing trend.

Density

- In comparison to theoretical values, there is a decrease in the experimental density of both filament and 3D prints.
- With increasing filler content, the void content and weight-saving potential increase, and their values are more prominent for 3D printed core and sandwiches than for the respective filament.
- The 3D printed foam core has less density than respective sandwiches because of the presence of HDPE skin.

Filament development and 3D printing of core and sandwiches

- HDPE and SF filaments are extruded without any GMB breakage by using suitable extrusion parameters.
- Developed filaments exhibit a three-phase foam structure.
- The SF core and sandwiches are successfully 3D printed all at once without any defects.
- Both the nozzles available in printers are utilized for printing sandwich skin and core at once by using optimized printing parameters.

Tensile behavior of filaments and 3D prints

- Filament modulus increases with GMB content.
- Among foams, H60 displays the highest modulus, which is 48.02% higher than the HDPE print.
- 3D printed H - H60 registered 1.5 - 1.8 times higher modulus than the molded counterparts.
- Printed H20 - H60 has 1.16 - 1.56 times higher fracture strength than the printed H.
- A comparison of specific properties suggests that the printed syntactic foam parts have potential to replace some of the molded components which are being used in weight sensitive structures.
- A property map illustrates the capability of 3DP in comparison to other composites produced through various processing techniques.

Flexural behavior of core and concurrently printed sandwiches

- GMBs embedded in the HDPE matrix increase the specific modulus by ~2 times compared to H. The modulus of H - H60 printed foams is higher by 1.39 - 1.08 times against molded counterparts.
- The experimental flexural modulus is found to increase with an increase in GMB content. SH60 sandwich exhibits the highest specific modulus of 1050 ± 12.86 MPa and is 6.06% higher than neat HDPE.
- The 3D printed sandwich has superior strength and is in the range of 1.03 - 1.30 times compared to their respective foamed cores.
- SH20 did not fracture even at 10% strain, whereas SH40 and SH60 fractured due to their brittle nature and increased GMB content. The shear failure is not observed in 3D printed sandwiches.
- Experimental results are in good agreement with theoretical predictions. The deviation between experimental and theoretical modulus and critical load for SH20, SH40, SH60 is 13.18, 11.19, 11.50%, and 2.64, 4.01, 12.97%, respectively.

Compression behavior of core and sandwich samples

- The highest specific compressive modulus and yield strength are observed for H60 at 0.5 mm/min of cross head displacement among foam core.
- The yield strength of SH20, SH40, and SH60 is 1.22, 1.20, and 1.20 times higher than their respective H20, H40, and H60 cores, indicating the potential benefit of realizing all at once 3D printed syntactic foam cored sandwich.
- Specific compressive properties of printed sandwiches are higher than the core.

Buckling and free-vibration response of core and sandwiches

- The increase in GMB content increases both the buckling load and the natural frequency of the printed core and sandwiches.
- The critical buckling load of H20, H40, and H60 is increased by 5, 36.6, 72.8, and 3, 37, 77.5 % compared to neat HDPE when estimated through DTM and MBC.

- Compared to pure HDPE, the modulus of H20, H40, and H60 is increased by 6.29, 45.89, and 94.54 %, respectively.
- Experimentally, the first natural frequency at the buckling site reaches a minimal value and is rapidly increasing in the post-buckling region.
- By comparing critical buckling load through various methods, HDPE and H40 show the close agreement of critical buckling load across all methods except for H20 and H60, wherein VCT over-estimates.
- Property plot reveals the superior performance of 3D printed H60 foam as compared to natural fabric woven thermosetting composite.
- Printed sandwiches displayed global buckling mode shapes without any skin wrinkling or delamination. Compared to H20 - H60, the buckling loads and natural frequency of SH20 - SH60 are higher.
- The increase in frequency displays the lowest value at P_{cr} and subsequently increases after the post-critical buckling regime due to the geometrical stiffness gain. Experimental results match well with the numerical predictions.

The present work successfully demonstrates the development of syntactic foam filament for the 3D printing process. By using suitable printing parameters, SF core and sandwiches are successfully 3D printed without any delamination. Professionals in the 3D printing sector can use the experimental data presented here to realize components for specific applications. GMB content of 60 volume % exhibited superior performance among all the other compositions when synthesized through 3D printing.

SCOPE OF FUTURE WORK

The current work successfully demonstrated the development of lightweight feedstock filament with the intention to widen available material choices for commercially available 3D printers. GMB/HDPE-integrated complex geometrical components can be printed without any warpage, as presented in this work. Strength enhancement can be realized by surface modification of the constituent materials and the strategy of overlapping rasters and is the focus of future investigations.

REFERENCES

- Abdullah, A. M., Rahim, T. N. A. T., Mohamad, D., Akil, H. M. and Rajion, Z. A. (2017). "Mechanical and physical properties of highly ZrO₂/β-TCP filled polyamide 12 prepared via fused deposition modelling (FDM) 3D printer for potential craniofacial reconstruction application." *Materials Letters*, 189, 307-309.
- Abramovich, H., Govich, D. and Grunwald, A. (2015). "Buckling prediction of panels using the vibration correlation technique." *Progress in Aerospace Sciences*, 78, 62-73.
- Agarwal, B. D. and Broutman, L. J. (1980). "Analysis and performance of fiber composites." *Journal of Polymer Science: Polymer Letters Edition*, 18(10), 689-690.
- Alaimo, G., Marconi, S., Costato, L. and Auricchio, F. (2017). "Influence of meso-structure and chemical composition on FDM 3D-printed parts." *Composites Part B: Engineering*, 113, 371-380.
- Alkan, C., Arslan, M., Cici, M., Kaya, M. and Aksoy, M. (1995). "A study on the production of a new material from fly ash and polyethylene." *Resources, conservation and recycling*, 13(3-4), 147-154.
- Allen, H. (1969). *Analysis and Design of Structural Sandwich Panels* Pergamon Press. London.
- Amirpour, M., Bickerton, S., Calius, E., Das, R. and Mace, B. (2019). "Numerical and experimental study on deformation of 3D-printed polymeric functionally graded plates: 3D-Digital Image Correlation approach." *Composite Structures*, 211, 481-489.
- Annigeri, U. K. and Veeresh Kumar, G. B. (2018). "Effect of Reinforcement on Density, Hardness and Wear Behavior of Aluminum Metal Matrix Composites: A Review." *Materials Today: Proceedings*, 5(5, Part 2), 11233-11237.
- Arbelo, M. A., de Almeida, S. F. M., Donadon, M. V., Rett, S. R., Degenhardt, R., Castro, S. G. P., Kalnins, K. and Ozoliņš, O. (2014). "Vibration correlation technique

for the estimation of real boundary conditions and buckling load of unstiffened plates and cylindrical shells." *Thin-Walled Structures*, 79, 119-128.

Arbelo, M. A., Kalnins, K., Ozolins, O., Skukis, E., Castro, S. G. and Degenhardt, R. (2015). "Experimental and numerical estimation of buckling load on unstiffened cylindrical shells using a vibration correlation technique." *Thin-Walled Structures*, 94, 273-279.

Arivazhagan, A., Saleem, A., Masood, S., Nikzad, M. and Jagadeesh, K. (2014). "Study of dynamic mechanical properties of fused deposition modelling processed ULTEM material." *American Journal of Engineering and Applied Sciences*, 7, 307-315.

Arza, S. (2012). *Fillers Encyclopedia of Polymer Science and Technology*. 4th edition, John Wiley & Sons, New York.

Arzamasov B. (1989). *Material Science*. Moscow: Mir Publishers.

Ashby, M. F., Evans, A., Fleck, N. A., Gibson, L. J., Hutchinson, J. W. and Wadley, H. N. (2002). "Metal foams: a design guide-Butterworth-Heinemann, Oxford, UK, ISBN 0-7506-7219-6, Published 2000, Hardback, 251 pp." *Materials and Design*, 1(23), 119.

Ashrith, H., Doddamani, M. and Gaitonde, V. (2019). "Effect of wall thickness and cutting parameters on drilling of glass microballoon/epoxy syntactic foam composites." *Composite Structures*, 211, 318-336.

ASTM C365M-16, *Standard Test Method for Flatwise Compressive Properties of Sandwich Cores*, ASTM International, PA, USA.

ASTM C393-16, *Standard Test Method for Core Shear Properties of Sandwich Constructions by Beam Flexure*, ASTM International, PA, USA.

ASTM D638-14, *Standard Test Method for Tensile Properties of Plastics*, ASTM, International, PA, USA.

ASTM D696-13, *Standard Test Method for Coefficient of Linear Thermal Expansion of Plastics Between -300C and 300C with a Vitreous Silica Dilatometer*, ASTM, International, PA, USA.

ASTM D790-17, *Standard Test Methods for Flexural Properties of Unreinforced and Reinforced Plastics and Electrical Insulating Materials*, ASTM, International, PA, USA.

ASTM D792-13, *Standard Test Methods for Density and Specific Gravity (Relative Density) of Plastics by Displacement*, ASTM International, PA, USA.

ASTM D3878-18, *Standard Terminology for Composite Materials*, ASTM International, West Conshohocken, PA, USA.

ASTM F2792-10, *Standard Terminology for Additive Manufacturing Technologies*, ASTM International, PA, USA.

Atagür, M., Sarikanat, M., Uysalman, T., Polat, O., Elbeyli, İ. Y., Seki, Y. and Sever, K. (2018). "Mechanical, thermal, and viscoelastic investigations on expanded perlite-filled high-density polyethylene composite." *Journal of Elastomers & Plastics*, 50(8), 747-761.

Baglari, S., Kole, M. and Dey, T. K. (2011). "Effective thermal conductivity and coefficient of linear thermal expansion of high-density polyethylene — fly ash composites." *Indian Journal of Physics*, 85(4), 559-573.

Bardella, L. and Genna, F. (2001). "On the elastic behavior of syntactic foams." *International Journal of Solids and Structures*, 38(40), 7235-7260.

Benchechou, B., Coni, M., Howarth, H. and White, R. (1998). "Some aspects of vibration damping improvement in composite materials." *Composites Part B: Engineering*, 29(6), 809-817.

Bharath Kumar, B., Zeltmann, S. E., Doddamani, M., Gupta, N., Gurupadu, S. and Sailaja, R. (2016). "Effect of cenosphere surface treatment and blending method on

the tensile properties of thermoplastic matrix syntactic foams." *Journal of Applied Polymer Science*, 133(35), 4381.

Bharath Kumar, B. R., Doddamani, M., Zeltmann, S. E., Gupta, N., Uzma, Gurupadu, S. and Sailaja, R. R. N. (2016). "Effect of particle surface treatment and blending method on flexural properties of injection-molded cenosphere/HDPE syntactic foams." *Journal of Materials Science*, 51(8), 3793-3805.

Birman, V. and Kardomateas, G. A. (2018). "Review of current trends in research and applications of sandwich structures." *Composites Part B: Engineering*, 142, 221-240.

Bokaian, A. (1988). "Natural frequencies of beams under compressive axial loads." *Journal of Sound and Vibration*, 126(1), 49-65.

Boschetto, A. and Bottini, L. (2016). "Design for manufacturing of surfaces to improve accuracy in Fused Deposition Modeling." *Robotics and Computer-Integrated Manufacturing*, 37, 103-114.

Boschetto, A., Bottini, L. and Veniali, F. (2016). "Finishing of Fused Deposition Modeling parts by CNC machining." *Robotics and Computer-Integrated Manufacturing*, 41, 92-101.

Brenken, B., Barocio, E., Favaloro, A., Kunc, V. and Pipes, R. B. (2018). "Fused filament fabrication of fiber-reinforced polymers: A review." *Additive Manufacturing*, 21, 1-16.

Breunig, P., Damodaran, V., Shahapurkar, K., Waddar, S., Doddamani, M., Jeyaraj, P. and Prabhakar, P. (2020). "Dynamic impact behavior of syntactic foam core sandwich composites." *Journal of Composite Materials*, 54(4), 535-547.

Budiansky, B. and Fleck, N. A. (1993). "Compressive failure of fibre composites." *Journal of the Mechanics and Physics of Solids*, 41(1), 183-211.

Bunn, P. and Mottram, J. (1993). "Manufacture and compression properties of syntactic foams." *Composites*, 24(7), 565-571.

Burgiel, J., Butcher, W., Halpern, R., Oliver, D. and Tangora, P. (1994). Cost evaluation of automated and manual post-consumer plastic bottle sorting systems. Final report: Beck (RW), Orlando, FL (United States).

Burgueno, R., Quagliata, M. J., Mohanty, A. K., Mehta, G., Drzal, L. T. and Misra, M. (2004). "Load-bearing natural fiber composite cellular beams and panels." *Composites Part A: Applied Science and Manufacturing*, 35(6), 645-656.

Byberg, K. I., Gebisa, A. W. and Lemu, H. G. (2018). "Mechanical properties of ULTEM 9085 material processed by fused deposition modeling." *Polymer Testing*, 72, 335-347.

Caminero, M. A., Chacón, J. M., García-Moreno, I. and Reverte, J. M. (2018). "Interlaminar bonding performance of 3D printed continuous fibre reinforced thermoplastic composites using fused deposition modelling." *Polymer Testing*, 68, 415-423.

Chand, N., Sharma, P. and Fahim, M. (2010). "Correlation of mechanical and tribological properties of organosilane modified cenosphere filled high density polyethylene." *Materials Science and Engineering: A*, 527(21-22), 5873-5878.

Chawla, K. K. (2001). *Composite Materials*. New York: Springer.

Chen, F., Mac, G. and Gupta, N. (2017). "Security features embedded in computer aided design (CAD) solid models for additive manufacturing." *Materials & Design*, 128, 182-194.

Chen, H., Chen, T. and Hsu, C. (2006). "Effects of wood particle size and mixing ratios of HDPE on the properties of the composites." *Holz als Roh-und Werkstoff*, 64(3), 172-177.

Chen, H. and Zhao, Y. F. (2016). "Process parameters optimization for improving surface quality and manufacturing accuracy of binder jetting additive manufacturing process." *Rapid prototyping journal*, 22(3), 527-538.

Corigliano, A., Rizzi, E. and Papa, E. (2000). "Experimental characterization and numerical simulations of a syntactic-foam/glass-fibre composite sandwich." *Composites Science and Technology*, 60(11), 2169-2180.

Dakshinamurthy, D. and Gupta, S. (2018). "A study on the influence of process parameters on the viscoelastic properties of ABS components manufactured by FDM process." *Journal of The Institution of Engineers (India): Series C*, 99(2), 133-138.

Deepthi, M., Sailaja, R., Sampathkumaran, P., Seetharamu, S. and Vynatheya, S. (2014). "High density polyethylene and silane treated silicon nitride nanocomposites using high-density polyethylene functionalized with maleate ester: Mechanical, tribological and thermal properties." *Materials & Design (1980-2015)*, 56, 685-695.

Dikshit, V., Nagalingam, A. P., Goh, G. D., Agarwala, S., Yeong, W. Y. and Wei, J. (2019). "Quasi-static indentation analysis on three-dimensional printed continuous-fiber sandwich composites." *Journal of Sandwich Structures & Materials*, 23(2), 385-404.

Divya, V., Khan, M. A., Rao, B. N. and Sailaja, R. (2015). "High density polyethylene/cenosphere composites reinforced with multi-walled carbon nanotubes: Mechanical, thermal and fire retardancy studies." *Materials & Design*, 65, 377-386.

Divya, V., Pattanshetti, V., Suresh, R. and Sailaja, R. (2013). "Development and characterisation of HDPE/EPDM-g-TMEVS blends for mechanical and morphological properties for engineering applications." *Journal of Polymer Research*, 20(2), 1-11.

Doddamani, M. (2019). "Wear behavior of glass microballoon based closed cell foam." *Materials Research Express*, 6(11), 115314.

Doddamani, M. (2020). "Influence of microballoon wall thickness on dynamic mechanical analysis of closed cell foams." *Materials Research Express*, 6(12), 125348.

- Doddamani, M. and Kulkarni, S. (2011). "Dynamic response of fly ash reinforced functionally graded rubber composite sandwiches-a Taguchi approach." *International Journal of Engineering, Science and Technology*, 3(1), 166-182.
- Doddamani, M. R., Kulkarni, S. M. and Kishore. (2011). "Behavior of sandwich beams with functionally graded rubber core in three point bending." *Polymer Composites*, 32(10), 1541-1551.
- Domingo-Espin, M., Puigoriol-Forcada, J. M., Garcia-Granada, A.-A., Llumà, J., Borros, S. and Reyes, G. (2015). "Mechanical property characterization and simulation of fused deposition modeling Polycarbonate parts." *Materials & Design*, 83, 670-677.
- Dul, S., Fambri, L. and Pegoretti, A. (2016). "Fused deposition modelling with ABS-graphene nanocomposites." *Composites Part A: Applied Science and Manufacturing*, 85, 181-191.
- Durgun, I. and Ertan, R. (2014). "Experimental investigation of FDM process for improvement of mechanical properties and production cost." *Rapid prototyping journal*, 20(3), 228-235.
- El Achaby, M., Ennajih, H., Arrakhiz, F. Z., El Kadib, A., Bouhfid, R., Essassi, E. and Qaiss, A. (2013). "Modification of montmorillonite by novel geminal benzimidazolium surfactant and its use for the preparation of polymer organoclay nanocomposites." *Composites Part B: Engineering*, 51, 310-317.
- Elamin, M., Li, B. and Tan, K. T. (2018). "Impact damage of composite sandwich structures in arctic condition." *Composite Structures*, 192, 422-433.
- Es-Said, O. S., Foyos, J., Noorani, R., Mendelson, M., Marloth, R. and Pregger, B. A. (2000). "Effect of Layer Orientation on Mechanical Properties of Rapid Prototyped Samples." *Materials and Manufacturing Processes*, 15(1), 107-122.

Escócio, V. A., Pacheco, E. B. A. V., Silva, A. L. N. d., Cavalcante, A. d. P. and Visconte, L. L. Y. (2015). "Rheological behavior of renewable polyethylene (HDPE) composites and sponge gourd (*Luffa cylindrica*) residue." *International Journal of Polymer Science*, 714352

Esha, S. and Rajaram. (1997). "Plastic Recycling in Bangalore - India." *Urban Waste Expertise Programme (UWEP), CS-Plast India*, 8-10.

Espalin, D., Arcaute, K., Rodriguez, D., Medina, F., Posner, M. and Wicker, R. (2010). "Fused deposition modeling of patient-specific polymethylmethacrylate implants." *Rapid prototyping journal*, 16(3), 164-173.

Faes, M., Ferraris, E. and Moens, D. (2016). "Influence of inter-layer cooling time on the quasi-static properties of ABS components produced via fused deposition modelling." *Procedia Cirp*, 42, 748-753.

Ferreira, R. T. L., Amatte, I. C., Dutra, T. A. and Bürger, D. (2017). "Experimental characterization and micrography of 3D printed PLA and PLA reinforced with short carbon fibers." *Composites Part B: Engineering*, 124, 88-100.

Ferrigno, T. H. (1978). Handbook of fillers and reinforcements for plastics *H. S. Katz and J. V. Milewski eds* Van Nostrand Reinhold, New York, 66-71.

Fitzharris, E. R., Watanabe, N., Rosen, D. W. and Shofner, M. L. (2018). "Effects of material properties on warpage in fused deposition modeling parts." *The International Journal of Advanced Manufacturing Technology*, 95(5), 2059-2070.

Gangil, B., Kukshal, V., Sharma, A., Patnaik, A. and Kumar, S. (2019). "Development of hybrid fiber reinforced functionally graded polymer composites for mechanical and wear analysis." *AIP Conference Proceedings*, 2057(1), 020059.

Garcia, C. D., Shahapurkar, K., Doddamani, M., Kumar, G. M. and Prabhakar, P. (2018). "Effect of arctic environment on flexural behavior of fly ash cenosphere reinforced epoxy syntactic foams." *Composites Part B: Engineering*, 151, 265-273.

- Geng, P., Zhao, J., Wu, W., Ye, W., Wang, Y., Wang, S. and Zhang, S. (2019). "Effects of extrusion speed and printing speed on the 3D printing stability of extruded PEEK filament." *Journal of Manufacturing Processes*, 37, 266-273.
- Gibson, L. J. and Ashby, M. F. (1999). *Cellular solids: structure and properties*. Cambridge university press.
- Goel, M. D., Bedon, C., Singh, A., Khatri, A. P. and Gupta, L. M. (2021). "An Abridged Review of Buckling Analysis of Compression Members in Construction." *Buildings*, 11(5), 211.
- Gordeev, E. G., Galushko, A. S. and Ananikov, V. P. (2018). "Improvement of quality of 3D printed objects by elimination of microscopic structural defects in fused deposition modeling." *PloS one*, 13(6), e0198370.
- Griffiths, C. A., Howarth, J., De Almeida-Rowbotham, G. and Rees, A. (2016). "A design of experiments approach to optimise tensile and notched bending properties of fused deposition modelling parts." *Proceedings of the Institution of Mechanical Engineers, Part B: Journal of Engineering Manufacture*, 230(8), 1502-1512.
- Gupta, N., Brar, B. S. and Woldesenbet, E. (2001). "Effect of filler addition on the compressive and impact properties of glass fibre reinforced epoxy." *Bulletin of Materials Science*, 24(2), 219-223.
- Gupta, N., Maharsia, R. and Jerro, H. D. (2005). "Enhancement of energy absorption characteristics of hollow glass particle filled composites by rubber addition." *Materials Science and Engineering: A*, 395(1-2), 233-240.
- Gupta, N., Pinisetty, D. and Shunmugasamy, V. C. (2013). *Reinforced polymer matrix syntactic foams: effect of nano and micro-scale reinforcement* (1 ed.): Springer, Cham.

Gupta, N. and Ricci, W. (2006). "Comparison of compressive properties of layered syntactic foams having gradient in microballoon volume fraction and wall thickness." *Materials Science and Engineering: A*, 427(1-2), 331-342.

Gupta, N. and Woldesenbet, E. (2004). "Microballoon wall thickness effects on properties of syntactic foams." *Journal of Cellular Plastics*, 40(6), 461-480.

Gupta, N., Woldesenbet, E. and Mensah, P. (2004). "Compression properties of syntactic foams: effect of cenosphere radius ratio and specimen aspect ratio." *Composites Part A: Applied Science and Manufacturing*, 35(1), 103-111.

Gupta, N., Zeltmann, S. E., Luong, D. D. and Doddamani, M. (2018). 7—Core Materials for Marine Sandwich Structures *Marine Composites: Design and Performance* (pp. 187-224). Cambridge: Elsevier (Woodhead Publishing imprint).

Gupta, N., Zeltmann, S. E., Luong, D. D. and Doddamani, M. (2018). Testing of Foams. In S. Schmauder, C.-S. Chen, K. K. Chawla, N. Chawla, W. Chen, Y. Kagawa & C.-H. Hsueh (Eds.), *Handbook of Mechanics of Materials* (pp. 1-40). Singapore: Springer Singapore.

Gupta, N., Zeltmann, S. E., Shunmugasamy, V. C. and Pinisetty, D. (2014). "Applications of polymer matrix syntactic foams." *JOM*, 66(2), 245-254.

Gwon, J. G., Lee, S. Y., Kang, H. and Kim, J. H. (2012). "Effects of sizes and contents of exothermic foaming agent on physical properties of injection foamed wood fiber/HDPE composites." *International Journal of Precision Engineering and Manufacturing*, 13(6), 1003-1007.

Haldar, A., Managuli, V., Munshi, R., Agarwal, R. and Guan, Z. (2021). "Compressive behaviour of 3D printed sandwich structures based on corrugated core design." *Materials Today Communications*, 26, 101725.

Hemath, M., Mavinkere Rangappa, S., Kushvaha, V., Dhakal, H. N. and Siengchin, S. (2020). "A comprehensive review on mechanical, electromagnetic radiation shielding,

and thermal conductivity of fibers/inorganic fillers reinforced hybrid polymer composites." *Polymer Composites*, 41(10), 3940-3965.

Hwang, S., Reyes, E. I., Moon, K.-s., Rumpf, R. C. and Kim, N. S. (2015). "Thermo-mechanical characterization of metal/polymer composite filaments and printing parameter study for fused deposition modeling in the 3D printing process." *Journal of Electronic Materials*, 44(3), 771-777.

Jakobsen, J., Bozhevolnaya, E. and Thomsen, O. T. (2007). "New peel stopper concept for sandwich structures." *Composites Science and Technology*, 67(15), 3378-3385.

Jayavardhan, M. and Doddamani, M. (2018). "Quasi-static compressive response of compression molded glass microballoon/HDPE syntactic foam." *Composites Part B: Engineering*, 149, 165-177.

Jayavardhan, M., Kumar, B. B., Doddamani, M., Singh, A. K., Zeltmann, S. E. and Gupta, N. (2017). "Development of glass microballoon/HDPE syntactic foams by compression molding." *Composites Part B: Engineering*, 130, 119-131.

John, B. and Nair, C. R. (2014). 13 - Syntactic foams. In H. Dodiuk & S. H. Goodman (Eds.), *Handbook of thermoset plastics (Third Edition)* (pp. 511-554). Boston: William Andrew Publishing.

Karlsson, K. F. and TomasÅström, B. (1997). "Manufacturing and applications of structural sandwich components." *Composites Part A: Applied Science and Manufacturing*, 28(2), 97-111.

Kazmer, D. (2017). 28 - Three-dimensional printing of plastics. In M. Kutz (Ed.), *Applied Plastics Engineering Handbook (Second Edition)* (pp. 617-634): William Andrew Publishing.

Kooistra, G. W., Queheillalt, D. T. and Wadley, H. N. G. (2008). "Shear behavior of aluminum lattice truss sandwich panel structures." *Materials Science and Engineering: A*, 472(1), 242-250.

KSSPMA. (1992). A Guide to Plastics. Bangalore.

Kulkarni, S., Kumar, S. S., Kumar, S. S., Sinha, U. K., Shah, B., Kumar, K. S., Mithran, A. S. and Pillai, K. M. (2021). *Vibration Reduction in Indigenous Wankel Rotary Combustion Engine with Structured Layer Damping*. Paper presented at the Proceedings of the 6th National Symposium on Rotor Dynamics.

Kumar, B. B., Doddamani, M., Zeltmann, S. E., Gupta, N., Ramesh, M. and Ramakrishna, S. (2016). "Processing of cenosphere/HDPE syntactic foams using an industrial scale polymer injection molding machine." *Materials & Design*, 92, 414-423.

Labella, M., Zeltmann, S. E., Shunmugasamy, V. C., Gupta, N. and Rohatgi, P. K. (2014). "Mechanical and thermal properties of fly ash/vinyl ester syntactic foams." *Fuel*, 121, 240-249.

Laishram, R., Bisheshwar, H., Shivakumar, N., Amrutur, B. and Reddy, T. (2019). *A Study on the Effects of Fiber Orientation on Woven Glass Fiber Composite Structures*. Paper presented at the 2nd International Conference on Research in Science, Engineering and Technology, Oxford, United Kingdom.

Lalehpour, A. and Barari, A. (2018). "A more accurate analytical formulation of surface roughness in layer-based additive manufacturing to enhance the product's precision." *The International Journal of Advanced Manufacturing Technology*, 96(9), 3793-3804.

Lee, J. and Huang, A. (2013). "Fatigue analysis of FDM materials." *Rapid prototyping journal*, 19(4), 291-299.

Lee, S. M. (1992). *Handbook of composite reinforcements*: John Wiley & Sons.

- Lee, T., Boey, F. and Khor, K. (1995). "On the determination of polymer crystallinity for a thermoplastic PPS composite by thermal analysis." *Composites Science and Technology*, 53(3), 259-274.
- Li, T. and Wang, L. (2017). "Bending behavior of sandwich composite structures with tunable 3D-printed core materials." *Composite Structures*, 175, 46-57.
- Lingaiah, K. and Suryanarayana, B. G. (1991). "Strength and stiffness of sandwich beams in bending." *Experimental Mechanics*, 31(1), 1-7.
- Liu, H., Wu, Q., Han, G., Yao, F., Kojima, Y. and Suzuki, S. (2008). "Compatibilizing and toughening bamboo flour-filled HDPE composites: Mechanical properties and morphologies." *Composites Part A: Applied Science and Manufacturing*, 39(12), 1891-1900.
- Liu, H., Wu, Q. and Zhang, Q. (2009). "Preparation and properties of banana fiber-reinforced composites based on high density polyethylene (HDPE)/Nylon-6 blends." *Bioresource technology*, 100(23), 6088-6097.
- Lombardi, J. L., Hoffinan, R. A., Waters, J. A. and Popovich, D. (1997). *Issues associated with EFF & FDM ceramic filled feedstock formulation*. Paper presented at the International Solid Freeform Fabrication Symposium.
- Malloy, R., Hudson, J. and Lee, S. (1990). International encyclopedia of composites edited by Lee, SM VCH.
- Manalo, A., Aravinthan, T., Karunasena, W. and Islam, M. (2010). "Flexural behaviour of structural fibre composite sandwich beams in flatwise and edgewise positions." *Composite Structures*, 92(4), 984-995.
- Manas, C. and Salil, R. (2006). "Plastic Technology" *Handbook*. CRC press, NewYork, 2-6.
- Masood, S. and Song, W. (2004). "Development of new metal/polymer materials for rapid tooling using fused deposition modelling." *Materials & Design*, 25(7), 587-594.

Matli, P. R., Krishnan, A. V., Manakari, V., Parande, G., Chua, B. W., Wong, S. C. K., Lim, C. Y. H. and Gupta, M. (2020). "A new method to lightweight and improve strength to weight ratio of magnesium by creating a controlled defect." *Journal of Materials Research and Technology*, 9(3), 3664-3675.

Matsunaga, H. (1996). "Free vibration and stability of thin elastic beams subjected to axial forces." *Journal of Sound and Vibration*, 191(5), 917-933.

Mines, R. A. W., Tsopanos, S., Shen, Y., Hasan, R. and McKown, S. T. (2013). "Drop weight impact behaviour of sandwich panels with metallic micro lattice cores." *International Journal of Impact Engineering*, 60, 120-132.

Mirzabeigy, A. and Madoliat, R. (2016). "Large amplitude free vibration of axially loaded beams resting on variable elastic foundation." *Alexandria Engineering Journal*, 55(2), 1107-1114.

Mohamed, M., Anandan, S., Huo, Z., Birman, V., Volz, J. and Chandrashekhara, K. (2015). "Manufacturing and characterization of polyurethane based sandwich composite structures." *Composite Structures*, 123, 169-179.

Mohamed, O. A., Masood, S. H. and Bhowmik, J. L. (2015). "Optimization of fused deposition modeling process parameters: a review of current research and future prospects." *Advances in Manufacturing*, 3(1), 42-53.

Mohanty, S. and Nayak, S. K. (2010). "Short Bamboo Fiber-reinforced HDPE Composites: Influence of Fiber Content and Modification on Strength of the Composite." *Journal of reinforced plastics and composites*, 29(14), 2199-2210.

Nanavaty, K. (1997). *Recycling of Plastics: Indian Experience*. Paper presented at the 3rd International Plastics Exhibition and Conference on Environment/Recycling of Plastics, New Delhi.

- Narahara, H., Shirahama, Y. and Koresawa, H. (2016). "Improvement and Evaluation of the Interlaminar Bonding Strength of FDM Parts by Atmospheric-Pressure Plasma." *Procedia Cirp*, 42, 754-759.
- Nikzad, M., Masood, S. and Sbarski, I. (2011). "Thermo-mechanical properties of a highly filled polymeric composites for Fused Deposition Modeling." *Materials & Design*, 32, 3448-3456.
- Ning, F., Cong, W., Hu, Y. and Wang, H. (2017). "Additive manufacturing of carbon fiber-reinforced plastic composites using fused deposition modeling: Effects of process parameters on tensile properties." *Journal of Composite Materials*, 51(4), 451-462.
- Ning, H., Janowski, G. M., Vaidya, U. K. and Husman, G. (2007). "Thermoplastic sandwich structure design and manufacturing for the body panel of mass transit vehicle." *Composite Structures*, 80(1), 82-91.
- Noor, A. K., Burton, W. S. and Bert, C. W. (1996). "Computational Models for Sandwich Panels and Shells." *Applied Mechanics Reviews*, 49(3), 155-199.
- Nugroho, A., Ardiansyah, R., Rusita, L. and Larasati, I. (2018). "Effect of layer thickness on flexural properties of PLA (PolyLactid Acid) by 3D printing." *Journal of Physics: Conference Series*, 1130, 012017.
- Omar, M. Y., Xiang, C., Gupta, N., Strbik III, O. M. and Cho, K. (2015). "Syntactic foam core metal matrix sandwich composite: Compressive properties and strain rate effects." *Materials Science and Engineering: A*, 643, 156-168.
- Omar, M. Y., Xiang, C., Gupta, N., Strbik, O. M. and Cho, K. (2015). "Syntactic foam core metal matrix sandwich composite under bending conditions." *Materials & Design*, 86, 536-544.
- Ou, R., Xie, Y., Wolcott, M. P., Sui, S. and Wang, Q. (2014). "Morphology, mechanical properties, and dimensional stability of wood particle/high density

polyethylene composites: effect of removal of wood cell wall composition." *Materials & Design*, 58, 339-345.

Panupakorn, P., Chaichana, E., Praserttham, P. and Jongsomjit, B. (2013). "Polyethylene/Clay Nanocomposites Produced by Polymerization with Zirconocene/MAO Catalyst." *Journal of Nanomaterials*, 2013, 154874.

Park, S., Russell, B. P., Deshpande, V. S. and Fleck, N. A. (2012). "Dynamic compressive response of composite square honeycombs." *Composites Part A: Applied Science and Manufacturing*, 43(3), 527-536.

Patil, B., Bharath Kumar, B. R. and Doddamani, M. (2019). "Compressive behavior of fly ash based 3D printed syntactic foam composite." *Materials Letters*, 254, 246-249.

Patil, B., Kumar, B. B., Bontha, S., Balla, V. K., Powar, S., Kumar, V. H., Suresha, S. and Doddamani, M. (2019). "Eco-friendly lightweight filament synthesis and mechanical characterization of additively manufactured closed cell foams." *Composites Science and Technology*, 183, 107816.

Perez, B. (2013). "Printing Pioneer Scott Crump's Kitchen Experiment." *South China Morning Post*.

Petras, A. (1999). *Design of sandwich structures*. University of Cambridge.

Plantema, F. J. (1966). *Sandwich construction: the bending and buckling of sandwich beams, plates, and shells*. New York: John Wiley and Sons.

Ponnamma, D., Cabibihan, J.-J., Rajan, M., Pethaiah, S. S., Deshmukh, K., Gogoi, J. P., Pasha, S. K. K., Ahamed, M. B., Krishnegowda, J., Chandrashekar, B. N., Polu, A. R. and Cheng, C. (2019). "Synthesis, optimization and applications of ZnO/polymer nanocomposites." *Materials Science and Engineering: C*, 98, 1210-1240.

- Porter, D. A., Hoang, T. V. and Berfield, T. A. (2017). "Effects of in-situ poling and process parameters on fused filament fabrication printed PVDF sheet mechanical and electrical properties." *Additive Manufacturing*, 13, 81-92.
- Prüß, H. and Vietor, T. (2015). "Design for fiber-reinforced additive manufacturing." *Journal of Mechanical Design*, 137(11), 111409.
- Puterman, M., Narkis, M. and Kenig, S. (1980). "Syntactic foams I. Preparation, structure and properties." *Journal of Cellular Plastics*, 16(4), 223-229.
- Qin, Q.-h., Zhang, J.-x., Wang, Z.-j., Li, H.-m. and Guo, D. (2014). "Indentation of sandwich beams with metal foam core." *Transactions of Nonferrous Metals Society of China*, 24(8), 2440-2446.
- Rajaneesh, A., Sridhar, I. and Rajendran, S. (2014). "Relative performance of metal and polymeric foam sandwich plates under low velocity impact." *International Journal of Impact Engineering*, 65, 126-136.
- Rajesh, M. and Pitchaimani, J. (2017). "Experimental investigation on buckling and free vibration behavior of woven natural fiber fabric composite under axial compression." *Composite Structures*, 163, 302-311.
- Rayegani, F. and Onwubolu, G. C. (2014). "Fused deposition modelling (FDM) process parameter prediction and optimization using group method for data handling (GMDH) and differential evolution (DE)." *The International Journal of Advanced Manufacturing Technology*, 73(1-4), 509-519.
- Reinhart, T. J. (1998). *"Overview of composite materials" Handbook of composites.* Springer, Boston.
- Rezayat, H., Zhou, W., Siriruk, A., Penumadu, D. and Babu, S. S. (2015). "Structure–mechanical property relationship in fused deposition modelling." *Materials Science and Technology*, 31(8), 895-903.

Riddick, J. C., Haile, M. A., Von Wahlde, R., Cole, D. P., Bamiduro, O. and Johnson, T. E. (2016). "Fractographic analysis of tensile failure of acrylonitrile-butadiene-styrene fabricated by fused deposition modeling." *Additive Manufacturing*, 11, 49-59.

Rinaldi, M., Ghidini, T., Cecchini, F., Brandao, A. and Nanni, F. (2018). "Additive layer manufacturing of poly (ether ether ketone) via FDM." *Composites Part B: Engineering*, 145, 162-172.

Sachinkumar, Narendranath, S. and Chakradhar, D. (2020). "Studies on microstructure and mechanical characteristics of as cast AA6061/SiC/fly ash hybrid AMCs produced by stir casting." *Materials Today: Proceedings*, 20, A1-A5.

Satpathy, B. K., Das, A. and Patnaik, A. (2011). "Ductile-to-brittle transition in cenosphere-filled polypropylene composites." *Journal of Materials Science*, 46(6), 1963-1974.

Scott, G. G. (2000). "Polymers." *Polymer Degradation and Stability*, 68, 1-7.

Sewda, K. and Maiti, S. N. (2010). "Crystallization and melting behavior of HDPE in HDPE/teak wood flour composites and their correlation with mechanical properties." *Journal of Applied Polymer Science*, 118(4), 2264-2275.

Seyedkanani, A., Niknam, H. and Akbarzadeh, A. (2020). "Bending behavior of optimally graded 3D printed cellular beams." *Additive Manufacturing*, 35, 101327.

Shahapurkar, K., Doddamani, M., Mohan Kumar, G. and Gupta, N. (2019). "Effect of cenosphere filler surface treatment on the erosion behavior of epoxy matrix syntactic foams." *Polymer Composites*, 40(6), 2109-2118.

Shaikh, A. and Channiwala, S. (2006). "Experimental and analytical investigation of jute polyester composite for long continuous fiber reinforcement." *Journal of Reinforced Plastics and Composites*, 25(8), 863-873.

Shaikh, H., Anis, A., Poulouse, A. M., Alam, M., A-Otaibi, M. N., Alam, M. A. and Al-Zahrani, S. M. (2016). "Studies on High Density Polyethylene Reinforced with

Phosphate Ore Particles: Thermal, Rheological, Mechanical and Morphological Properties." *Polymer-Plastics Technology and Engineering*, 55(17), 1831-1841.

Shariyat, M. (2007). "Thermal buckling analysis of rectangular composite plates with temperature-dependent properties based on a layerwise theory." *Thin-Walled Structures*, 45(4), 439-452.

Shekhar, B. (2012). "Roadmap to 13 Million Tons." *Plastindia in-house journal*, 37, 6-11.

Shunmugasamy, V. C., Pinisetty, D. and Gupta, N. (2012). "Thermal expansion behavior of hollow glass particle/vinyl ester composites." *Journal of Materials Science*, 47(14), 5596-5604.

Shunmugasamy, V. C., Zeltmann, S. E., Gupta, N. and Strbik, O. M. (2014). "Compressive Characterization of Single Porous SiC Hollow Particles." *JOM*, 66(6), 892-897.

Shutov, F. A. (1986). *Syntactic polymer foams*. Paper presented at the Chromatography/foams/copolymers, Berlin, Heidelberg.

Singer, J. A., Arbocz, J. A., Weller, T. A. and Cheney, J. A. R. (2003). "Buckling Experiments: Experimental Methods in Buckling of Thin-Walled Structures. Shells, Built-up Structures, Composites and Additional Topics, Volume 2." *Applied Mechanics Reviews*, 56(1), B5.

Singh, R., Bedi, P., Fraternali, F. and Ahuja, I. (2016). "Effect of single particle size, double particle size and triple particle size Al₂O₃ in Nylon-6 matrix on mechanical properties of feed stock filament for FDM." *Composites Part B: Engineering*, 106, 20-27.

Singh, R., Kumar, R. and Kumar, S. (2017). "Polymer waste as fused deposition modeling feed stock filament for industrial applications." *Ref. module in "Materials Science and Materials Engineering"*, (pp. 1-12) Elsevier, U.K.

Singh, R., Singh, N., Bedi, P. and Ahuja, I. (2016). "Polymer Single-Screw Extrusion With Metal Powder Reinforcement." *Ref. module in "Materials Science and Materials Engineering"*, (pp. 1-18) Elsevier, U.K.

Singh, R., Singh, S. and Fraternali, F. (2016). "Development of in-house composite wire based feed stock filaments of fused deposition modelling for wear-resistant materials and structures." *Composites Part B: Engineering*, 98, 244-249.

Singh, R., Singh, S. and Mankotia, K. (2016). "Development of ABS based wire as feedstock filament of FDM for industrial applications." *Rapid prototyping journal*, 22(2), 300-310.

Souza, M. and Assaid, L. (1991). "A new technique for the prediction of buckling loads from nondestructive vibration tests." *Experimental Mechanics*, 31(2), 93-97.

Spoerk, M., Arbeiter, F., Cajner, H., Sapkota, J. and Holzer, C. (2017). "Parametric optimization of intra-and inter-layer strengths in parts produced by extrusion-based additive manufacturing of poly (lactic acid)." *Journal of Applied Polymer Science*, 134(41), 45401.

Spoerk, M., Arbeiter, F., Raguz, I., Weingrill, G., Fischinger, T., Traxler, G., Schuschnigg, S., Cardon, L. and Holzer, C. (2018). "Polypropylene filled with glass spheres in extrusion-based additive manufacturing: effect of filler size and printing chamber temperature." *Macromolecular Materials and Engineering*, 303(7), 1800179.

Srinivasan, N. K. and Ramakrishnan, S. S. (1983). *The science of engineering materials*. New Delhi: Oxford & IBH.

Steeves, C. A. and Fleck, N. A. (2004). "Collapse mechanisms of sandwich beams with composite faces and a foam core, loaded in three-point bending. Part I: analytical models and minimum weight design." *International Journal of Mechanical Sciences*, 46(4), 561-583.

- Tagliavia, G., Porfiri, M. and Gupta, N. (2010). "Analysis of flexural properties of hollow-particle filled composites." *Composites Part B: Engineering*, 41(1), 86-93.
- Tang, X., Jian, W., Huang, J., Zhao, F., Li, C., Xiao, X., Yao, X. and Luo, S. (2018). "Spall damage of a Ta particle-reinforced metallic glass matrix composite under high strain rate loading." *Materials Science and Engineering: A*, 711, 284-292.
- Tekinalp, H. L., Kunc, V., Velez-Garcia, G. M., Duty, C. E., Love, L. J., Naskar, A. K., Blue, C. A. and Ozcan, S. (2014). "Highly oriented carbon fiber–polymer composites via additive manufacturing." *Composites Science and Technology*, 105, 144-150.
- Theotokoglou, E. E. (1996). "Analytical determination of the ultimate strength of sandwich beams." *Applied Composite Materials*, 3(5), 345-353.
- Thomsen, O. T. (2009). "Sandwich materials for wind turbine blades—present and future." *Journal of Sandwich Structures & Materials*, 11(1), 7-26.
- Thomson WT, D. M. a. P. C. (2008). "Theory of vibrations with applications." *5th ed. India: Pearson Education*.
- Tian, X., Liu, T., Wang, Q., Dilmurat, A., Li, D. and Ziegmann, G. (2017). "Recycling and remanufacturing of 3D printed continuous carbon fiber reinforced PLA composites." *Journal of cleaner production*, 142, 1609-1618.
- Timoshenko, J. M. G. a. (2004). *Mechanics of materials*, (2nd ed.). New Delhi: CBS Publishers & Distributors Pvt.Ltd.
- Torres, J., Cotelo, J., Karl, J. and Gordon, A. P. (2015). "Mechanical Property Optimization of FDM PLA in Shear with Multiple Objectives." *JOM*, 67(5), 1183-1193.
- Triantafillou, T. C. and Gibson, L. J. (1987). "Failure mode maps for foam core sandwich beams." *Materials Science and Engineering*, 95, 37-53.

Triantafillou, T. C. and Gibson, L. J. (1987). "Minimum weight design of foam core sandwich panels for a given strength." *Materials Science and Engineering*, 95, 55-62.

Tsouknidas, A., Pantazopoulos, M., Katsoulis, I., Fasnakis, D., Maropoulos, S. and Michailidis, N. (2016). "Impact absorption capacity of 3D-printed components fabricated by fused deposition modelling." *Materials & Design*, 102, 41-44.

Tuan Rahim, T. N. A., Abdullah, A. M., Md Akil, H., Mohamad, D. and Rajion, Z. A. (2015). "Preparation and characterization of a newly developed polyamide composite utilising an affordable 3D printer." *Journal of Reinforced Plastics and Composites*, 34(19), 1628-1638.

Turner, B. N. and Gold, S. A. (2015). "A review of melt extrusion additive manufacturing processes: II. Materials, dimensional accuracy, and surface roughness." *Rapid prototyping journal*, 21 (3), 250–261.

Turner, B. N., Strong, R. and Gold, S. A. (2014). "A review of melt extrusion additive manufacturing processes: I. Process design and modeling." *Rapid prototyping journal*, 20(3), 192-204.

Tuttle, M., Singhatanadgid, P. and Hinds, G. (1999). "Buckling of composite panels subjected to biaxial loading." *Experimental Mechanics*, 39(3), 191-201.

Ugural, A. C. and Fenster, S. K. (2003). *Advanced strength and applied elasticity (Fourth Edition)*. New Jersey: Pearson education.

Vijayavenkataraman, S., Fuh, J. Y. and Lu, W. F. (2017). "3D Printing and 3D Bioprinting in Pediatrics." *Bioengineering*, 4(3), 63.

Vinson, J. (1999). *The behavior of sandwich structures of isotropic and composite materials* (1 ed.). U.S.A: CRC; Routledge.

Waddar, S., Jeyaraj, P. and Doddamani, M. (2018). "Influence of axial compressive loads on buckling and free vibration response of surface-modified fly ash

cenosphere/epoxy syntactic foams." *Journal of Composite Materials*, 52(19), 2621-2630.

Waddar, S., Pitchaimani, J. and Doddamani, M. (2018). "Snap-through buckling of fly ash cenosphere/epoxy syntactic foams under thermal environment." *Thin-Walled Structures*, 131, 417-427.

Waddar, S., Pitchaimani, J. and Doddamani, M. (2020). "Effect of thermal loading on syntactic foam sandwich composite." *Polymer Composites*, 41(5), 1774-1784.

Waddar, S., Pitchaimani, J., Doddamani, M. and Barbero, E. (2019). "Buckling and vibration behaviour of syntactic foam core sandwich beam with natural fiber composite facings under axial compressive loads." *Composites Part B: Engineering*, 175, 107133.

Waddar, S., Pitchaimani, J., Doddamani, M. and Gupta, N. (2018). "Buckling and Free Vibration Behavior of Cenosphere/Epoxy Syntactic Foams under Axial Compressive Loading." *Materials Performance and Characterization*, 7(1), 532-546.

Wadley, H. N. G., Fleck, N. A. and Evans, A. G. (2003). "Fabrication and structural performance of periodic cellular metal sandwich structures." *Composites Science and Technology*, 63(16), 2331-2343.

Wang, A.-J. and McDowell, D. (2004). "In-plane stiffness and yield strength of periodic metal honeycombs." *J. Eng. Mater. Technol.*, 126(2), 137-156.

Wang, D. (2009). "Impact behavior and energy absorption of paper honeycomb sandwich panels." *International Journal of Impact Engineering*, 36(1), 110-114.

Wang, J., Xie, H., Weng, Z., Senthil, T. and Wu, L. (2016). "A novel approach to improve mechanical properties of parts fabricated by fused deposition modeling." *Materials & Design*, 105, 152-159.

Wang, R., Shang, J., Li, X., Luo, Z. and Wu, W. (2018). "Vibration and damping characteristics of 3D printed Kagome lattice with viscoelastic material filling." *Scientific reports*, 8(1), 1-13.

Wasiak, A., Sajkiewicz, P. and Woźniak, A. (1999). "Effects of cooling rate on crystallinity of i-polypropylene and polyethylene terephthalate crystallized in nonisothermal conditions." *Journal of Polymer Science Part B: Polymer Physics*, 37(20), 2821-2827.

Weng, Z., Wang, J., Senthil, T. and Wu, L. (2016). "Mechanical and thermal properties of ABS/montmorillonite nanocomposites for fused deposition modeling 3D printing." *Materials & Design*, 102, 276-283.

Wu, H., Kitipornchai, S. and Yang, J. (2015). "Free vibration and buckling analysis of sandwich beams with functionally graded carbon nanotube-reinforced composite face sheets." *International Journal of Structural Stability and Dynamics*, 15(07), 1540011.

Wu, P., Wang, J. and Wang, X. (2016). "A critical review of the use of 3-D printing in the construction industry." *Automation in Construction*, 68, 21-31.

Yang, C., Tian, X., Li, D., Cao, Y., Zhao, F. and Shi, C. (2017). "Influence of thermal processing conditions in 3D printing on the crystallinity and mechanical properties of PEEK material." *Journal of Materials Processing Technology*, 248, 1-7.

Yao, T., Deng, Z., Zhang, K. and Li, S. (2019). "A method to predict the ultimate tensile strength of 3D printing polylactic acid (PLA) materials with different printing orientations." *Composites Part B: Engineering*, 163, 393-402.

Yao, X., Luan, C., Zhang, D., Lan, L. and Fu, J. (2017). "Evaluation of carbon fiber-embedded 3D printed structures for strengthening and structural-health monitoring." *Materials & Design*, 114, 424-432.

- Yaseer Omar, M., Xiang, C., Gupta, N., Strbik, O. M. and Cho, K. (2015). "Syntactic foam core metal matrix sandwich composite: Compressive properties and strain rate effects." *Materials Science and Engineering: A*, 643, 156-168.
- Yasui, Y. (2000). "Dynamic axial crushing of multi-layer honeycomb panels and impact tensile behavior of the component members." *International Journal of Impact Engineering*, 24(6), 659-671.
- Yuan, C., Bergsma, O., Koussios, S., Zu, L. and Beukers, A. (2012). "Optimization of Sandwich Composites Fuselages Under Flight Loads." *Applied Composite Materials*, 19(1), 47-64.
- Yuan, M. and Bourell, D. (2016). "Quality improvement of optically translucent parts manufactured from LS and SL." *Rapid prototyping journal*, 22(1), 87-96.
- Zeng, C., Liu, L., Bian, W., Leng, J. and Liu, Y. (2021). "Bending performance and failure behavior of 3D printed continuous fiber reinforced composite corrugated sandwich structures with shape memory capability." *Composite Structures*, 262, 113626.
- Zhang, J., Qin, Q., Ai, W., Li, H. and Wang, T. (2014). "The failure behavior of geometrically asymmetric metal foam core sandwich beams under three-point bending." *Journal of Applied Mechanics*, 81(7), 071008.
- Zhang, J., Qin, Q., Xiang, C. and Wang, T. J. (2016). "Dynamic response of slender multilayer sandwich beams with metal foam cores subjected to low-velocity impact." *Composite Structures*, 153, 614-623.
- Zhang, J., Zhou, R., Wang, M., Qin, Q., Ye, Y. and Wang, T. J. (2018). "Dynamic response of double-layer rectangular sandwich plates with metal foam cores subjected to blast loading." *International Journal of Impact Engineering*, 122, 265-275.

Zhu, F., Chou, C. C. and Yang, K. H. (2011). "Shock enhancement effect of lightweight composite structures and materials." *Composites Part B: Engineering*, 42(5), 1202-1211.

Zou, R., Xia, Y., Liu, S., Hu, P., Hou, W., Hu, Q. and Shan, C. (2016). "Isotropic and anisotropic elasticity and yielding of 3D printed material." *Composites Part B: Engineering*, 99, 506-513.

LIST OF PUBLICATIONS

INTERNATIONAL JOURNALS

1. **Bharath H S**, Dilip Bonthu, Pavana Prabhakar and Mrityunjay Doddamani (2020). “Three-dimensional printed lightweight composite foams.” *ACS Omega*, 5(35): p. 22536–22550. (SCI, 3.512 IF)
2. **Bharath H S**, Akshay Sawardekar, Sunil Waddar, P Jeyaraj and Mrityunjay Doddamani (2020). “Mechanical behavior of 3D printed syntactic foam composites.” *Composite Structures*, 254: Art. No.112832. (SCI, 5.407 IF).
3. **Bharath H S**, Akshay Sawardekar, Sunil Waddar, P Jeyaraj and Mrityunjay Doddamani (2021). “Effect of axial compression on dynamic response of concurrently printed sandwich.” *Composite Structures*, 259: Art. No. 113223. (SCI, 5.407 IF).
4. **Bharath H S**, Dilip Bonthu, Suhasini Gururaja, Pavana Prabhakar and Mrityunjay Doddamani (2021). “Flexural response of 3D printed sandwich composite.” *Composite Structures*, 259: Art. No. 113732. (SCI, 5.407 IF).

INTERNATIONAL CONFERENCES

1. **Bharath H S**, Pavana Prabhakar, Suhasini Gururaja and Mrityunjay Doddamani (2020). “Compressive behaviour of 3D printed foam.” Proceedings of the American Society for Composites - 35th Annual Technical Conference, September 14-16, 2020, NJ, USA.

BIO-DATA

1. Name : Bharath H S
2. Father's Name : H S Siddappa
3. Date of Birth : 09th March 1991
4. Nationality : Indian
5. Marital Status : Married
6. Address : Department of Mechanical Engineering
National Institute of Technology Karnataka
Surathkal, PO Srinivasnagar 575 025
Karnataka, India.
7. Mobile Number : +91 8904318630
8. E-mail id. : *bharath.mechengg@gmail.com*
9. Educational Qualification :

Qualification	University/Board	Year of Passing
Ph.D. (Mechanical Engineering)	National Institute of Technology Karnataka	Pursuing
M.Tech. (Mechanical Engineering)	Visvesvaraya Technological University, Belgaum	2014
B.E. (Mechanical Engineering)	Visvesvaraya Technological University, Belgaum	2012
